UNIVERSITY OF SHEFFIELD

The application of modal decomposition techniques for the analysis of environmental flows

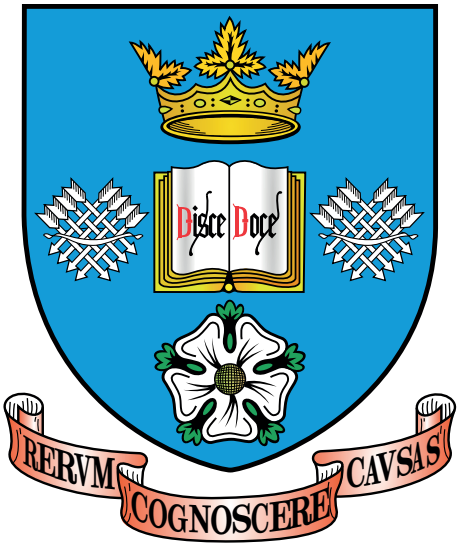

by

Jonathan Higham

A thesis submitted in partial fulfilment for the degree of Doctorate of Philosophy

Department of Civil & Structural Engineering

May 2017

Abstract

Civil Engineering and fluid mechanics are two fields that are not usually put into the same category. In reality however, many of the problems faced in Civil Engineering are caused by fluids. For example: the mixing of pollutants; the scouring of riverbanks; and the undesired oscillations of bridges and buildings caused by wind. Whilst it is possible to simulate the interactions of fluids and structures, it is computationally expensive and as a consequence experiments are needed to validate simplified models. Undertaking these experiments is not trivial, and unavoidably, the data collected can contain outlier / anomalous data points. There have been many attempts to create algorithms to automatically remove and or replace these outliers, the most effective or which are based on modal decomposition techniques. In fluid mechanics there are two prominent modal decomposition techniques. These are Proper Orthogonal Decomposition (POD), which can be use to determine modes that are spatially independent, and Dynamic Mode Decomposition (DMD) which can be used to determine modes that are temporally independent.

The majority of the previous POD and DMD applications have been have been applied to mechanical and aerospace engineering problems. However, the focus of this thesis is the application of modal decomposition techniques solely in Civil Engineering. First, the modal decomposition technique POD, is used to create a novel computationally efficient method for filtering spurious points from experimental data. Second a method of combining POD and DMD to attain regions of spatial and temporal independence is proposed. Third, these methods are applied to a river groyne problem to explain the spatio-temporal mechanisms leading to the sudden expansion of a mixing layer. Finally, these methods are applied to a

group of multi-scale square cylinders, resembling the layout of a city, to describe the spatio-temporal behaviour of the wake.

This thesis creates a suite of tools which can be applied by Civil Engineers to understand complex mechanisms, for instance, in environmental fluid mechanics.

Preface

This thesis is a 'thesis by papers' created from papers either published or submitted:

P1 Higham J.E., Brevis, W., Keylock, C.J. A rapid filtering and reconstruction method of two-dimensional image velocimetry signals using a non-iterative POD-method. Measurement Science and Technology 27.12 (2016): 125303.

P2 Higham, J.E., Brevis, W., Keylock, C.J. Implications of the selection of a particular modal decomposition technique for the analysis of shallow flows. Submitted to Journal of Hydraulic Research.

P3 Higham, J.E., Brevis, W., Keylock, C.J., Safarzadeh, A. Using modal decompositions to explain the sudden expansion of the mixing layer in the wake of a groyne in a shallow flow. Submitted to Advances in Water Resources.

P4 Higham, J.E., Brevis, W. Modification of the modal characteristics of a square cylinder wake obstructed by a multi-scale array of obstacles. Submitted to Experimental, Thermal and Fluid Science.

In chapter one a brief overview of themes presented in all of the papers is presented. Chapter two contains the literature associated to all of the papers. In chapter three the results and findings from P1 are presented. In chapter four the results and findings from P2 are presented. In chapter five the results and findings from P3 are presented, and in chapter six the results and findings from P4 are presented and expanded. Finally, in chapter seven the conclusions of all of the chapters are summarised. It is also made clear to the reader that some additional data presented are the consequence of the review process.

Furthermore, each of the chapters/papers have been influenced by the following conference proceedings.

Conference Proceedings

- Higham J.E., Brevis, W., Keylock, C.J. (2016). Turbulent characteristics produced by a blockage of pre-fractal emergent obstacles. AFMC, Perth, Australia, December 2016
- Higham J.E., Brevis, W., Keylock, C.J. (2016). Turbulent characteristics produced by a blockage of multi-scale emergent obstacles. Multisolve Workshop, Imperial College London, September 2016
- Higham J.E., Brevis, Safarzadeh, A. (2016). An Investigation into the dynamics of coherent structures in a turbulent shallow flow with an emergent side wall obstacle. 11th European Fluid Mechanics Conference, Seville, Spain, September 2016.
- Higham J.E., Brevis, W., Keylock, C.J. (2016). Turbulent characteristics produced by a blockage of multi-scale emergent obstacles. Inaugural UK Fluid Conference, Imperial College London, September 2016
- Higham J.E., Brevis, W., Keylock, C.J. (2015). A rapid filtering and reconstruction method of two-dimensional image velocimetry signals using a non-iterative POD-method. Bulletin of the American Physical Society 60.
- Higham J.E., Brevis, W., Keylock, C.J. (2015) On the Large Scale Dynamics in the Wake of a Fractal Obstacle. Bulletin of the American Physical Society 60.
- Higham, J.E., W. Brevis, and C. J. Keylock (2014). A Rapid, Empirical Method for Detection and Estimation of Outlier Frames in Particle Imaging

Velocimetry Data using Proper Orthogonal Decomposition. The University of Sheffield Engineering Symposium Conference Proceedings Vol. 1. Vol. 1. Sheffield, 2014.

Acknowledgements

Throughout my Ph.D. there have been a number of people who have been there to help and guide me along the way.

My first set of acknowledgments, although not to a person are to the 'Natural Environment Research Council' and the Department of Civil & Structural Engineering at the University of Sheffield, for providing the funding to allow me to conduct my research.

My second set of acknowledgments are to my two supervisors or advisors (as they prefer to call themselves), Dr. Wernher Brevis & Dr. Chris Keylock, both of them have been there to support my research and my personal development. In particular I would like to acknowledge the help of Dr. Brevis (who I now think is fluent in most English curse words) for his hands-on support in my laboratory experiments. Additionally, I would like to acknowledge the help of Dr. Daniel Wise and the discussion I have had with Dr. Franck Nicolleau. Finally I would like to acknowledge the support of the technicians who have been there to lend me an all important hammer or two!

My third set of acknowledgments go to my family and friends for their support, particularly my mum who has been there at the end of a phone to listen to me rant. In the workroom (D105) we have had full blow stand up arguments over the use of tensors and turbulence closure methods, which has all be in good jest and I would like to acknowledge the input of the whole room. Outside of the university I would like to acknowledge my friends for being understanding and supportive, however, I am sure most of them still don't know what I do!

Finally I would like to acknowledge Dr. A. Safarzadeh, the John Hopkins Turbulence database, Dr. J. Hain and Dr. C. Kähler for some of the data presented

in this thesis. Dr. H. Wang (POD-OC) and Mr. A. Masullo for providing their algorithms (AWAMT).

Contents

List of Figures

List of Tables

Nomenclature

Abbreviations

AWAMT Adaptive Weighted Angle and Magnitude Threshold method

CFD Computational Fluid Dynamics

CNN Cellular Neural Networks

DMD Dynamic Mode Decomposition

DNS Direct Numerical Simulations

JHTDB John Hopkins Turbulence Database

LES Large Eddy Simulations

LSPIV Large Scale Particle Image Velocimetry

PCA Principle Components Analysis

PIV Particle Image Velocimetry

POD Proper Orthogonal Decomposition

POD-OC Proper Orthogonal Decomposition Outlier Correction

PODDEM Proper Orthogonal Decompositions Detection and Estimation Method

Q2CS Quasi two-dimensional Coherent Structures

RANS Reynolds Averaged Navier Stokes

SVD Singular Value Decompsitions

UOD Universal Outlier Detection

Greek Symbols

δt Sampling rate

ϵ_{RMS} measure of precision

λ diagonal of POD singular values

$\mathbf{\Phi}$ POD spatial modes

$\mathbf{\Psi}$ DMD spatial modes

μ dynamic viscosity

ν kinematic viscosity

$\overline{\epsilon}$ measure of accuracy

ρ density

σ cluster size parameter (PODDEM)

τ number of DMD modes

τ_I integral time scale

Mathematical Operators

$(\cdot)^*$ conjugate transpose

$(\cdot)^T$ transpose matrix operation

$(\cdot)^\star$ non-dimensional operator

δ_{ij} Kronecker delta

$\langle\cdot\rangle$ time-averaged

∇ gradient

$\nabla\cdot$ divergence operator

∇^2 Laplacian operator

σ standard deviation

Roman Symbols

η number of POD modes

$\mathbf{\Omega}$ vorticity

$\mathbf{C}$ POD temporal coefficients

$\mathbf{D}_\alpha$ DMD singular values

$\mathbf{M}$ Mask matrix (PODDEM)

$\mathbf{M}$ mask matrix (PODDEM)

$\mathbf{Q}$ DMD temporal coefficients

$\mathbf{S}$ POD singular values

$\mathbf{u}$ velocity field

$\mathbf{W}$ column vector transformed velocity fields

$\mathbf{W}^c$ corrected dataset (PODDEM)

$\mathbf{x}$ spatial coordinates

$\mathcal{R}_{ij}$ Reynolds stress tensor

Ω_0 spatial-temporal averaged vorticity

f_0 sampling frequency

g acceleration of gravity

m_b size of sub divided region (PODDEM)

N size of column in input matrix $\mathbf{W}$

n_b size of sub divided region (PODDEM)

N_c	size of outlier clusters
p	pressure field
Q	outlier rate (PODDEM)
Q	outlier rate
Q_0	flow rate
S_n	shallowness number
T	maximum temporal coordinate
t	time
$t_r\%$	user defined percentage (PODDEM)
u	streamwise velocity component
u'_{rms}	root-mean-square of fluctuating streamwise velocity component
v	spanwise velocity component
v'_{rms}	root-mean-square of fluctuating spanwise velocity component
W^A	DMD input matrix
W^B	DMD input matrix
X	maximum streamwise coordinate
Y	maximum spanwise coordinate
a	POD-OC robust parameter
B	width of channel
BR	blockage ratio
C_f	friction coefficient
Fr	Froude number

H	water depth
L	characteristic length scale
Re	Reynolds number
Re_D	cylinder Reynolds number
S_D	cylinder spacing
St	Strouhal number
U_0	bulk velocity
x	streamwise spatial coordinate
y	spanwise spatial coordinate
z	vertical spatial coordinate

To my darling [*insert name here*], this thesis is dedicated to you because [*insert heartfelt quote here*] ...

Chapter 1

Introduction

1.1 Environmental flows: a stochastic process

The natural environment surrounds us with fluids. In the context of Civil Engineering, the large scale turbulent motions of these fluids are extremely important as it is their complex motions that are responsible for the mixing of pollutants, the erosion of river banks, and the oscillations of bridges and buildings. The motion of any incompressible fluid is governed by the Navier-Stokes and continuity equations:

$$\frac{D\mathbf{u}}{Dt} = -\frac{1}{\rho}\nabla p + \nu\nabla^2\mathbf{u} + \vec{g} \tag{1.1}$$

$$\nabla \cdot \mathbf{u} = 0 \tag{1.2}$$

where $\mathbf{u}$ and p are velocity and pressure fields, $\vec{g}$ is the acceleration of gravity, t is time, ρ is density, ν is the kinematic viscosity, ∇ is the gradient operator, ∇^2 is the Laplacian operator and $\nabla\cdot$ is the divergence operator. Eq. 1.1 is derived

from Newton's second law applied to a infinitesimal volume of fluid. On the left hand side of the equation, is the advective term, which governs the rate of change of the velocity of the volume of fluid as it moves along its trajectory. The right hand side represents the viscous forces and pressure gradient that act upon the advected volume. In short, the state of a fluid is constantly changing in space and time therefore its spatio-temporal characteristics are stochastic. By using the bulk velocity U_0 and a characteristic length scale L the terms of Eq. 1.1 can be non-dimensionalised:

$$\mathbf{u}^\star = \frac{\mathbf{u}}{\mathrm{U}_0}, \qquad \mathrm{t}^\star = \frac{\mathrm{t}\ \mathrm{U}_0}{\mathrm{L}}, \qquad \mathrm{p}^\star = \frac{\mathrm{p}}{\rho \mathrm{U}_0^2} \tag{1.3}$$

where $(\cdot)^\star$ denotes non-dimensionalised . When these terms are substituted in the Eq. 1.1 the equation becomes:

$$\frac{D\mathbf{u}^\star}{Dt^\star} = -\nabla \mathrm{p}^\star + \frac{1}{\mathrm{Re}}\nabla^2 \mathbf{u}^\star \tag{1.4}$$

$$\mathrm{Re} = \frac{\mathrm{L}\ \mathrm{U}_0}{\nu} \tag{1.5}$$

where Re is a dimensionless parameter. As demonstrated by Eq. 1.5, Re relates the viscous to the inertial forces. This single parameter, the Reynolds number, is extremely important across all scales of fluid mechanics as it defines the transition of a flow from a laminar to a turbulent state. Whilst this was not mathematically proven by Reynolds rather by Stokes (1851). The Reynolds number was name after Reynolds by Sommerfeld (1908) for his experimental investigations (see Fig. 1.1) and his mathematical decomposition (Reynolds 1885):

$$u_i = \langle u_i \rangle + u_i', \tag{1.6}$$

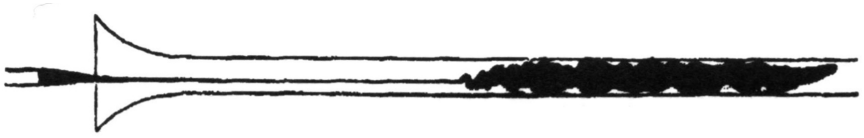

FIGURE 1.1: A sketch from Reynolds' 1883 paper (Reynolds 1883) of his experimental investigations of the transition of a fluid from a Laminar state to a Turbulent state.

The decomposition separates the fluctuating part of the flow, u_i', from the mean flow $\langle u_i \rangle$, where u_i is the velocity vector in each direction. By applying this decomposition to the steady-state incompressible Navier-Stokes equations Eq. 1.1:

$$\rho \langle u_j \rangle \frac{\partial \langle u_i \rangle}{\partial x_j} = \rho g + \frac{\partial}{\partial x_j} \left[-\langle p \rangle \delta_{ij} + \mu \left(\frac{\partial \langle u_i \rangle}{\partial x_j} + \frac{\partial \langle u_j \rangle}{\partial x_i} \right) - \rho \langle u_i' u_j' \rangle \right], \tag{1.7}$$

One can attain the Reynolds Averaged Navier-Stokes equation (RANS), where μ is the dynamic viscosity, δ_{ij} is the Kronecker delta. As shown on the right hand side of the equation the fluctuation components are a stress term: The Reynolds stress tensor ($\mathcal{R}_{ij} = -\rho \langle u_i' u_j' \rangle$). This term is extremely important as it is a measure of momentum flux and as a consequence, from a Civil Engineering perspective, is pivotal for understanding turbulent processes such as bed scouring and pollutant mixing.

While Reynolds should rightly be credited for this decomposition, plaudits must also be given to da Vinci and his early of sketches of turbulence, who 400 years before Reynolds, qualitatively described the Reynolds decomposition (see Fig. 1.2). In the text accompanying the sketches da Vinci likening a turbulent flow to hair with two motions: one due to the weight of the hair; the other due to the curls. Throughout this thesis there is much reference to these curls, which are formally defined as vortices or eddies. Where vorticity $\boldsymbol{\Omega}(\mathbf{x}, t)$ is defined by $\nabla \times \mathbf{u}(\mathbf{x}, t)$.

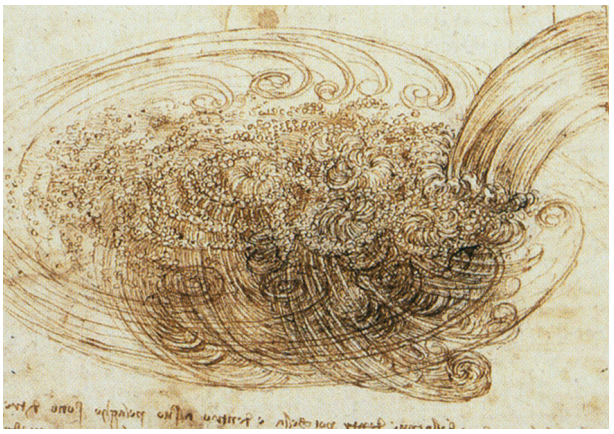

FIGURE 1.2: A drawing from the notebooks of Leonardo da Vinci. "A study of turbulent water flow" (da Vinci et al. 1970).

1.2 The different scales of turbulence

The Reynolds decomposition shows that the stochastic part of a turbulent flow is associated with the fluctuations. These fluctuations can be related to the turbulent structures that make up the flow (as shown by da Vinci). Richardson (1922) proposed a space filling picture of these turbulent structures (see Fig. 1.3) where the largest scales remove energy from the mean flow. The interaction amongst the turbulent structures, of various scales, passes energy sequentially from the larger turbulent structures gradually to the smaller ones until finally viscosity dominates and the energy is dissipated. This process is known as the turbulent energy cascade. Taylor (1938) later statistically described this cascade using an energy spectrum to describe the different scales. Within this spectrum there are three classifications of turbulent length scales:

- The integral length scales, which are a measure of the large scale turbulent structures in the production range.
- The Taylor micro-scales, which define length scales at which the turbulent structures begin to cascade down their energy.

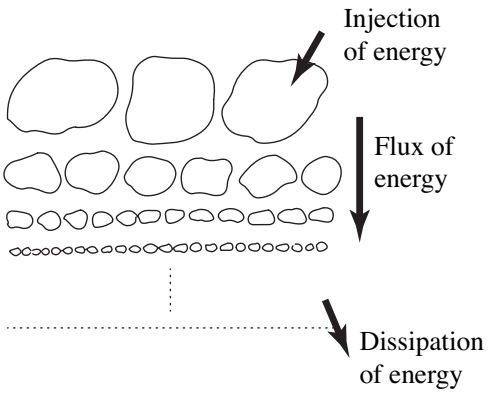

FIGURE 1.3: The energy cascade of turbulence modified from (Frisch & Donnelly 1996)

- The Kolmogorov micro-scales, which define the smallest turbulent structures within the flow.

Both Richardson & Taylor suggested that the rate of energy dissipation was universal and for certain cases this was proven by Kolmogorov (Kolmogorov 1941, 1962). However, there is still much debate surrounding the universality of this solution (e.g. Belchov & Yaglom (1971), Kraichnan (1967), Batchelor (1969)).

This energy cascade and the smaller length scales are extremely interesting and the focus of much theoretical research such as in physics and maths. However, as the focus of this thesis is on environmental flows in Civil Engineering, only the largest scales, the integral scales, are considered as it is these scales which contain the most turbulent kinetic energy and are responsible for large changes in momentum.

1.3 Coherent structures

In the last decade, a large part of the research in fluid dynamics has moved away from the development of statistical models and has concentrated on the identification and description of the dynamics of the so-called coherent structures. Whilst there is no fixed definition a number of authors have proposed their own definitions. Hussain (1983) first described a coherent structure as, "a connected, large-scale turbulent fluid mass with a phase-correlated vorticity over its spatial extent,". More recently Adrian (2007), Adrian & Marusic (2012) defined coherent structures to be coherent motions of individual entities, which significantly contribute to the mean flow and momentum fluxes, but are not exclusively spatially coherent. Whilst there still may not be a universal definition, it is agreed that coherent structures are spatially and temporally coherent and are the building blocks of turbulent flows.

In fluid mechanics there are several ways to identify these coherent structures. Some of them are based on the identification of invariants of the velocity gradient tensor (Hunt et al. 1988, Hussain 1983, Chakraborty et al. 2005), which is defined in terms of the spatial derivatives of the velocity field. In this context, some of the most used techniques to identify vortical structure are swirling strength (Zhou et al. 1999), Q-criterion, and lambda2 (Jeong & Hussain 1995). Other alternatives, based on a Lagrangian frame of reference, can be found for instance in the case of Lyapunov exponents (Green et al. 2007). Most of these methods allow the identification of instantaneous vortical structures, allowing their tracking and the extraction of important characteristics such as trajectories and lifetime. However, these methods are only based on instantaneous spatial statistics and do not

take into consideration the temporal evolution of the coherent structures. An alternative to these methods is based on the identification of the structures that statistically contribute the most to the variance of the signal under analysis, these methods are referred to as modal decomposition techniques. A classical fluid mechanics approach is the Proper Orthogonal Decomposition (Lumley et al. 1996) (POD). In the case of a velocity signal, the POD technique is able to identify those flow-structures that contribute the most to the turbulent kinetic energy, revealing their spatial structure (modes) and temporal dynamics (coefficients). The flexibility of the POD technique is highly recognised within the fluid mechanics community (Berkooz et al. 1993*a*) and previously has achieved great successes in: describing the large scale turbulent processes in shallow flows (Brevis & García-Villalba 2011); the use in modelling and control (Ly & Tran 2001); and has been used to describe the complex flow mechanisms associate to a cross jet Meyer et al. (2007). However, as highlighted by Schmid et al. (2009) one limitation of the POD technique is that it assumes that the turbulent mechanisms are linear, this is normally fulfilled by the dynamics of large–scale structures, but is generally not true in the global analysis of smaller scales of a turbulent field. A recent alternative that assumes a temporal orthogonality, different than the POD that assumes a spatial one, is the Dynamic Mode Decomposition (DMD) (Schmid et al. 2009, Rowley et al. 2009). DMD allows a better identification of coherent structures in a highly non-linear turbulent mechanisms, however one limitation is that it is not able to rank the resulting modes in terms of their contribution to a certain magnitude, as the POD does with the variance. To this authors knowledge, even though DMD may offer the key to describing coherent structures of temporal significance, it has only been successfully applied to highly theoretical works such as

lid driven cavities (Schmid et al. 2009), flames Schmid (2010) and simple geometries (Tu et al. 2014). If one to is assume the arguments of Adrian (2007), Hussain & Clark (1981) are correct, then clearly neither of these methods alone satisfy the definition of spatial and temporal coherence, but however, when combined they might.

1.4 Thesis structure

This thesis consists of seven chapters. The main results of this thesis are also presented in either accepted or submitted journal papers as highlighted in the preface.

- Chapter 1 has outlined the area of study.
- Chapter 2 presents a literature review relating to the aims of the thesis.
- Chapter 3 presents a novel filtering technique based on POD.
- Chapter 4 focuses on the integration of the POD and DMD, suggesting a means to extract turbulent structures with both spatio-temporal significance.
- Chapter 5 applies the POD & DMD to a river groyne case.
- Chapter 6 applies the POD & DMD to a multi-scale arrangement of square cylinders relating to a city layout.
- Chapter 7 concludes.

Chapter 2

Literature Review

As previously outlined this thesis is a 'thesis by papers'. The focus of this thesis is on the application of modal decompositions to two-dimensional Particle Image Velocimetry vector fields.

Each of the following chapters relate to the findings presented in four different, either submitted or accepted, papers. In this chapter the literature is divided into four sections, relating to the following chapters respectively:

- In section 2.1 the literature associated to experimental methods, data acquisition and outliers is presented.
- In section 2.2 the literature and methodology of modal decomposition techniques is outlined.
- In section 2.3 the literature associated to a turbulent shallow flows obstructed by to a single lateral groynes is presented.
- In section 2.4 the literature associated to fully three-dimensional turbulent flows obstructed by square cylinders is presented.

Whilst the different chapters may address different research topics, there are connected themes throughout the chapters.

2.1 Experimental methods

In fluid mechanics it is theoretically possible to simulate a turbulent flow using Direct Numerical Simulations (DNS), i.e. the direct numerical solution of the Navier-Stokes equations. However the computational resources required to calculate even the smallest of domains is very high and as a result the use of DNS for practical applications is very limited. If DNS is not practical the Navier-Stokes equations can be filtered and only the largest scales solved, for example in Large Eddy Simulations (LES) (Smagorinsky 1963), however, the effects and assumptions relating this filtering need to be taken into consideration when analysing the data. Instead of using DNS / LES, Reynolds Averaging can be applied to the Navier-Stokes equations and turbulence modelling can be used to close the resulting RANS equations, thereby reducing the computational effort required to simulate fluid flow. Although by time averaging, the dynamics of the fluids motions are lost. There are several popular closure methods, e.g. the $k-\varepsilon$ turbulence model, which assume isotropic turbulence as well as several empirically calibrated coefficients. So therefore, while it is technically possible to conduct experiments numerically, in practice such simulations require physical experimental data to validate the results and to derive empirical constants.

2.1.1 Particle Image Velocimetry

Particle Image Velocimetry (PIV) is a non-intrusive optical based technique which can be used to obtain instantaneous velocity measurements. Typically a flow is seeded with tracer particles, which respond to but do not affect the flow structures (Adrian et al. 2000). In some cases, but not all cases, illumination is required to highlight the particles located in a specific plane. Although in the case of shallow flows floating particles can be used (Safarzadeh & Brevis 2016). The motions of the particles are captured using digital cameras, and the displacement of the particles are calculated using correlations.

In standard two-dimensional PIV only two velocity components are attained. However, with the addition of a second camera it is also possible to use stereo reconstructions to attain a third component. Recent advances in experimental techniques have shown that further increasing the number of cameras it is possible to attain a three-dimensional volume of all three velocity components, however, typically these applications are limited to small volumes and are extremely heavily computational. For a deeper insight into flow measurement techniques the reader is directed to Scarano (2012).

2.1.2 PIV outliers

Any minor error, such as flaws in the image acquisition, or inhomogeneities of the flow seeding, can lead to poor correlations between image pairs resulting in errors within the vector fields: these errors are often referred to as outliers. Ideally one should try to mitigate against all of these problems, but they are often unavoidable. As PIV sequences can contain thousands of vector fields, numerous

contributions have suggested approaches to automatically reduce the influence of outliers. Typically, these methods fall into three categories:

1. Methods which use local spatial statistics of the vector fields to separately detect and estimate outliers.

2. Methods which spread or smooth the influence of outliers within the data fields.

3. Methods which use spatio-temporal features obtained from statistical approaches, such as POD, to detect and or estimate outliers.

The most common of these methods are based on spatial statistics. Westerweel (1994) suggested three methods for outlier detection by comparison of local statistics: 'local-mean'; 'local-median'; and 'global-mean'. The 'local-median' method was found to be most accurate, but not practical, as *ad hoc* thresholds are required for different flow regimes. By normalising the residuals of the local medians with respect to a robust estimate of the local variation of the velocity, the 'local median' method was improved, resulting in the 'Universal Outlier Detection' (UOD) approach (Westerweel & Scarano 2005*a*). This method is popular, but struggles to detect groups of outliers due to their influences on the local statistics. As a consequence, the 'Adaptive Weighted Angle and Magnitude Threshold method' (AWAMT) (Masullo & Theunissen 2016) was developed to improve the UOD approach. As in the UOD method, AWAMT detects outliers by comparing local statistics in the local neighbourhood. However, the AWAMT dynamically adapts the size of the neighbourhood to account for larger clusters. Furthermore, AWAMT normalises residuals with respect to a vector's magnitude and angle, adopting a modified Gaussian weighted distance-based averaging median. Masullo & Theunissen (2016) found AWAMT to improve on the UOD method for the detection

of clusters of outliers and in the overall accuracy of detection. A more complex method of outlier detection uses Cellular Neural Networks (CNN) to create a detection scheme by obtaining stable states of neurons. However, the robustness and accuracy of the method was found to be comparable only to the 'local-median' method (Liang et al. 2003).

These methods described above only detect outliers which means that an interpolation scheme is still required. As these methods calculate outliers locally i.e. in single vector fields, it is intuitive to use simple local statistical methods such as linear, bi-linear, spline or more complex mathematical models, such as Kriging (Gunes et al. 2006). Consequently, these local methods are dependent on the characteristic length scales of the flow and on the resolution of the acquired images. Alternatively, if outliers in several vector fields of the sequence are detected, an iterative POD based method such as 'Gappy POD' (Everson & Sirovich 1995) can be used. Gappy-POD and Kriging are comparable in effectiveness and Gappy-POD has been further developed with the Adaptive Gappy-POD formulation (Raben et al. 2012). However, these methods are computationally expensive and impractical for the long vector field sequences found in some PIV measurements (Gunes et al. 2006). An alternative method recently proposed in fluid mechanics is the 'All-in-one' method (Garcia 2010, 2011), based on the combination of penalised least squares techniques, discrete cosine transforms and the generalised cross-validation method. Whilst the aim of the method is to reduce the influence of the outliers, Wang et al. (2015) notes this method can weaken instantaneous velocity fluctuations and gradients.

A recent iterative, spatio-temporal statistical method, which couples the detection and estimation of outliers using a POD, is the POD-Outlier Correction method or POD-OC (Wang et al. 2015) . This method assumes that outliers do not perturb

into the low-order POD spatial modes of a flow decomposition. It detects outliers by comparing each vector field to a residual calculated from the mean, standard deviation and a 'robust parameter' (a=3). The detected points are replaced using a low-order reconstruction and a second residual, this process is repeated until convergence of the POD spectrum based on user defined convergence criterion.

2.2 Modal decomposition techniques

As previously discussed the term coherent structure has no fixed definition. Modal decomposition techniques can be used to attain spatial or temporal coherences from a velocity signal (such as those attained from PIV). Two popular methods in fluid mechanics are the spatially orthogonal POD and the more recent temporally orthogonal DMD.

2.2.1 Proper Orthogonal Decomposition

The POD is a statistical method commonly used in fluid mechanics for the extraction and analysis of energy meaningful turbulent structures (Aubry 1991, Berkooz et al. 1993*b*). POD was independently derived by a number of individuals, consequently acquiring a variety of names in different fields including Karhunen-Loève Decomposition, Singular Value Decomposition (SVD) (Golub & Reinsch 1970) and Principal Components Analysis (PCA) (Kosambi 1943, Loève 1945, Karhunen 1946, Pougachev 1953, Obukbov 1954). POD extracts energy relevant structures (modes) from set of a stochastic, statistically steady-state turbulent fields, within a finite time domain, ordering them by their contribution to the total variance of the physical property being analysed, e.g. velocity (Brevis & García-Villalba

2011). A set of $t = 1, 2, \ldots, T$ temporally ordered vector fields,$\mathbf{u}(x, y; t)$, is considered, each of which is of size $X \times Y$. The method requires the construction of a $N \times T$ matrix $\mathbf{W}$ from T columns $\mathbf{w}(t)$ of length $N = XY$, each column corresponding to a column-vector version of a transformed snapshot $\mathbf{u}(x, y; t)$. A POD is obtained by:

$$\mathbf{W} \equiv \mathbf{\Phi}\,\mathbf{S}\,\mathbf{C}^{\mathrm{T}} \tag{2.1}$$

where $\mathbf{S}$ is a matrix of size $\eta \times \eta$, (η are the number of modes of the decomposition, and $(\cdot)^T$ represents a transpose matrix operation). The $\lambda = \mathrm{diag}(\mathbf{S})^2/(N-1)$ is the vector containing the contribution to the total variance of each η. The elements in λ are ordered in descending rank order, i.e. $(\lambda_1 \geq \lambda_2 \geq \ldots \lambda_\eta \geq 0)$. In practical terms the matrix $\mathbf{\Phi}$ of size $N \times \eta$ contains the spatial structure of each of the modes and the matrix $\mathbf{C}$ of size $\eta \times \eta$ contains the coefficients representing the time evolution of the modes.

2.2.2 Dynamic Mode Decomposition

The DMD algorithm was introduced into fluid mechanics by Schmid (2010) & Rowley et al. (2009), based on a Arnoldi Eigenvalue algorithm suggested by Ruhe (1984). However the use of this method, up until now, has been focused on solving highly theoretical problems e.g. ((Schmid 2010, 2011, Schmid et al. 2009)). Unlike POD, which is based upon a co-variance matrix, the DMD algorithm approximates the temporal dynamics by fitting a high-degree polynomial to a Krylov sequence of flow fields (Mezić 2005, Schmid et al. 2009). For complex flow systems containing superpositions of turbulent structures and mechanisms, the DMD algorithm can be used to extract spatial modes with single 'pure' frequencies. There are currently a number of methods by which one can compute a DMD, and the method used in

this thesis is the popular SVD based method; this approach has been shown to be less susceptible to experimental noise (Schmid 2010). The algorithm is outlined below, although the reader is directed to Schmid (2010), Jovanović et al. (2014), Tu et al. (2014) for the full mathematical description. The DMD algorithm begins with a similar transformation as POD:

$$\mathbf{W^A} = \{w_{t=1}, w_{t=2}, \ldots, w_{t=\tau}\}, \quad \& \quad \mathbf{W^B} = \{w_{t=2}, w_{t=3}, \ldots, w_{t=T}\} \tag{2.2}$$

where $\tau = (T-1)$, and the super-scripts A & B denote the two $\mathbf{W}$ matrices of size $N \times \tau$. A SVD of $\mathbf{W^A}$ is computed, such that:

$$\mathbf{W^A} \equiv \tilde{\mathbf{\Phi}}\tilde{\mathbf{S}}\tilde{\mathbf{C}}^T. \tag{2.3}$$

where $\tilde{\mathbf{\Phi}}, \tilde{\mathbf{S}}$ & $\tilde{\mathbf{C}}$ are the POD modes (Eigenvectors), the Eigenvalues and the temporal coefficients of $\mathbf{W^A}$ respectively. The matrix $\mathbf{F}$, of size $(\tau \times \tau)$, is created by:

$$\mathbf{F} = \tilde{\mathbf{\Phi}}\mathbf{W^B}\tilde{\mathbf{C}}\tilde{\mathbf{S}}^{-1} \tag{2.4}$$

and its complex Eigenvalues, μ_i, and Eigenvectors, z_i, are computed where $i = 1 \ldots \tau$. At this point the method of Jovanović et al. (2014) is used, as this creates a set of amplitudes for each spatial mode. Following Jovanović et al. (2014) a Vandermonde matrix is created from the complex eigenvalues:

$$\mathbf{Q}_{i,j} = \mu_i^{(j-1)} \tag{2.5}$$

where $i = 1 \ldots \tau$ & $j = 1 \ldots \tau$, and the spatial modes are created by $\mathbf{\Psi} = \tilde{\mathbf{\Phi}}\mathbf{Z}$, where $\mathbf{Z}$ is the set of complex Eigenvectors previously computed. Furthermore, a set of amplitudes, $\mathbf{D}_\alpha$, are created and the original input, $\mathbf{W^A}$, can be expressed

as:

$$\mathbf{W^A} \equiv \mathbf{\Psi D}_\alpha \mathbf{Q} \tag{2.6}$$

where $\mathbf{D}_\alpha$ is of size $\tau \times \tau$. Similar to a POD $\mathbf{\Psi}$, the spatial are modes of size $N \times \tau$ relating to the spatial structure, $\alpha = diag(\mathbf{D}_\alpha)$ relates to amplitude of the temporal coefficients, but not the variance of the DMD mode, and $\mathbf{Q}$ contains the coefficients representing the time evolution of the modes. In practical terms, the angle between the real and imaginary part of, z_i, can be used to describe the frequency relating to each $\mathbf{\Psi}$ and expressed as a frequency (f_i) or Strouhal number (St_i) by:

$$f_i = 2\pi f_0 \arg\{z_i\} \quad \& \quad \mathrm{St}_i = (2\pi \mathrm{U}_0 f_0 \arg\{z_i\})/\mathrm{L} \tag{2.7}$$

where, $i = 1 \ldots \tau$, L is characteristic length scale, U_0 is the bulk velocity and f_0 is the sampling frequency.

2.3 Shallow flows and river groynes

The main effect caused by the forcing of a topographical obstruction in a turbulent shallow flow is the generation of highly energetic coherent structures (Jirka 2001). Due to the constraints imposed by the water depth on the vertical vortex stretching process, these coherent structures grow sidewise, developing a mainly horizontal dynamics. This means that their structure is almost two-dimensional everywhere on depth, except near the bottom where the boundary layer governs the flow characteristics, i.e they behave as quasi-two-dimensional coherent structures (Q2CS) (Jirka 2004). Besides the Reynolds number, Q2CS are mainly characterised by the Shallowness number $S_n = C_f D/H$, where C_f is the friction coefficient, D a characteristics length scale and H the water depth (Chen & Jirka 1997, Uijttewaal

2014, Constantinescu et al. 2009). Due to the high energy of Q2CS, their dynamics can be crucial to understand important process such as momentum and mass exchange, and the dynamic loads exerted by a flow over hydraulics infrastructure. It is because of this that the description of their spatial characteristics and temporal dynamics is paramount in the context of environmental process and hydraulic engineering.

In natural flows such as rivers and estuaries, groynes are installed to prevent bank scouring (Kuhnle et al. 1999, Koken & Constantinescu 2008), create and enhance fish habitats (Grift et al. 2003) and to improve navigation (Brevis et al. 2014). The majority of these natural flows are bounded flows in a domain for which two dimensions, namely that in the direction of the flow, as well as one traverse dimension, greatly exceed the third dimension, consequently they fulfil definition of a shallow flow (Jirka 2004).

Dependent upon the magnitude of the transversal velocity gradient, a topographical obstruction of any flow can lead to the formation of a mixing layer. In contrast to in deep flows, the large-scale coherent turbulent structures which populate the far field of a shallow mixing layer, can almost extend the whole depth of the flow. As a consequence Q2CS, and their spatio-temporal dynamics, are easily influenced by bed-friction (Nadaoka & Yagi 1998, Uijttewaal & Tukker 1998, Chu & Babarutsi 1988, Socolofsky & Jirka 2004). From an environmental perspective these Q2CS are of great significance, as their spatio-temporal behaviour governs mass and momentum exchange. Some examples of this can be found in their key role to predict the concentration of pollutants, nutrients and the rates of sediment transport (Rhoads & Sukhodolov 2004, Boyer et al. 2006, Sukhodolov & Rhoads 2001, Cheng & Constantinescu 2014).

Many previous works have investigated the spatio-temporal dynamics of Q2CS created by plane shear instabilities e.g. (Chu & Babarutsi 1988, Uijttewaal & Tukker 1998, Rhoads & Sukhodolov 2004), and have shown that due to the effects of bed-friction the spread/growth rate of a shallow mixing layer is modified. In an experimental study to investigate the effect of topographical forcing on a shallow flow, Talstra et al. (2006) found that unlike in a deep flow, (Armaly et al. 1983), the shallow flow mixing layer bound a second counter rotating recirculation cell. They also found at the downstream edge of the first recirculation cell there was a sudden expansion in the mixing layer, which they hypothesised to be associated to the shearing interface between the two counter rotating cells. In a recent study, this sudden expansion was also found to occur when a shallow flow was obstructed by a single lateral groyne, it was also observed that the length of reattachment of the mixing layer with the wall was protracted compared with the a deep case (Safarzadeh & Brevis 2016, Safarzadeh et al. 2016). A number of time-averaged experimental studies have previously investigated this case, but have neither observed or explained this phenomena (Duan et al. 2009, Ahmed et al. 2010, Kadota & Suzuki 2010, Francis et al. 1968). RANS (k-ω) simulations of Chrisohoides et al. (2003) observed the dual cell system and found that it was stable but periodically horizontally expanding and contracting. They further found that eddies from upstream and shed from the tip of the obstacle were engulfed by the second downstream recirculation cell, and as the mixing layer reattached with the lateral wall, vorticity was injected back upstream; however they did not observe a sudden expansion the mixing layer. Safarzadeh & Brevis (2016) recently explained that due to the anisotropy associated to the flow system, RANS simulations, based on isotropic closure models, will not be able to simulate the expansion of the mixing layer or predict the length of reattachment. Other Computational Fluid Dynamics

(CFD) studies relating to a single groyne have only focused on the turbulent mechanisms upstream and in the near wake of the groyne e.g. (Garde et al. 1961, Koken & Constantinescu 2009, 2008, Paik & Sotiropoulos 2005, Koken 2011), whilst not directly related to this study it is inferred that these complexities have implications on the dynamics of the mixing layer downstream. From all of these findings it is clear that the dynamics of a shallow mixing layer produced in the downstream wake of a single groyne are complex and non-linear.

2.4 Urban morphology: multi-scale arrays of square cylinders

Urban morphology presents descriptive and analytical challenges for researchers in many different disciplines. Even considered only in terms of their physical structure, cities are very complex systems, teeming with detail and variation; this makes the modelling of urban morphology not only difficult but computationally resource-intensive.

The turbulent wake produced by a single square cylinder is a well known fluid mechanics problem, but it is still of much interest today, especially in the built environment due to the direct applicability to high-rise buildings (Huber 1988, Huber et al. 1991). For a square cylinder, unlike a circular one, the separation points of the flow are fixed, meaning the properties of the wake in a turbulent flow are relatively insensitive to changes of the Reynolds number (Okajima 1982, Dutta et al. 2003), Re_D=U_0D/ν, D is the side length of the square cylinder. However there are a number other parameters which modify the wake properties. Significant effects can be caused by changes of the incoming turbulent intensities,

$u'_{rms}/\langle u \rangle$. A higher $u'_{rms}/\langle u \rangle$ induces a rise in the base pressure, leading to a reduction in the mean drag (Lee 1975). In addition, an increase of the base pressure can cause a protracted position of the reattachment point of the separated shear layers (Bearman & Trueman 1972). Another effect of an increased $u'_{rms}/\langle u \rangle$ is an expansion of the thickness of the separated shear layers (Lee 1975) and a decrease of the vortex shedding frequency (Batham 1973, Gerrard 1966, Bearman 1967). This evidence suggest that for a constant Re_D, the lower the drag, the furthest downstream the position of the reattachment point, thus the larger the recirculation bubble.

Another important parameter controlling the properties of the wake is the confinement or blockage ratio, BR=D/B , where B is the width of the channel. Richter & Naudascher (1976), Mukhopadhyay et al. (1992), Davis et al. (1984) concluded that the confinement of a cylinder can increase the drag and the vortex shedding frequency. Based on the reduction of drag, this could imply a decreased size of the recirculation bubble.

In the context of the flow around two twin square cylinders separated in the spanwise flow direction, Kolar et al. (1997) found that positioning two square cylinders close to each other could have an important effect on the properties of the individuals and combined wake. They found when the cylinders are separated by spacing $\mathrm{S}_D \lesssim 1.1\mathrm{D}$, they acted as a single bluff body, but with a reduced drag. At a greater spacing $1.1\mathrm{D} \lesssim \mathrm{S}_D \lesssim 2.2\mathrm{D}$ the individual wakes were bi-modal, and directed towards one of the cylinders. Finally when the spacing was $\mathrm{S}_D \gtrsim 2.2\mathrm{D}$, in the near field, the wake of both cylinders acted independently. Analogously, but in the context of the flow around square cylinders in a longitudinal tandem arrangement, Liu & Chen (2002), Zhou & Yiu (2006) observed that if two cylinders were placed in a streamwise tandem, the separation affects the properties of

the furthest downstream wake. At $S_D \lesssim 2.0D$ the cylinders acted as a single body and the frequency of vortex shedding spectrum was broadband around the peak frequency. Increasing the spacing, $2.0D \lesssim S_D \lesssim 3.0D$, a recirculation region was created between the two cylinders. This region intermittently injects vorticity, also changing the properties of the wake (Lin et al. 2002). Finally $S_D \gtrsim 8.0D$ the two cylinder acted independently, however the vorticity of the structures shed downstream was reduced by the influence of the wake developed upstream. This means that, in an array, the distribution of elements should produce different resulting flow structures which should be a function of the gaps between the obstacles, and also the length scale of the cylinders involved. As a matter of fact previous work on the interaction between cylinders arranged in a stream- or spanwise orientation has shown that the wake generated by the largest cylinder dominates the flow, and that the characteristics of the resulting flow field are a function of the ratio between the cylinder sizes and the spacing between them (Chen & Shao 2013, Zhang et al. 2005, Kumar & Vengadesan 2009, Gao et al. 2010, Islam et al. 2017). Furthermore, even though it is possible to find in the literature studies characterising the arrays of square cylinders of uniform scales (Zong & Nepf 2012, Nicolle & Eames 2011), to the best of these authors knowledge there has been no reported research on the flow interactions produced by multi-scale arrays.

2.5 Summary

As discussed in Section 2.1 even for state-of-the-art experimental techniques it is still possible to acquire images which contain outlier data points. As typically large amounts of images are collected in a PIV investigation, it is not feasible to remove the outliers manually. As a consequence there have been a number of different methods proposed to remove these and replace these outlier. The most effective are based on a POD, however these techniques are only based on computationally expensive iterative methods which construct low-order models of the data to remove detect and remove the outliers.

Section 2.2 derives two modal decomposition techniques, the POD and the DMD. These methods can be used to determine spatially orthogonal (POD) and temporally orthogonal (DMD) turbulent structures. In flow cases containing complex spatial and temporal regions the POD is unable to determine regions of spatial and temporal coherence. The section also shows that the DMD is not able to rank resulting modes in terms of their contribution to the total turbulent kinetic energy, as in a POD.

Section 2.3 describes a spatio-temporal event occurring in the mixing layer of a shallow flow. Previous works have shown that the two dimensional turbulent structures relating to this region are extremely important as they govern mass and momentum exchange and the dynamic loads on hydraulic structures.

Finally, Section 2.4 shows that there has been little or no work investigating groups of multi-scale square cylinders, which directly relate to the built environment. Those works which have investigated small groups of square cylinders have found

that the spatio-temporal behaviours of the downstream wakes are heavily affected by the spacing and confinement of the cylinders.

2.6 Aims of the thesis

In this thesis the main concern is the general use of modal decompositions techniques to solve large scale problems associated to Civil Engineering. The general aim of this thesis is four-fold:

1. Development of experimental methods: Development of a novel POD technique to accurately remove and replace outliers with increased computational performance.

2. Application of modal decomposition techniques: Integration of POD and DMD techniques to improve the identification of shallow flow regions of high temporal and spatial importance.

3. Improved understanding of the dynamics of shallow flow structures: Investigation of the spatio-temporal mechanism leading to the sudden expansion of a mixing layer created by topographical forcing in a shallow flow.

4. Investigation of wakes in the built environment: Characterisation of the modal changes induced by surrounding elements of the wake of a square cylinder.

Chapter 3

A rapid non-iterative proper orthogonal decomposition based outlier detection and correction for PIV data

This chapter proposes a novel method of detection and estimation of outliers in PIV measurements by the modification of the temporal coefficients associated with a POD of an experimental time series. Using synthetic outliers applied to two datasets obtained from the John Hopkins Turbulence Database (JHTDB) (Li et al. 2008) and real PIV vector fields obtained from (Hain & Kähler 2007) the method is benchmarked against state-of-the-art approaches recently proposed to remove the influence of outliers. Compared with these methods, the proposed approach offers an increase in accuracy and robustness for the detection of outliers and comparable accuracy for their estimation.

3.1 POD outlier Detection & Estimation Method (PODDEM)

A methodology for the detection and estimation of outliers in every vector field of a dataset, through the modification of the results of a POD is proposed. In Appendix A the mathematical reasoning for which is given. Unlike other POD-based methods, the proposed method is non-iterative, and hence less computationally expensive. Alternative POD-based methods are built on modifications of $\mathbf{\Phi}$, while the present one relies on changes to $\mathbf{C}$. The present method is based on the observation that outliers in every vector field in a time series can produce spikes or a noisy evolution of $\mathbf{C}$ (see Fig. 3.2). The hypothesis of this work is that a suitable correction of $\mathbf{C}$ can be used to reduce the influence of outliers in the time series. As summarised in algorithm 3.1, this is achieved as follows:

(a) A POD, as shown in Eq. (2.1), is performed on the input matrix $\mathbf{W}$ (in this study only two velocity components are used).

(b) A moving average filter is applied to each POD coefficient vector $\mathbf{c}_n$, where $n = 1 \dots \eta$. These vectors correspond to column components of $\mathbf{C}$. In this work a convolution kernel size of 0.01 of the spatially averaged integral time scale, $0.01\tau_I$, was used during the moving averaging procedure. $0.01\tau_I$ for a kernel size was found to be effective in the test cases presented in the present study, as the kernel was large enough to remove the smaller scale noise, but not large enough to affect the temporal evolution of $\mathbf{C}$, a sensitivity analysis can be found in the Appendix A (Figs. A.1 & A.2), in which multiple factors the of τ_I were investigated on all cases to find an optimum value for both detection

and estimation. The resulting vectors are stored in $\mathbf{C}^E$, an estimated version of $\mathbf{C}$.

(c) A new $\mathbf{W}^E$ is created, using Eq. (2.1), $\mathbf{W}^E = \mathbf{\Phi S}(\mathbf{C}^E)^T$.

(d) A matrix $\mathbf{W}'$ is created from $|\mathbf{W} - \mathbf{W}^E|$, where $|\cdot|$ represents the absolute value operation.

(e) Similar to previous approaches, a mask matrix $\mathbf{M}$ of the same size as $\mathbf{W}$ is introduced, in which each element is assigned the value 1.

(f) The columns of $\mathbf{W}'$ are sorted in descending order. The locations of $\mathbf{W}'$ corresponding to the first $t_r\%$ (user defined percentage, relating to the ratio of the number of outliers to total number of vectors in the dataset) of the sorted $\mathbf{W}'$ are assigned a 0 in $\mathbf{M}$.

(g) Using a simple operation a corrected version $\mathbf{W}^c$ of $\mathbf{W}$ is obtained: $\mathbf{W}^c = \mathbf{W} \cdot \mathbf{M} + \mathbf{W}^E \cdot (1 - \mathbf{M})$, where $\cdot$ corresponds to the inner product operation. More simply: the valid data, i.e. those with elements of $\mathbf{M}$ with value 1, are retained, while the detected outliers are replaced by those calculated in $\mathbf{W}^E$.

3.1.1 Selection of test cases

In this study two datasets from the JHTDB are used for a quantitive assessment. These data are chosen due to the availability of long time series. 1000 vector fields are selected for each case, each of them containing 64×64 grid points. The first dataset selected is a subset of a DNS of a channel flow (Graham et al. 2016). The origin of the selected section is located at $x = 18.2, y = -0.99$, and $z = 6.6$. From that point, 64 points are taken in the x and y positive direction, at a spacing of

Require: A sequence of T vector fields transformed into a matrix $\mathbf{W}$ and a user defined percentage $t_r\%$.
Output: A matrix $\mathbf{W^c}$ with outliers removed. The columns of $\mathbf{W^c}$ can be reshaped to obtain a filtered version of the sequence of vector fields.

$\mathbf{W} \leftarrow \{w_1, w_2 \dots w_T\}$,
$[\mathbf{\Phi}, \mathbf{S}, \mathbf{C}] \leftarrow \text{SVD}(\mathbf{W})$.
$\mathbf{C}^E \leftarrow \mathbf{c}_n^E \leftarrow \text{movingaverage}(\mathbf{c}_n, 0.01\tau_I)$; where $n = 1 \dots \eta$,
$\mathbf{W}^E \leftarrow \mathbf{\Phi S C}^{E^T}$,
$\mathbf{W}' \leftarrow |\mathbf{W} - \mathbf{W}^E|$,
$\mathbf{M_{ij}} \leftarrow 1$,
$\mathbf{M_{ij}} \leftarrow 0$, corresponding to locations of top $t_r\%$ of sort$(\mathbf{W}_{ij})$,
$\mathbf{W}^c \leftarrow \mathbf{W} \cdot \mathbf{M} + \mathbf{W}^E \cdot (1 - \mathbf{M})$.

Algorithm 3.1: PODDEM

0.01. The selected domain size is equal to $8\pi \times 2\pi \times 3\pi$. For the construction of the time series, this region was sampled with a $\delta t = 0.012$; on average the dataset contains 9 integral time scales, $\tau_I = 9$. The second dataset is a subset from the DNS of a forced homogenous isotropic turbulence. The origin of the selected region was located at $x = 0$, $y = 0$, and $z = 0$. From the origin, 64 points are taken in the x and z positive direction, at a spacing of 0.015. The total size of the sampled region is $2\pi \times 2\pi \times 2\pi$. The temporal sampling is performed with a $\delta t = 0.012$ and on average 6 integral time scales $\tau_I = 6$.

According to Shinneeb et al. (2004), PIV measurements can contain two types of outliers: single spurious vectors, and clusters of spurious vectors, the latter of the two being more common. As the datasets obtained from JHTDB are outlier-free, synthetic outliers were introduced in the time series. As the synthetic data is added to the data it is possible to quantify the accuracy of the detection and estimation methods. For comparison purposes the same method of synthesising outliers developed by Wang et al. (2015) is used to benchmark the proposed method. An

outlier rate is introduced, Q, defined as the percentage of outliers in each vector field. In the case of single distributed outliers, a random location is obtained from a uniform random function. Similarly to previous works, the magnitude of the x and y components of these outlier vectors are drawn independently from a uniform distribution $[-u_{max}, u_{max}]$, where u_{max} is the maximum magnitude of velocity in the entire data. In the case of clusters of outliers, an analogous approach to the one presented by Shinneeb et al. (2004) is adopted, in which, a parameter N_c is also introduced. This parameter defines the number of vectors involved in a certain cluster of size $G(N_c)$; however, the total number of outlier vectors in each snapshot remains defined by Q. A distribution similar to the one used by Garcia (2011) is adopted for the determination of the size of the clusters:

$$G(N_c) = A \cdot exp(-N_c^2/\sigma^2) \tag{3.1}$$

where σ is the standard deviation of the size distribution, and A is a parameter defining the size of a cluster corresponding to the mean number of elements. Different sizes of outliers are distributed throughout the datasets. As in Wang et al. (2015), the vectors within a cluster also are of a similar magnitude and values of $A = 0.4$ and $\sigma = 2.8$ are used. Several cases are tested in this work, involving $Q = 5\%$ and $Q = 15\%$. For these outlier rates, outlier clusters in the range $1 \leq N_c \leq 7$ are analysed. In Fig. 3.1, an example of a generated synthetic vector field is presented, where $Q = 5\%$ and $N_c = 1$.

Fig. 3.2 shows the spatial and temporal structure of the two leading POD modes for both test cases. It also shows the changes introduced by the outliers on the modes structure when $Q = 5\%$ and $N_c = 3$ are introduced. In both cases, the general patterns in the leading spatial modes remain as in the original time series,

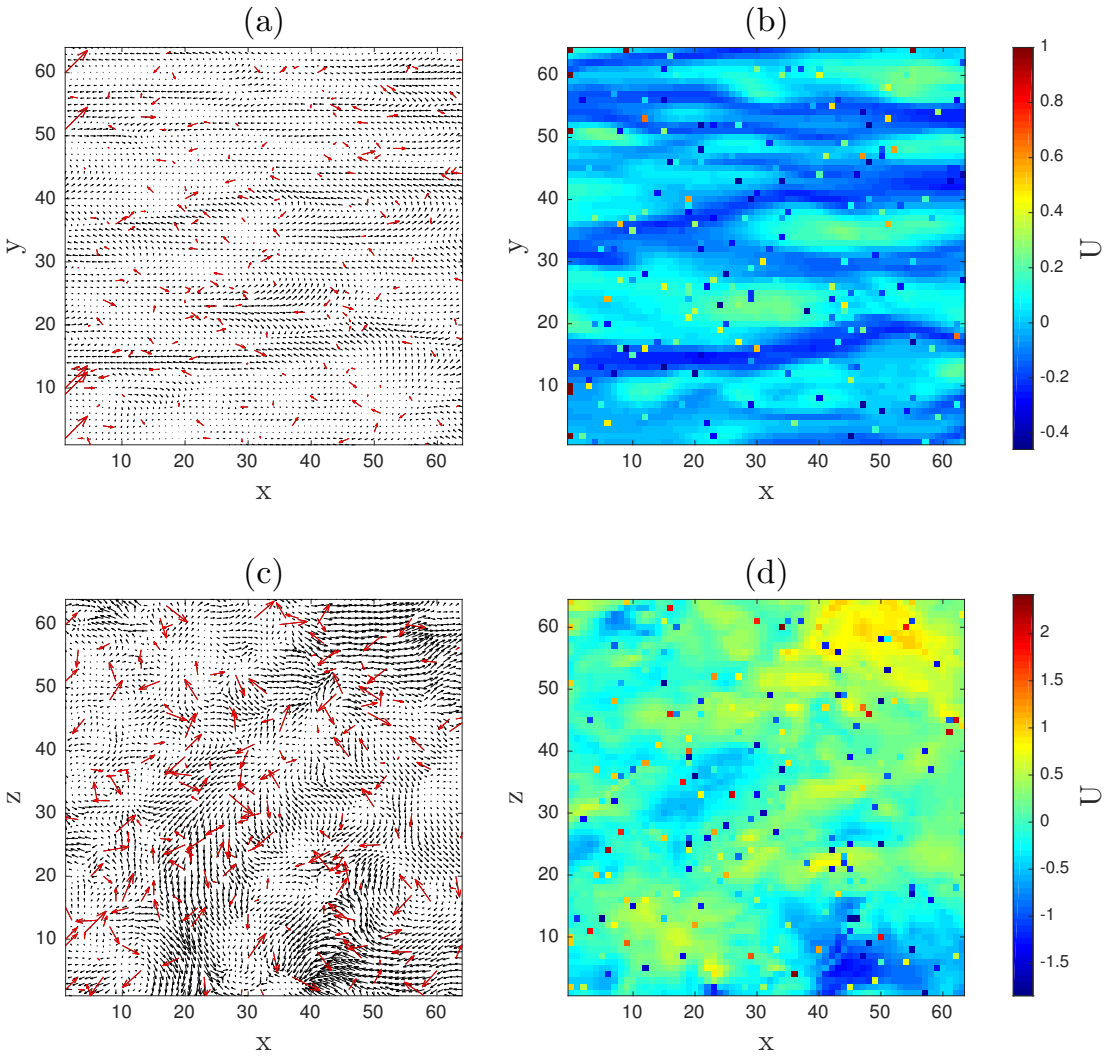

FIGURE 3.1: Synthetic vector fields from JHTDB numerical time series. Synthetic outliers are highlighted in red. $Q = 5\%$ and $N_c = 1$ have been used for these examples. (a) & (b) Two-dimensional vector fields and longitudinal velocity magnitude for channel flow, respectively. (c) & (d) Two-dimensional vector fields and longitudinal velocity magnitude for isotropic turbulence, where U is the streamwise component. The 500^{th} vector field in the sequence is shown.

but with a grainier structure. Qualitatively speaking, a more obvious effect of the outliers in the POD can be observed in the temporal POD coefficients. In both time series, it is observed that temporal behaviour can be effected by noise. While it is clear that, noise reduction in the two-dimensional spatial structure is possible, the strategy of correcting the temporal behaviour of the modes is followed in this work, leading to the development of PODDEM .

To supplement the quantitive assessment, a third 'real' experimental dataset is used, namely that of of the turbulent flow over periodic hills Hain & Kähler (2007). This data set contains single frame particle images acquired in the central plane of the channel, using hollow glass particles of $d = 10\mu m$ illuminated with a 5W Nd:YAG laser and recorded by means of a Phantom v12 camera. PIV processing is undertaken on 1000 sequential images using PIVLab (Thielicke & Stamhuis 2014); analogous to Hain & Kähler (2007) two passes are undertaken using interrogation windows of size 64×64 and 32×32 respectively, each with a 50% overlap. It is found that, on average, the data set contains $\tau_I = 6$. No synthetic outliers are introduced to the dataset.

3.1.2 Quantification of algorithm performance

An assessment of the algorithm's performance requires the introduction of criteria for error quantification. All elements are considered to establish the effect of false positive detections and following estimations on the error statistics. Following the criteria defined by Wang et al. (2015), the relative error ϵ_i between an unmodified element (obtained prior to the application of synthetic outliers) of the matrix $\mathbf{W}$,

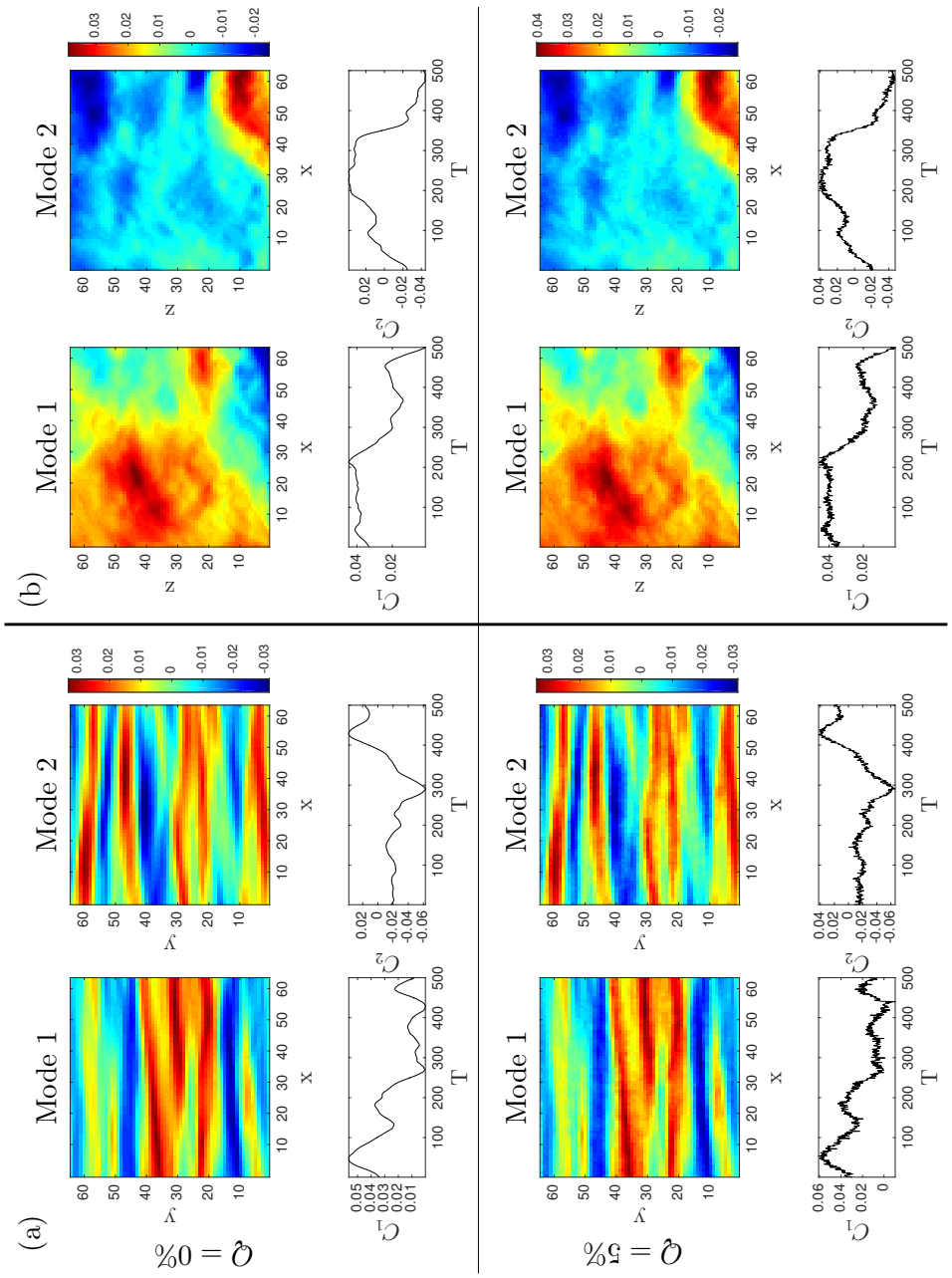

FIGURE 3.2: Example of the POD decomposition on the original and contaminated time series. The left column shows the results for the channel flow case. The right column corresponds to the isotropic case flow. The first row shows the results for the original time series. The second row shows the results for a contaminated time series with $Q = 5\%$ and $N_c = 3$. Even though differences in the spatial structures of the first two modes can be observed, the most evident differences can be seen in the noisier structure of the temporal coefficients associated with these modes.

w_i, and its estimated value w_i', can be defined as:

$$\epsilon_i = \frac{|w_i' - w_i|}{|w_i|}, \tag{3.2}$$

where the sub-index $i = 1...NT$ represents individual elements of $\mathbf{W}$. This means that the double-averaged error, i.e. spatial and temporal averaged relative error, $\overline{\epsilon_i}$, can be calculated as:

$$\overline{\epsilon_i} = \frac{1}{NT}\sum_{i=1}^{NT}\epsilon_i, \tag{3.3}$$

Using this definition the spatio-temporal root mean square (RMS) of the relative error can be calculated as:

$$\epsilon_{RMS} = \sqrt{\frac{1}{NT}\sum_{i=1}^{NT}(\epsilon_i - \overline{\epsilon_i})^2}. \tag{3.4}$$

Hence Eq. (3.3) is a means of characterising the accuracy of the various methods, whilst Eq. (3.4) is a measure of precision. A number of methods are chosen in order to benchmark the estimation functionality of PODDEM. The first method is the so-called POD-OC (Wang et al. 2015). As POD-OC has shown an increased accuracy in comparison with standard statistical methods, e.g. global-mean and linear interpolation, these latter methods are omitted from further consideration. The second comparative method is the All-in-one smoothing function of Garcia (2010), which is implemented using the MATLAB function 'smoothn'. Kriging has also been used for benchmarking, as this method has shown good performance in some of the tests presented by Wang et al. (2015) and Gunes et al. (2006). This method has been implemented in the DACE toolbox for MATLAB (Nielsen et al. 2002), with a second-order polynomial regression and a Gaussian correlation model

(Raben et al. 2012). The detection performance of the PODDEM is quantified by benchmarking the result with the POD-OC method (Wang et al. 2015) and with the AWAMT method introduced by Masullo & Theunissen (2016). As Kriging is solely an interpolation method and AWAMT is purely a detection method, these two methods are coupled when examining estimation and detection.

N.B. the comparisons of POD-OC and AWAMT are computed using algorithms obtained from the authors. For AWAMT the user defined for the coherence threshold, background error and averaging interval are set to the default settings, as outlined in Masullo & Theunissen (2016) (2, 0.1 and 0.3 respectively.)

3.2 Results

3.2.1 Detection ability

Figure 3.3 shows a comparison of the methods outlined above when used to identify the location of the synthetic outliers introduced in the time series. In this work, a correct detection is defined as the detection of a velocity vector belonging to the introduced list of synthetic outliers, while the performance is measured as a percentage of the total number of introduced outliers. A false positive is defined as a velocity vector detected as outlier, but not belonging to the original outlier list; similarly, the performance is measured as a percentage of the total number of introduced synthetic outliers. Only a subset of the estimation methods also have the capability to detect outliers, and thus only PODDEM, POD-OC and the AWAMT methods are benchmarked in this section. As shown in Fig. 3.3 & Fig. 3.4, PODDEM performs similarly to the POD-OC for the detection of correct outliers positions. However PODDEM shows a higher reliability as it has a lower

rate of detection of false positives. Of all the benchmarked algorithms, AWAMT detects the least false positives, but as the size of N_c (the size of the cluster), is increased AWAMT becomes less effective in detection. A noticeable benefit of PODDEM is its constant performance in detection, as only a minor difference in its detection ability is seen between outlier rates and test cases.

3.2.2 Estimation ability

To fully scrutinise the different methods they are all examined twice. Firstly, the methods are examined purely on the basis of their estimation ability i.e where all of locations of the outlier points are known. Secondly, the methods are examined on their coupled estimation and detection ability i.e. where the locations of the outlier points are unknown. The accuracy ($\overline{\epsilon}$) and precision (ϵ_{RMS}) of the methods are presented in Fig. 3.5 & Fig. 3.6. Fig. 3.5 shows that when all of the locations of outliers are known and the methods are used solely for interpolation, POD-OC and Kriging for clusters $N_c \leq 4$, are the most accurate and precise methods. However, with a higher outlier rate ($Q = 15\%$), for clusters i.e. $N_c > 4$, PODDEM is the more accurate and precise. For detection, the accuracy of PODDEM remains constant, regardless of the size of N_c. Fig. 3.6 demonstrates that, even when coupled with the detection functionality the PODDEM's error remains constant. Between the test cases the results for PODDEM are similar, unlike any of the other methods; this suggests that the accuracy of PODDEM could be independent of the test case, and only dependent on the outlier rate Q. A qualitative comparison of the spatial characteristics of the estimation by the different methods is presented in Fig. 3.7. It is clear from the figure that the small scale details of the flow are retained by both POD based methods. The AWAMT method has struggled to

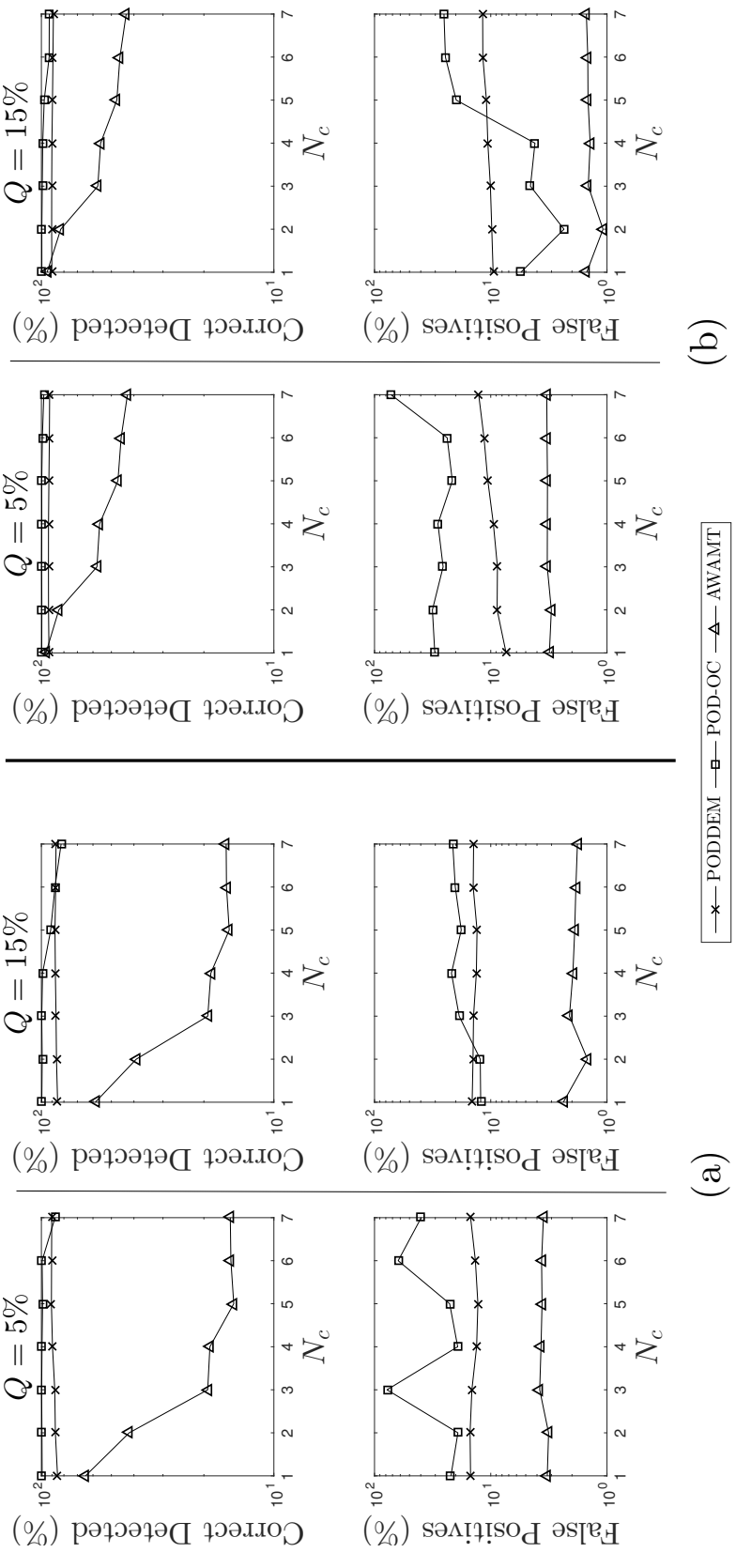

FIGURE 3.3: Assessment of the detection capabilities of the outliers introduced in the channel and isotropic flow time series. The plot shows the performance results for PODDEM and benchmark methods. The top row shows the percentage of correct detected outliers as a function of total number of introduced synthetic outliers, for $Q = 5\%$ and $Q = 15\%$. The bottom row shows the number of false positives, similarly expressed as a function of total number of introduced synthetic outliers. (a) Channel flow (b) isotropic flow

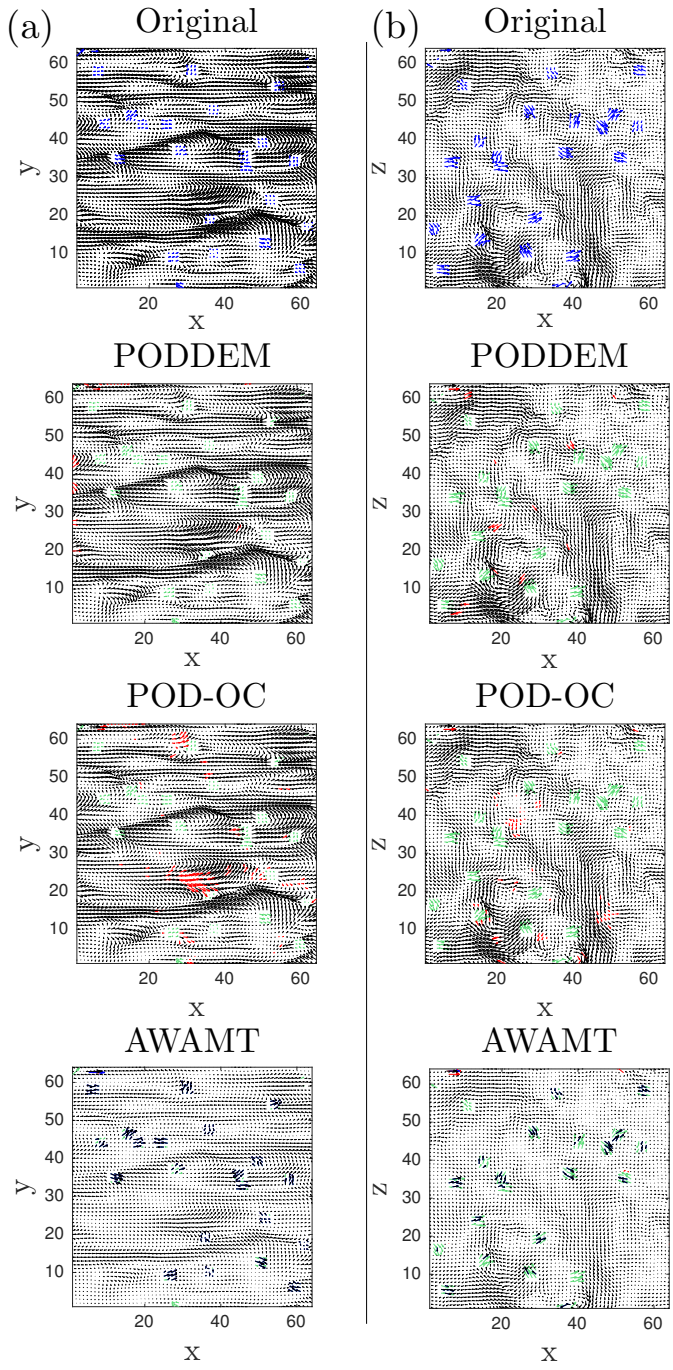

FIGURE 3.4: Example of the detection on a single vector field using the benchmarked detection methods. For this, a $Q = 5\%$, $N_c = 3$ have been used. (a) Channel flow (b) isotropic flow. The black vectors show the original flow, blue show the applied synthetic outliers, green show the correct detections and red show the false positive detections. The 500^{th} vector field in the sequence is shown.

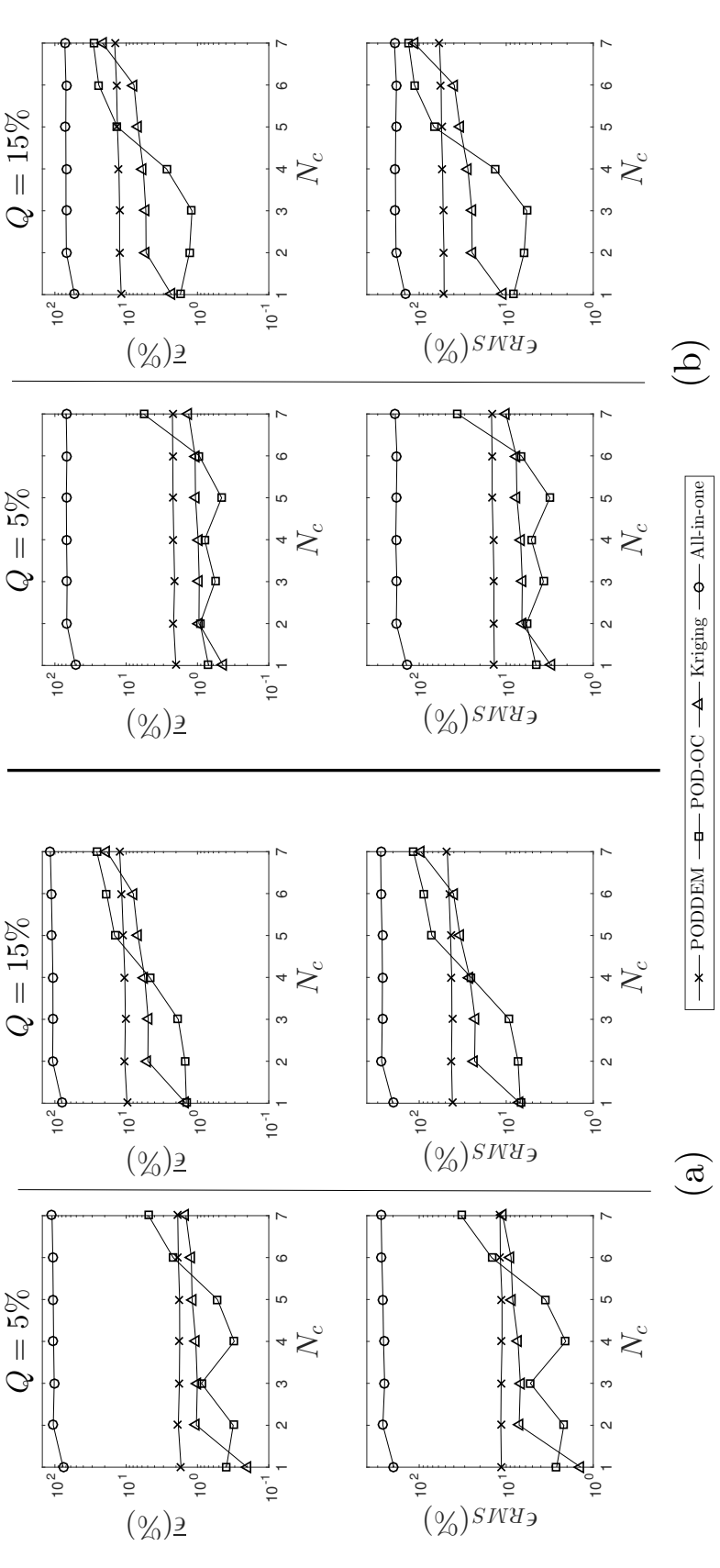

FIGURE 3.5: The plots show a comparison of the performance for the estimation of the correct value of outlier vectors between PODDEM, POD-OC, All-in-one and Kriging methods, where all locations of the outlier points are **known**. The top row shows $\bar{\epsilon}$ (accuracy) and bottom rows show the spatio-temporal ϵ_{RMS} (precision) error. (a) Shows the error obtained with the contaminated channel case. (b) Shows the results for the isotropic case.

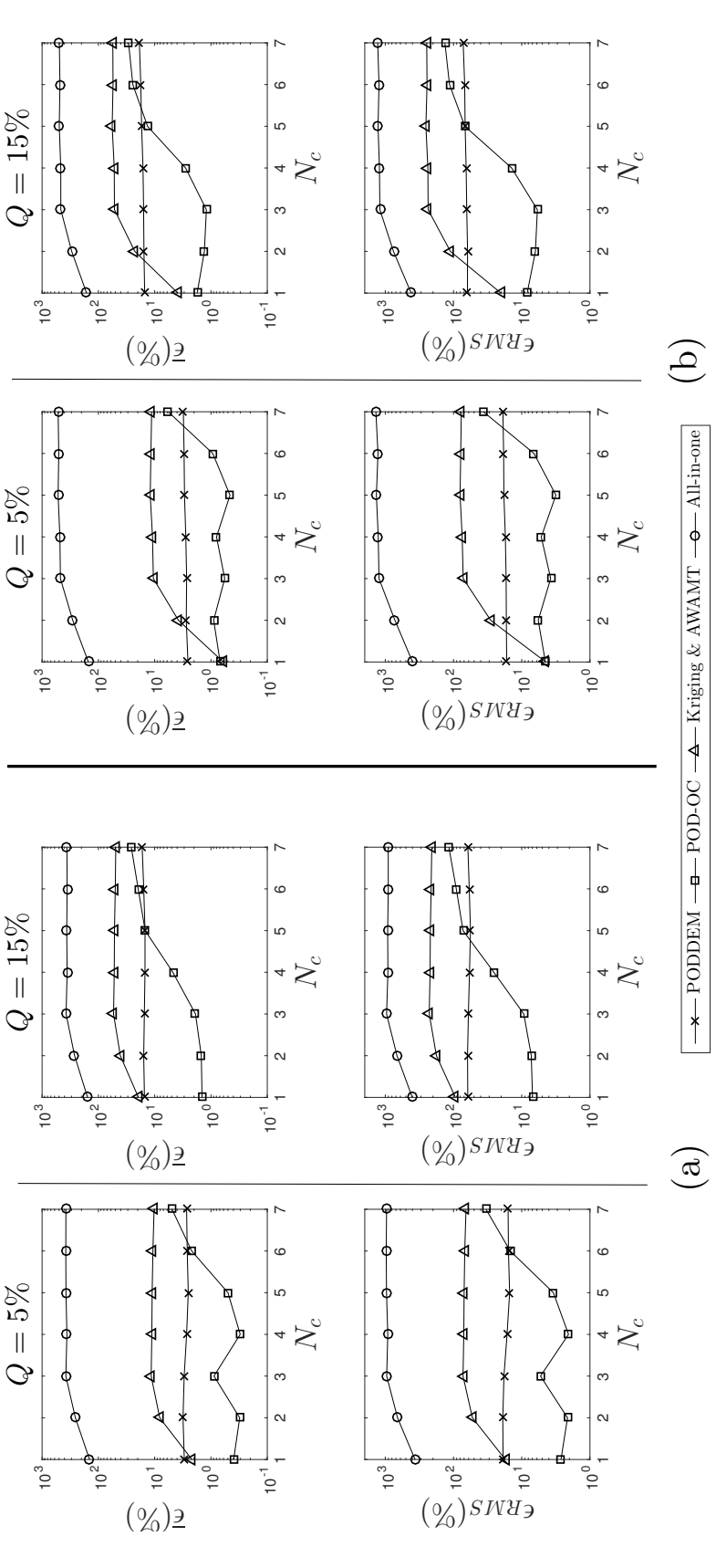

FIGURE 3.6: The plots show a comparison of the performance for the estimation of the correct value of outlier vectors between PODDEM, POD-OC, All-in-one and the coupled AWAMT & Kriging methods, where all locations of the outlier points are **unknown**. The top row shows $\bar{\epsilon}$ (accuracy) and bottom rows show the spatio-temporal ϵ_{RMS} (precision) error. (a) Shows the error obtained with the contaminated channel case. (b) Shows the results for the isotropic case.

detect all of the outlier clusters, resulting in a the vector field which still contains a number of errors. The All-in-one method clearly filters small scale structures thus producing a blurred estimation of the vector field. (N.B. the All-in-one method can be used to interpolate missing values, as shown or to remove influences of outliers making a new estimate of the whole field, as shown in Fig. 3.7.)

An estimated computational efficiency of the calculation under the current implementation is shown in Table 3.1. Of course, a computational performance assessment depends on many factors, such as the programming technique and programming language. So as to exclude such variables, the computations were all undertaken on the same computer, using MATLAB R2015b, and restricted to a single core. The results are normalised with respect to the PODDEM method. It is found that under these conditions, the PODDEM's time efficiency is comparable to that for the All-in-one method and far superior to that for other methods.

	PODDEM	**POD-OC**	**AWAMT & Krig**	**All-in-one**
Channel	1.0	55	4073.6	1.1
Isotropic	1.0	68	2905.8	0.8

TABLE 3.1: Comparison of computing time between PODDEM and benchmark algorithms. The values are normalised with respect to the PODDEM calculation time.

The SVD which is at the core of the PODDEM and POD-OC methods is memory intensive. As illustrated by the test cases where only between 6 - 9 integral time scales are used, the dataset could be temporally partitioned (assuming it is statically converged) if memory is limited. PODDEM offers a substantial time benefit compared with POD-OC, which requires a minimum of two SVDs while PODDEM only ever requires one.

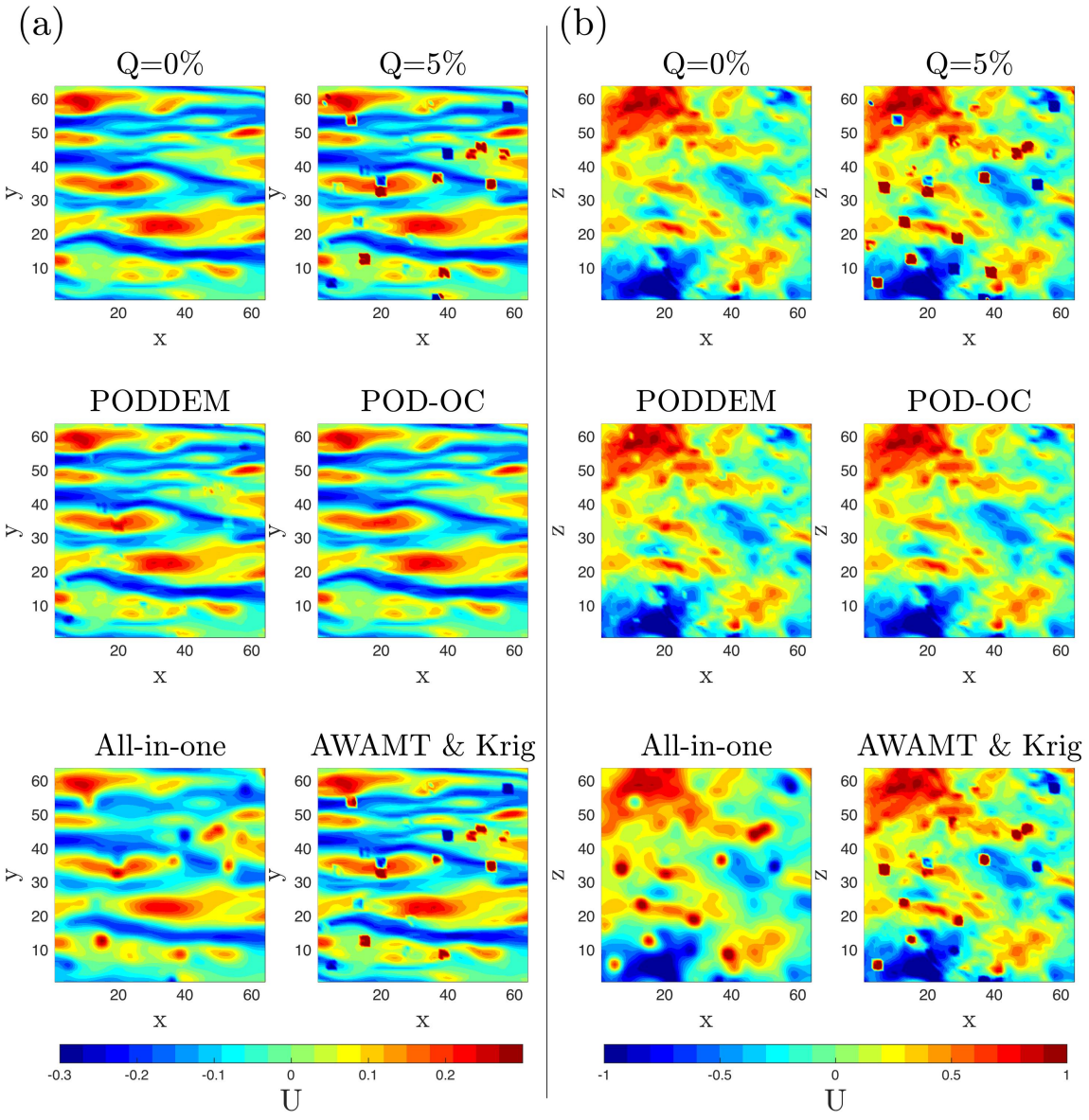

FIGURE 3.7: Example of the estimated instantaneous longitudinal velocity component after the application of the benchmarked estimation methods. For this, a $Q = 5\%$, $N_c = 3$ have been used. (a) Channel flow (b) isotropic flow. The original snapshot, with no outliers, i.e. $Q = 0\%$, and with $Q = 5\%$ are shown in the top row for reference, where U is the streamwise component. The 500^{th} vector field in the sequence is shown.

3.2.3 Detection and estimation on a single vector field

In this section the detection and estimation capabilities of the proposed algorithm are tested not for a sequence of vector fields, but instead for a single contaminated field. This case has been selected to demonstrate that PODDEM can still be used if time resolute data is not available. PODDEM is benchmarked in a manner analogous to the benchmark performed by Wang et al. (2015). A single vector field (500^{th}) is sub-divided into multiple sub-fields, which are used to build an ensemble of observations. Wang et al. (2015) showed that the size of the number of sub-fields is critical: a larger size of the sub-fields will offer more spatial information, but will reduce the number of ensemble components. This means the total number of modes involved in the decomposition of the ensemble will be reduced. According to Wang et al. (2015), the ensemble construction is more effective for filtering when the ratio between the sub-fields size, $(n_b \times m_b)$, and the size of the original snapshot $(N \times M)$, R_B, is between 0.2 and 0.5. Wang et al. (2015) also recommends creating the ensemble for overlapping sub-fields i.e. a one vector element shift along both x and y, thereby increasing number of fields; accordingly, a sub-field of size $n_b \times m_b = 16 \times 16$ was chosen.

The results of the detection assessment are shown in Fig. 3.8. Much as in the results in previous section, PODDEM shows a better detection performance than POD-OC in terms of the percentage of correct outliers identified. Whilst the AWAMT method does not detect many false positives, its detection ability decreases as the cluster size increases again. Between the POD-based methods, a difference can be observed when the percentages of false positives are compared. The higher reliability of PODDEM in this regard is evident from the results for both channel and isotropic case flow.

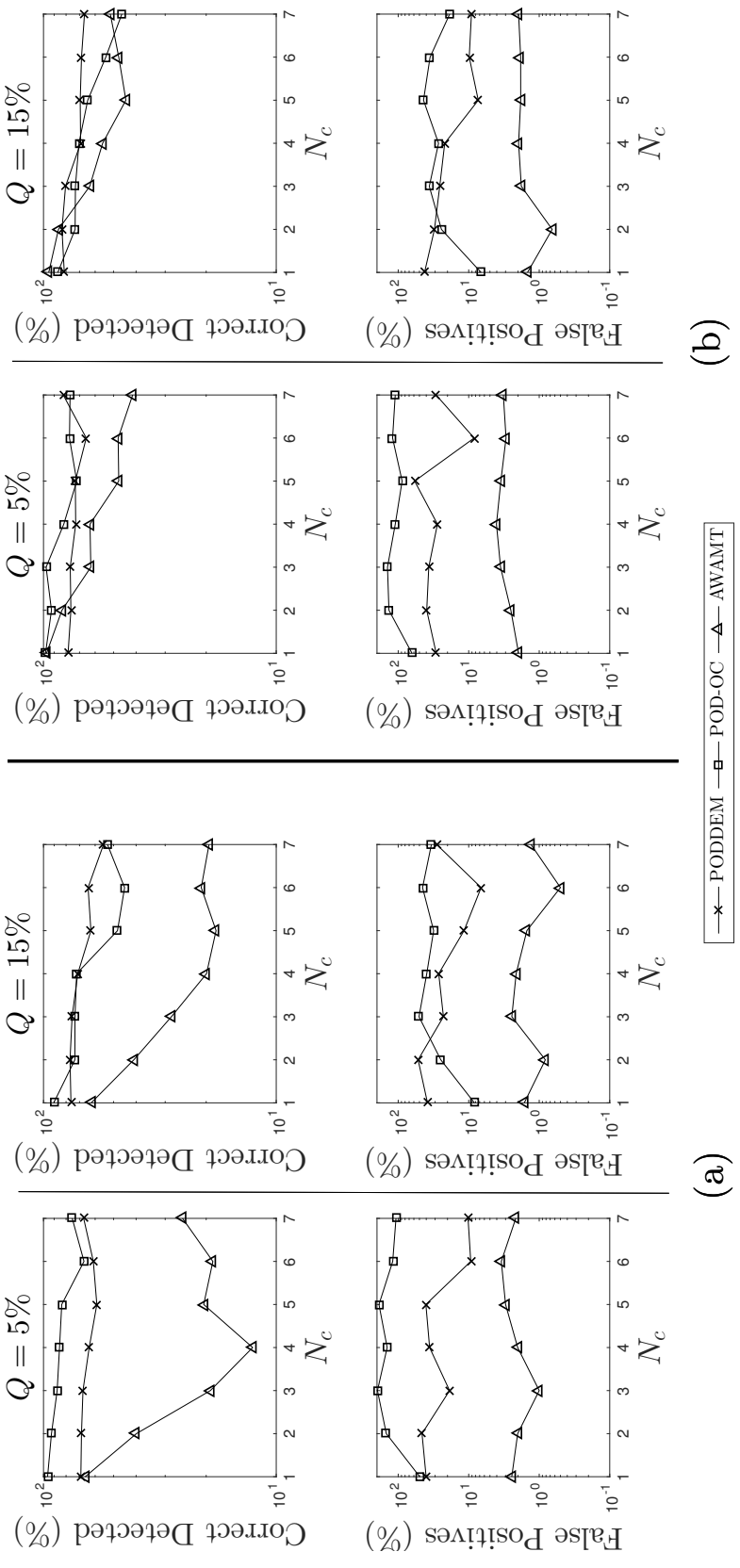

FIGURE 3.8: Performance comparison between PODDEM, POD-OC and AWAMT for the detection of outliers in case of a single contaminated vector field (500^{th}). The top row shows the correct outliers detected. The bottom row shows the percentage of false outliers detected. (a) Results for isotropic case. The snapshot has been transformed in an ensemble by using sub-fields of size $n_b \times m_b = 16 \times 16$

The errors in estimating the detected outliers for the single contaminated vector field are shown in Fig. 3.9. It is observed from the figure that PODDEM offers the most robust, accurate and precise estimation of the vector field. In particular, the improvement in the precision statistics when using PODDEM are clear. A qualitative comparison of the spatial characteristics is presented in Fig. 3.10. The results of the estimation highlight some of the limitations of the POD based methods for the estimation of a single frame. However, the quantitative and qualitative results show that PODDEM improves estimates compared to those obtained using POD-OC, AWAMT & Kriging and the All-in-one method.

3.2.4 PIV data

To supplement the quantitative analysis, the same methods are applied to real PIV data containing real outliers. As the locations of outlier vectors are not known, a formal analysis is not possible. As shown in Fig. 3.11, qualitatively speaking all of the methods perform well apart from the All-in-one method, which again removes/blurs the smaller spatial scale. Unfortunately, the PIV data contained no large clusters of outliers which may have highlighted PODDEM's ability. From Fig 3.11 it is clear that the AWAMT method and Kriging is favourable. However, PODDEM detects all of the outlier points, especially those which could have a statistical impact, which POD-OC does not. If the data had contained large groups of outlier points, as demonstrated earlier, the results for AWAMT method and Kriging may not have been as favourable.

To further qualitatively demonstrate the detection and estimation capabilities of the PODDEM on a single field, it is applied to the real PIV data. In Fig. 3.12 vector field (500^{th}) of the real PIV data is selected and the PODDEM is compared

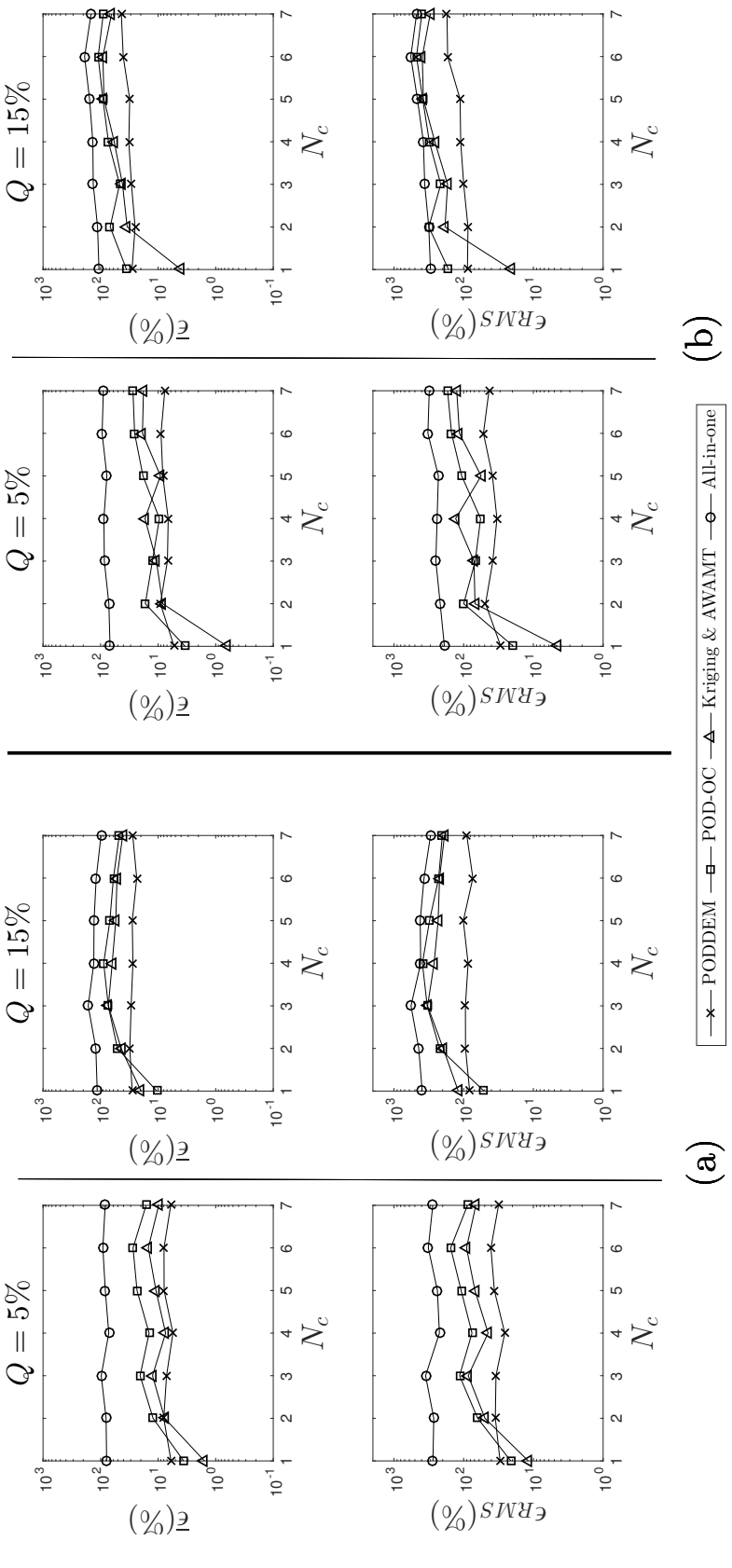

FIGURE 3.9: $\bar{\epsilon}$ (accuracy) and ϵ_{RMS} (precision) of PODDEM and POD-OC vector estimations for a single contaminated vector field (500^{th}). The top row shows $\bar{\epsilon}$ (accuracy) and bottom rows show the spatio-temporal ϵ_{RMS} (precision) error. (a) Shows the error obtained with the contaminated channel case (b) shows the results for the isotropic case. The snapshot has been transformed in an ensemble by using sub-fields of size $n_b \times m_b = 16 \times 16$

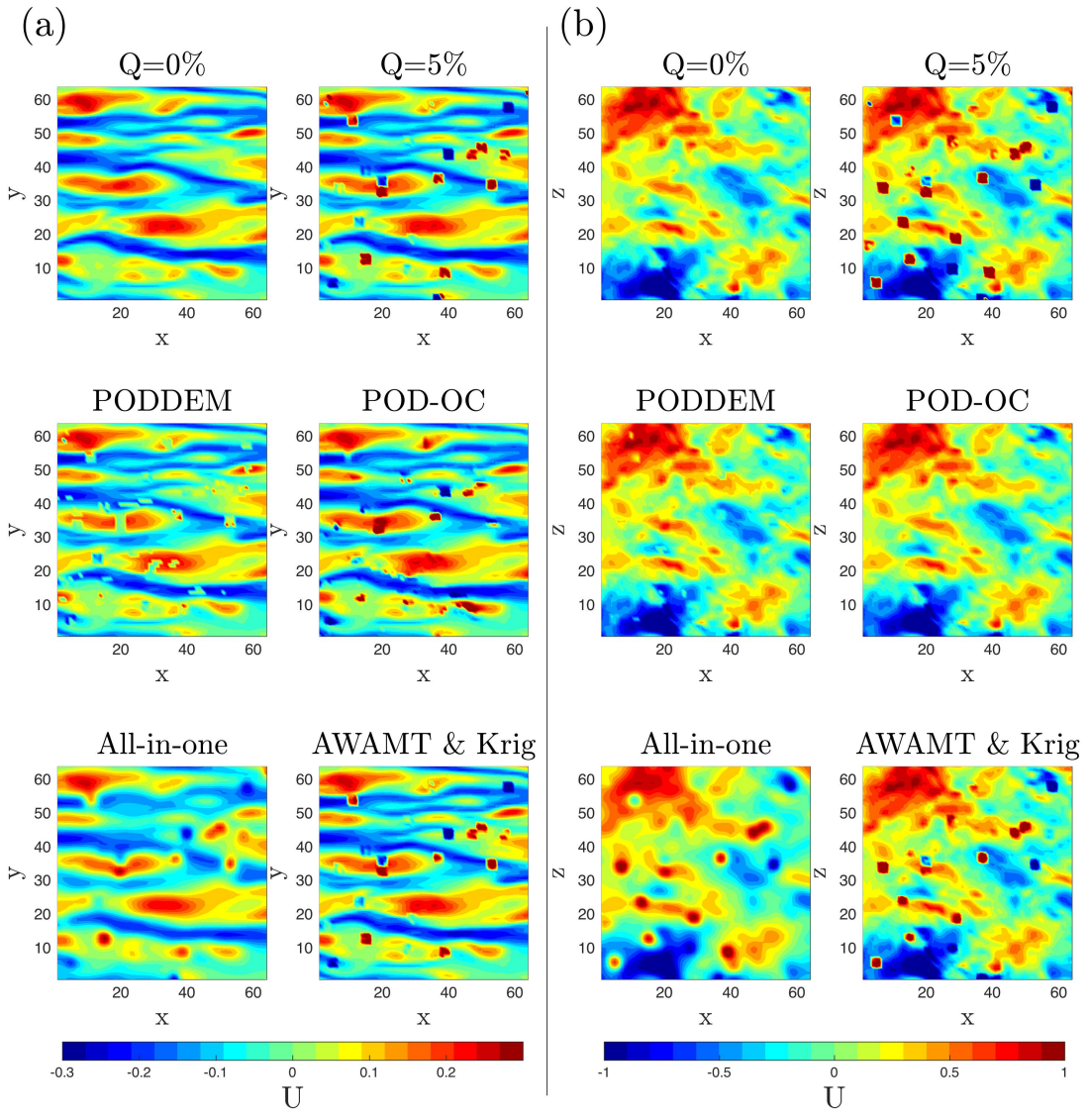

FIGURE 3.10: Estimation of the vector field associated to a single contaminated snapshot. The top rows show the original frame, $Q = 0\%$ and the contaminated frames with $Q = 5\%$ of outliers and $N_c = 3$. The bottom row shows the estimation obtained using the PODDEM and POD-OC. (a) Results for channel flow. (b) Results for the isotropic flow. The vector field has been transformed in an ensemble by using sub-fields of size $n_b \times m_b = 16 \times 16$, where U is the streamwise component. The 500^{th} vector field in the sequence is shown.

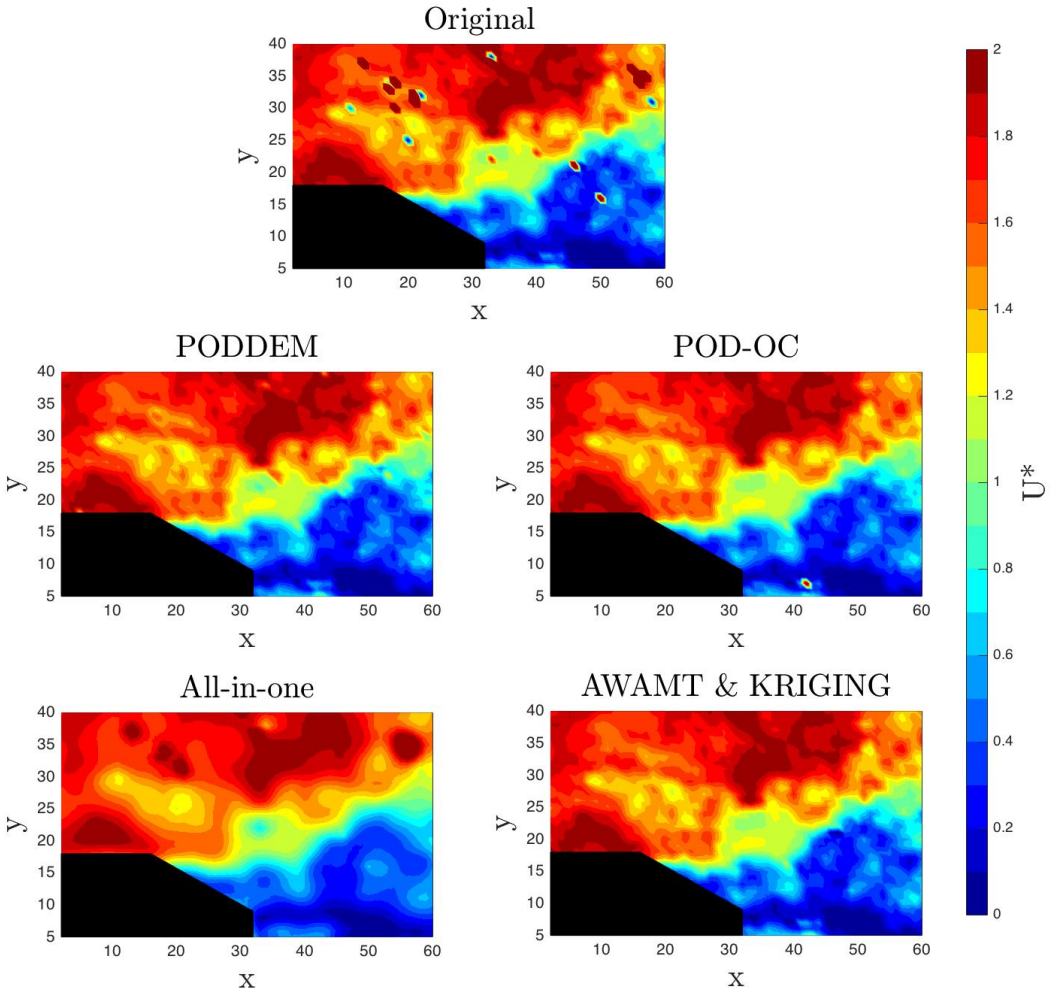

FIGURE 3.11: An example of the application of PODDEM, POD-OC, All-in-one and AWAMT & Kriging to real PIV data to a time series of data. Where U^* is defined at the velocity magnitude. As previous the 500^{th} vector field is presented.

with POD-OC, where $n_b \times m_b = 16 \times 16$. From Fig. 3.12 it is clear that the PODDEM out performs the POD-OC in both detection and estimation.

3.3 Discussions

The results show that there are clear advantages to using spatio-temporal information for the detection and estimation of outliers. As demonstrated by the present study, a POD-based technique can be approached using either a modification of the spatial modes (POD-OC) or a modification of the temporal coefficients (PODDEM). Figures. 3.3 & 3.4 in section 3 further demonstrates that there are clear benefits to modifying the temporal coefficients (PODDEM) for detection, especially in the case of large clusters of outliers. Figures 3.5, 3.6 & 3.7, show the estimation ability of PODDEM may not always be the optimal choice for smaller clusters of outliers, a user could opt to use a hybrid of a Kriging based method for small scale estimations and PODDEM for large scale estimations. This may be especially beneficial in the case of single vector fields. Furthermore, if time is not a limiting factor as user may opt to use the Adaptive Gappy-POD formulation Raben et al. (2012), however this method is extremely computationally expensive and impractical for large datasets.

3.3.1 POD-OC modifications

From the authors' investigations, it is found that the 'robust parameter', $a = 3$, which is proposed by Wang et al. (2015) for the POD-OC algorithm is not optimal, and that changes to a can improve the performance of POD-OC. A sensitivity analysis of a is shown in Fig. 3.13. As PODDEM also requires a user defined

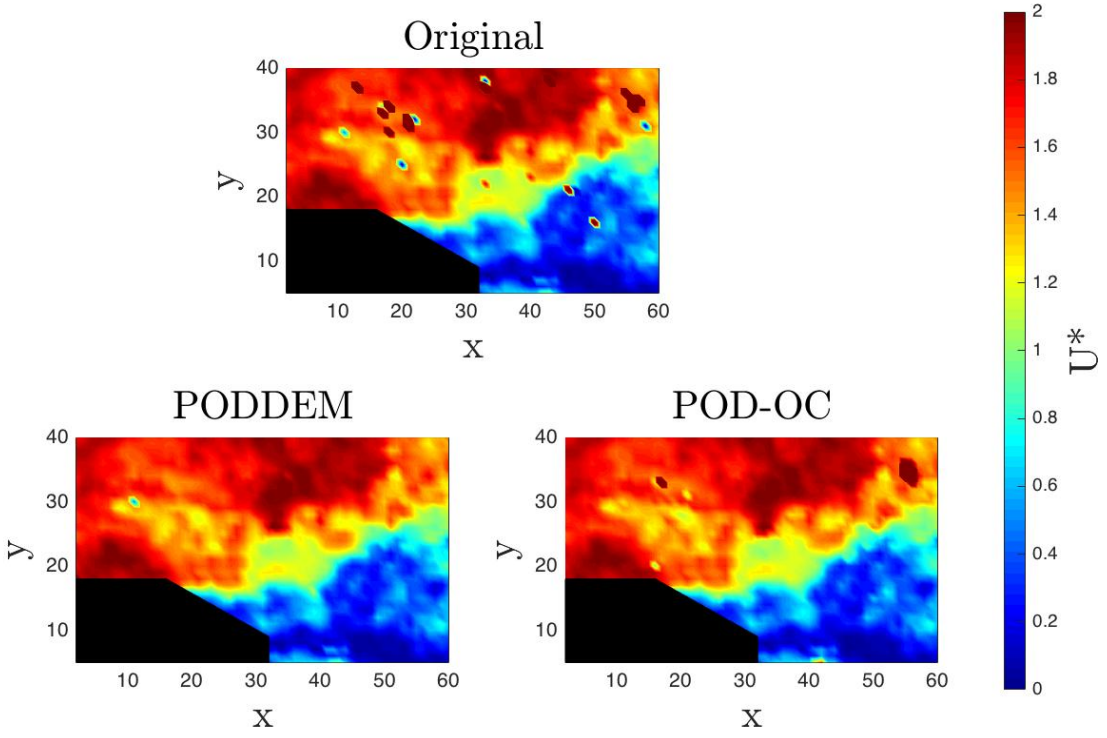

FIGURE 3.12: An example of the application of PODDEM, POD-OC, single frame of real PIV data (vector field 500^{th}). Where U^* is defined at the velocity magnitude. The vector field has been transformed in an ensemble by using sub-fields of size $n_b \times m_b = 16 \times 16$.

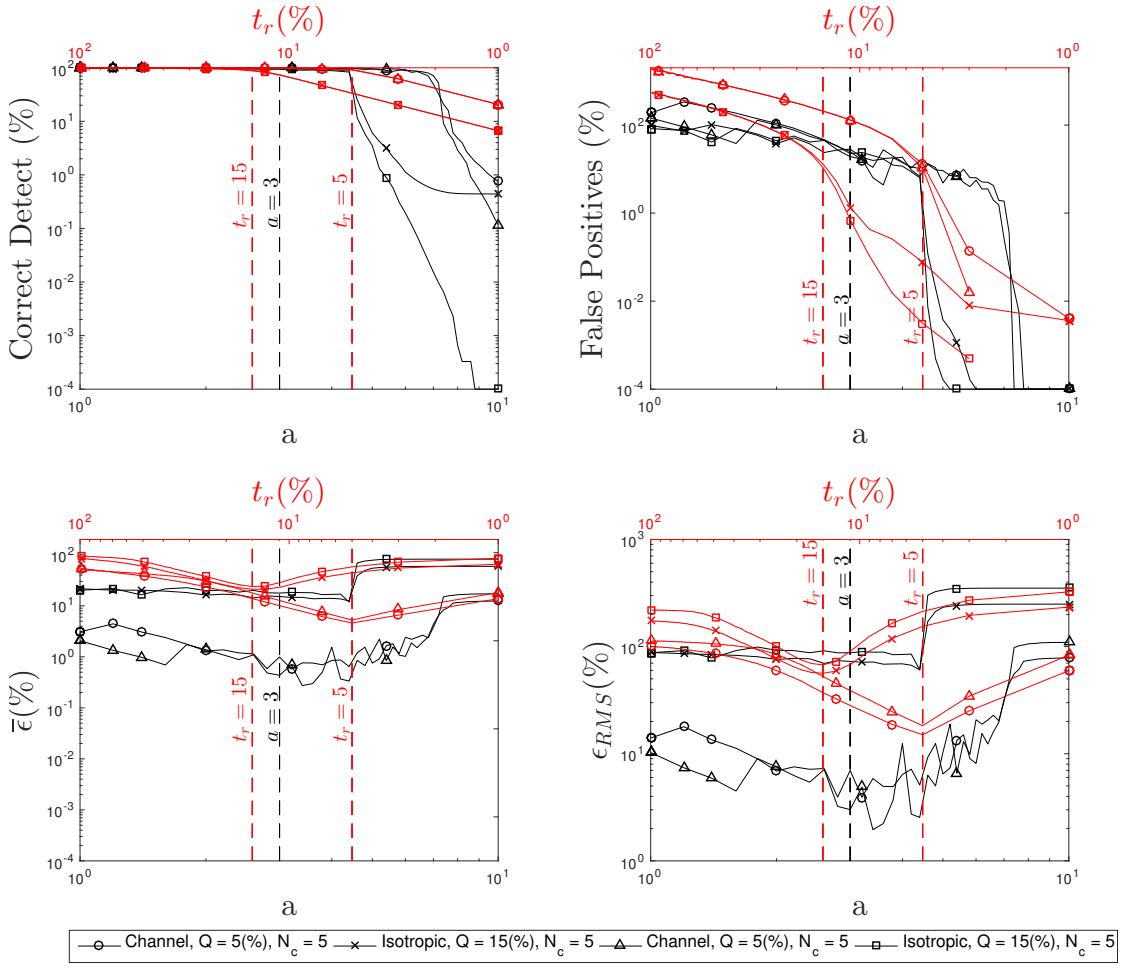

FIGURE 3.13: Sensitivity analysis: Varying the 'robust parameter', a, in the POD-OC algorithm (Black), and the user defined threshold, t_r, in PODDEM (Red). Top panels show the percentage of correction detections and false positives. Bottom panels show $\overline{\epsilon}$ (accuracy) and ϵ_{RMS} (precision).

percentage, t_r, which was previously introduced as dependent on the outlier rate, Q, a sensitivity analysis of t_r is also shown on the same figure, but on different axes. For the sensitivity analysis, a subset of four test cases are selected, two from each dataset (channel flow and isotropic turbulence), using two outlier rates $Q = 5\%$ and $Q = 15\%$, with an $N_c = 5$. Fig. 3.13 demonstrated that POD-OC has an optimal performance for $a \approx 4.5$. If this parameter is used, the correct rate of detection is increased, and rate of false detection minimised. The dependence of t_r with Q is also clear in the results. The optimum value of t_r in PODDEM is defined only by Q, which is a parameter that can be estimated based on a visual inspection of the PIV snapshots. However a user may adopt a value of $Q = 5\%$ as suggested by Westerweel & Scarano (2005*b*).

3.3.2 Further advancements to the PODDEM algorithm

The proposed PODDEM algorithm is based on the premise of 'smoothing' outliers within the temporal coefficients. This is ideal when every vector field contains an outlier; realistically however, not all vector fields will contain outliers. As shown in Fig. 3.14 when only 100 random frames contain outliers (i.e. 10% $N_c = 3$ & $Q = 5\%$), at the temporal locations relating to the vector fields containing outliers, spikes are perturbed in to the temporal coefficients. By imposing a spike detection algorithm, instead of a moving average, such as the 'Nikora-Goring method', typically used to remove spikes from acoustic doppler velocimetry data, Goring & Nikora (2002), the spikes can be removed without effecting other vector fields devoid of outliers. This is particularly beneficial where the temporal resolution of the dataset it low.

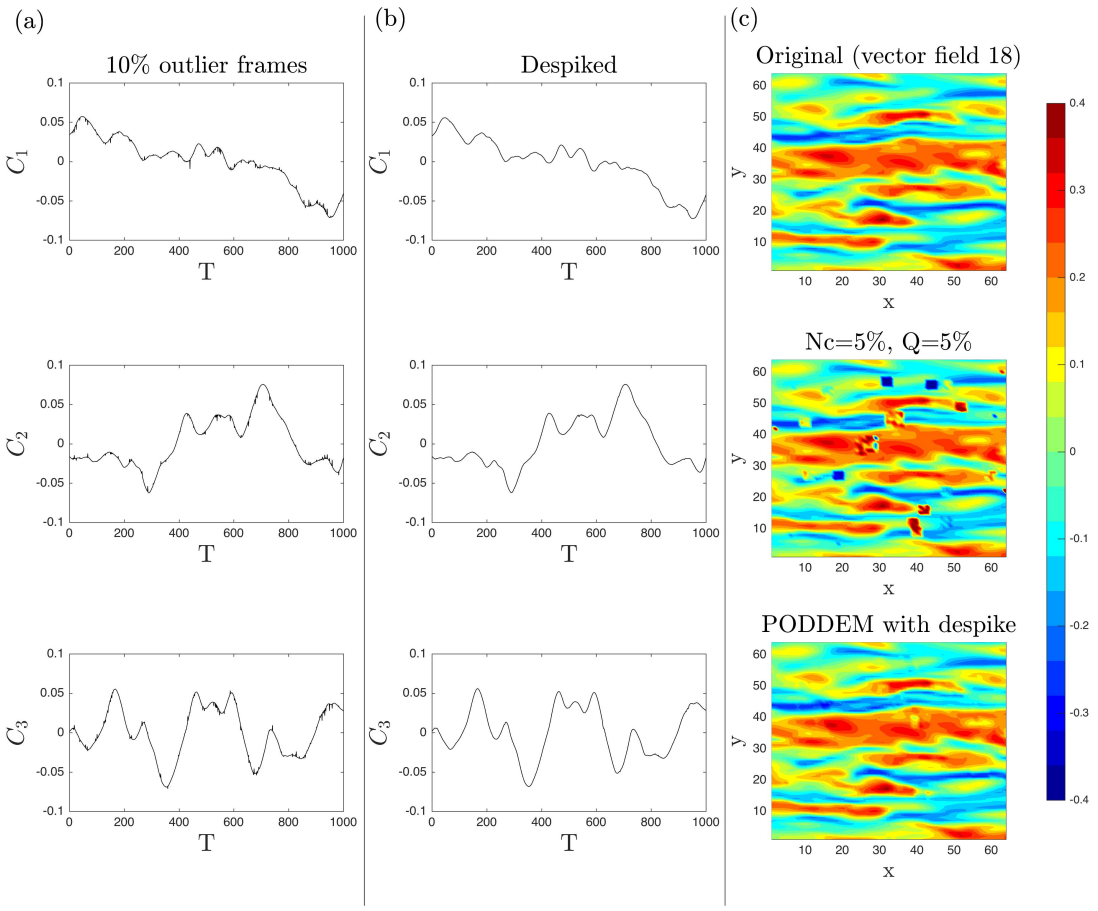

FIGURE 3.14: An example of outliers, $N_c = 3$ & $Q = 5\%$, applied to 100 random frames within the time series (vector field 18 shown). It is seen their locations perturb into the temporal coefficients.

3.4 Chapter conclusions

This chapter proposes a novel, rapid and non-iterative POD method for the detection and estimation of outliers (PODDEM) based on modifications of the temporal coefficients. By introducing synthetic outliers to time series extracted from the John Hopkins Turbulence Database, and to real PIV data, the detection and estimation abilities of PODDEM are benchmarked against state-of-the-art spatial/spatio-temporal methods, including POD-OC. From the results it is observed that there are clear advantages from using the POD (spatio-temporal) methods for the detection and estimation of outliers. Whilst the PODDEM is not always the most the accurate the robustness and time benefits clearly outperform other state-of-the-art methods. A sensitivity analysis reveals that a modification of the temporal coefficients is beneficial in robustness for the detection of outliers compared with modifications of spatial modes, as in POD-OC. Furthermore, for cases which are not time resolved, PODDEM can be applied to a single vector field. Compared with state-of-the-art spatial estimation and detection methods, PODDEM is able to improve the detection of outliers for single frames without decreasing the estimation accuracy.

Chapter 4

Implications of the selection of a particular modal decomposition technique for the analysis of shallow flows

This chapter deals with the capabilities of two synoptic modal decomposition techniques for the identification of the spatial patterns and temporal dynamics of coherent structures in shallow flows. Using two different experimental datasets it is shown that due to the linear behaviour of large-scale, quasi-two-dimensional flow structures, there is almost no differences in the identification of dominant modes between the results obtained from a traditional Proper Orthogonal Decomposition and the more recently developed Dynamic Mode Decomposition. However, it is also shown that non-linear dynamics can arise in the transition of these structures to a quasi-two-dimensional behaviour, which can result in the Proper Orthogonal Decomposition identifying structures composed of multi-frequencies, a sign of a

convoluted dynamics. Thus Dynamic Mode Decomposition is recommended instead for the analysis of such phenomena. In addition, this chapter introduces a simple ranking methodology for the use of the Dynamic Mode Decomposition technique in shallow flows, which is based on the results of the Proper Orthogonal Decomposition.

4.1 Introduction

The aim of this chapter is to not only demonstrate the potential utility of DMD in hydraulics research, but also to show how it can be complemented, and the interpretation of its results enhanced, through the use of information from POD. Overviews of these two techniques are provided in Chapter 2. Results where DMD and POD largely return the same behaviours are then presented, before considering a case in greater detail where more complex flow dynamics requires the use of the two techniques in parallel.

From Eq. 2.7, it is clear that each of the modes obtained by DMD relates to a unique peak frequency. If the Fourier spectrum of the POD coefficients is used to identify the frequency of dominant but intertwined structures, these frequencies can be used to identify their spatial structure from the DMD results. There is a main restriction for this methodology. The technique can be applied only for the identification of POD modes in shallow flows or in cases where a flow structure clearly governs the dynamics. In these flows, peak frequencies are expected to be clearly identified from the Fourier spectrum of the temporal POD coefficients. These conditions do not hold, for instance, in three-dimensional turbulent flows, where the contribution of low order modes can be of a similar magnitude to the contribution of higher order ones. Thus, any frequency extracted from the Fourier

spectrum might be misleading due to the lack of capabilities of POD to separate non-linear interactions of structures with similar contributions to the variance of the signal. It is because of this that the link between POD and DMD introduced here, is only presented in the context of shallow flows.

4.2 Flow visualisations of a shallow cylinder wake

A first experimental dataset was selected to showcase hydrodynamic conditions where the DMD does not improve the identification of Q2CS in the low order modes, obtained by POD. The dataset was obtained from the experimental work of Brevis & García-Villalba (2011), in which the POD of a flow visualisation was used to identify dominant frequencies in the wake of a cylinder in a shallow flow. All experimental details can be found in the work of Brevis & García-Villalba (2011). Fig. 4.1 shows the results obtained from the POD analysis. In this case modes $\mathbf{\Phi}_{1\&2}$ were paired indicating a periodic shedding behaviour with a different phase in these two modes. Fig. 4.1 only shows $\mathbf{\Phi}_1$ as reference. The modes reveal the advection of patches of dye transported by vortical structures. Modes $\mathbf{\Phi}_{3\&4}$ show a different structure, although also paired, which according to Brevis & García-Villalba (2011), corresponds to the spanwise alternated motion of the vortex behind the cylinder. The evolution of the temporal coefficients is clearly sinusoidal, thus a peak at f={0.2Hz & 0.4Hz} can be observed in the Fourier spectra for modes $\mathbf{\Phi}_{1\&2}$ and $\mathbf{\Phi}_{3\&4}$. As shown by Brevis & García-Villalba (2011) these two frequencies also relate to two peaks found in the Fourier Spectrum of Laser Doppler Anemometer (LDA) measurements of the same case. Due to the size of the region analysed, it is expected that the Q2CS will govern most for the spatial flow features. In addition S_n=0.06, thus it is expected to see a highly

linear dynamic of the dominant modes. This can be seen in the results of the DMD analysis shown in Fig. 4.2, where the spatial structure of the modes is very similar to that obtained by the POD. In both cases the coefficients show a sinusoidal shape, although the most noticeable difference is the sharper peak in the Fourier spectra in Fig. 4.2, highlighting the better localisation of the DMD method.

4.3 Shallow flow obstructed by a groyne

A shallow turbulent flow obstructed by a single groyne is a common occurrence in fluvial shallow flow hydraulics. The selected case corresponds to a flow topology similar to the one described by Talstra (2011). The flow that developed downstream of the obstacle is characterised by the formation of a shear layer bounding a low velocity recirculation region formed by a primary clockwise gyre, located in the downstream part of the recirculation zone, and an anti-clockwise secondary gyre, of smaller size, located immediately downstream the obstacle. The structures populating the shear layer in the near field, are expected to be generated by both vortex shedding from the tip of the obstacle, and by the strong velocity gradient produced between the main channel and the secondary gyre interface. From a general observation of the derived vorticity fields sequence, it is expected that the vortices associated with the velocity gradient are of a larger size as the mechanism of generation seems to be more energetic than vortex shedding. Even though $S_n \leq 0.6$, the region analysed here is the near field, where vortices are not expected to behave as a Q2CS, but are in a transitional stage, still governed by quasi two-dimensional features, but also influenced by three dimensional ones. It is in this region that one compares the POD and DMD performance and to introduce their integration.

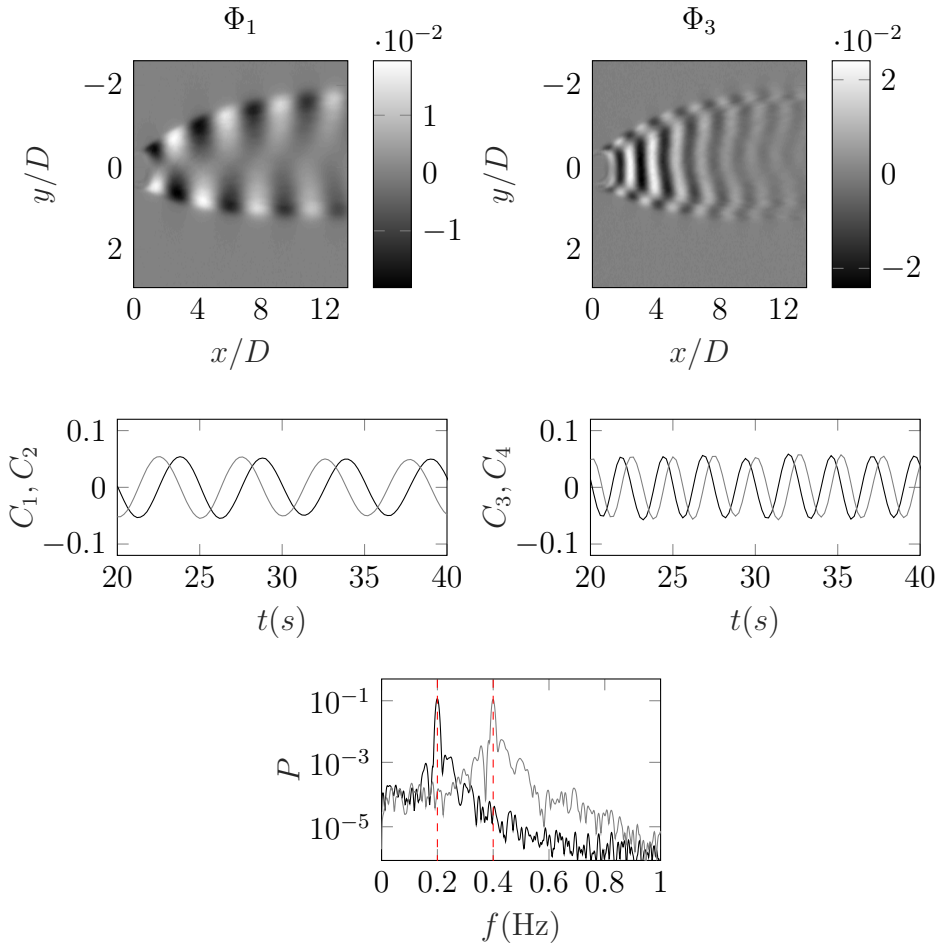

FIGURE 4.1: POD results of flow visualisations of a shallow cylinder wake. The top row shows the spatial modes $\mathbf{\Phi}_1$ & $\mathbf{\Phi}_3$. The central row shows the temporal coefficients $\mathbf{C}_1$ & $\mathbf{C}_3$, where the grey line denotes the mode which forms the conjugate pair. The bottom row shows Fourier Power Spectrum of the temporal coefficients $\mathbf{C}_1$ & $\mathbf{C}_3$ (grey). The red dashed lines highlight the frequencies extracted using the DMD.

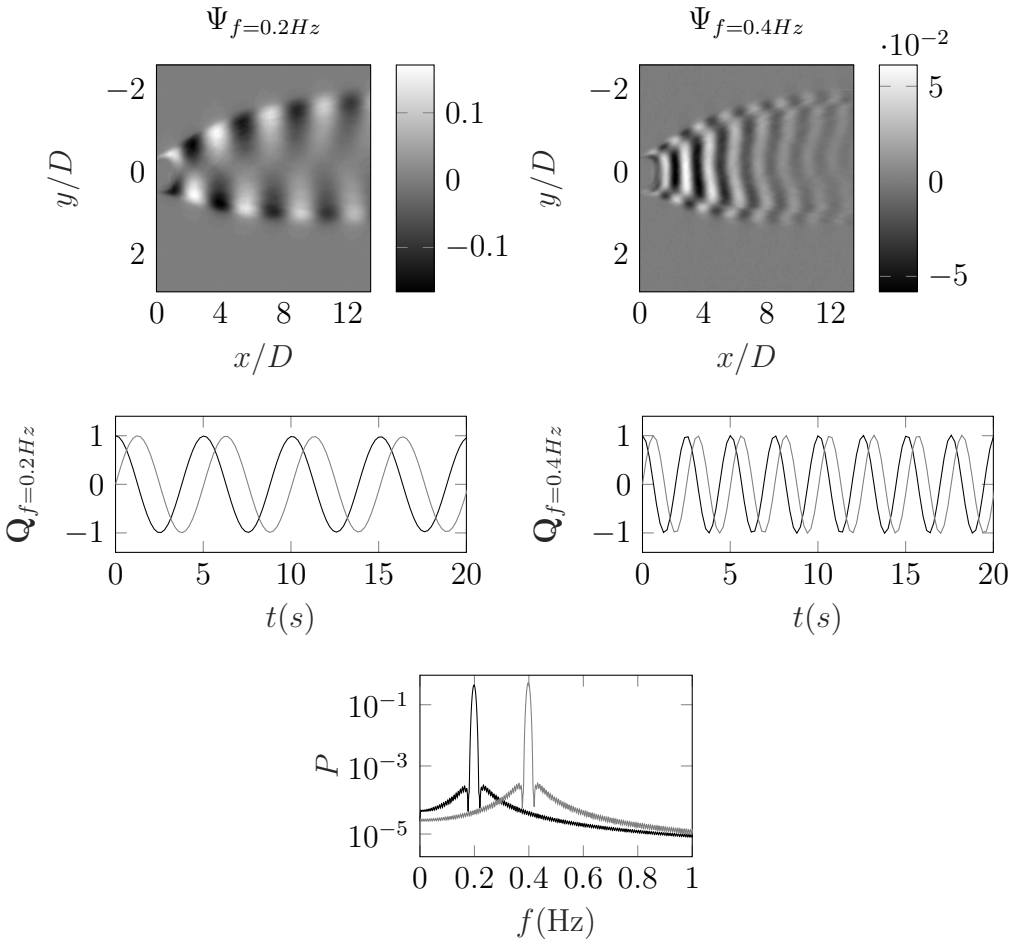

FIGURE 4.2: DMD results of flow visualisations of a shallow cylinder wake. The top row shows the spatial modes $\mathbf{\Psi}_{f=0.2Hz}$ & $\mathbf{\Psi}_{f=0.4Hz}$. The central row shows the real part of the temporal coefficients $\mathbf{Q}_{f=0.2Hz}$ & $\mathbf{Q}_{f=0.4Hz}$, where the dashed lines denotes the imaginary part. The bottom row shows the Fourier spectrum of the temporal coefficients $\mathbf{Q}_{f=0.2Hz}$ & $\mathbf{Q}_{f=0.4Hz}$ (grey).

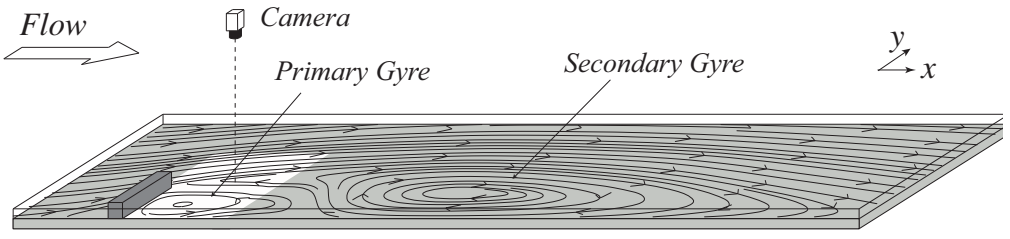

FIGURE 4.3: Illustration of the experimental setup of the single groyne. Measurement section highlighted in white. (Not to scale.)

The experiments were carried out in a tilting shallow flume of 18 m $\times$ 1.82 m located at the Institute for Hydromechanics, Karlsruhe Institute of Technology, Germany. A single rectangular obstacle of length D= 0.25 m and cross section 0.05 $\times$ 0.05 m was placed perpendicular to the main flow direction, at the side-wall of the flume, and at 12 m downstream from the channel entrance. The flow rate Q_0 was set to 0.0135 $\mathrm{m^3 s^{-1}}$, and the flume slope was inclined to 0.001 m/m resulting in a water depth H=0.04 m (see Fig. 4.3). The Reynolds number was, Re $=\mathrm{U_0 H}/\nu$=29680. These conditions gave a low Froude number, $Fr = U_0/\sqrt{gH} = 0.29$, where g is the acceleration of gravity, which ensured minimal surface disturbances (Uijttewaal 2005). Using the method of Zigrang & Sylvester (1982), the friction factor was estimated to be 0.03, thus $S_c = 0.18$ the dynamic of the Q2CS was quantified by means of Large Scale Particle Image Velocimetry (LSPIV) measurement. The PIV system consisted of a camera with a 1200$\times$1200 pixel CCD-sensor and 12 bit resolution. The flow was seeded with floating 2.5 mm particles using a pneumatic particle dispenser. It has been previously shown that the use of these tracer particles is effective in capturing the large scale turbulent motions (Weitbrecht et al. 2002). The camera was mounted directly above the water surface at a height of 1.5 m and was set to capture an area of 0.5 $\times$ 0.45 m downstream of the obstacle. A total of 700 Snapshots were recorded with an acquisition frequency of 7.5 Hz, relating to a spatial average of 15 integral time scales, to ensure the statistics were fully converged. The image sequence was analysed using the PIV package for Linux GPIV (van der Graaf 2010), using multi-pass and image deformation techniques (Scarano 2002), and the raw PIV results were filtered using the PODDEM algorithm (Higham et al. 2016).

Both the POD and DMD calculations were undertaken on all 700 snapshots. The POD was calculated over the snapshots of the fluctuating velocity field, while

the DMD was performed over the instantaneous velocity snapshots, for reasons discussed in Chapter 2.

In Fig. 4.5 the first two POD modes, $\mathbf{\Phi}_{1\&2}$, of the vorticity field are presented. These two modes have similar energy, contributing to ∼35% of the total variance. As shown by Rempfer & Fasel (1994) and Brevis & García-Villalba (2011), two modes of similar energy can show analogous, but shifted, spatial and temporal features. In this particular case, these shifted features appear to be related, as expected, to the advection of vortices resulting from a Kelvin-Helmholtz instability. Also in Fig. 4.5 the temporal coefficients, $\mathbf{C}_{1\&2}$, of the first two modes are presented. The evolution of the coefficients appears to correspond to the presence of multiple dynamical processes. This is further revealed by the Fourier spectrum of $\mathbf{C}_{1\&2}$, which shows the presence of a broad band of frequencies but with clear peaks, at different energy levels, and frequencies of f={0.21Hz, 0.32Hz & 0.39Hz}. After performing the DMD analysis on the data, the modes associated to these peak frequencies were identified. The properties of these modes are shown in Fig. 4.6, where the upper panels show the real part of each spatial mode, and the real (solid line) and imaginary (grey line) temporal coefficients are shown in the panels underneath. The bottom panel highlights how sharply the identified frequencies are expressed in the DMD modes. In Fig. 4.6 the first spatial DMD mode, $\mathbf{\Psi}_{f=0.21Hz}$, resembles the structures seen in the two first POD modes, and as shown in subsequent work, not presented here, that this is related to a flapping motion of the shear layer. The second mode $\mathbf{\Psi}_{f=0.32Hz}$ reveals the presence of an advecting motion along the shear layer. Finally the third mode $\mathbf{\Psi}_{f=0.39Hz}$ shows structures of smaller size but with about twice the frequency of the first mode which are shed from the tip of the obstacle. These mechanisms are summarised in Fig. 4.4. This example highlights the advantages of the presented approach

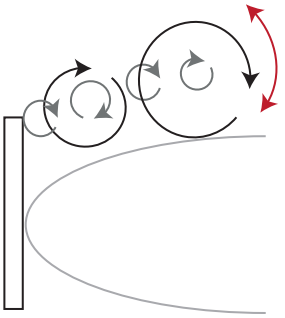

FIGURE 4.4: Schematic of groyne mechanism. Grey circles denote structures shed from the tip of the obstacle (f=0.39Hz), black circles denote the advection of structures along the shear layer (f=0.32Hz) and the red arrow denotes the flapping motion (f=0.21Hz).

of combining the DMD algorithm with a POD based search criterion. Because turbulent shear layer formulation and eddy shedding are typically complex and nonlinear, a mixing of frequencies is clear in the POD temporal coefficients. Using DMD, one can seek these frequencies and discern the flow processes that drive this dynamic behaviour.

4.4 Chapter conclusions

In this chapter a methodology has been introduced for enhancing understanding of fluvial and hydraulic processes in shallow flows using two modal decomposition methods. The physical basis for the approach derives from the fact that the POD undertakes a decomposition that is proportional to the variance in the data and, consequently, is related to energy or enstrophy in the measurements. However, for complex flows, POD mixes together multiple frequencies. The Fourier spectrum of a POD mode provides the information to search through the DMD to find the relevant frequencies. The spatial DMD modes corresponding to these frequencies can then be used to elucidate the relevant mechanisms. The application of the method is discussed in terms of flows where the low order modes which make a

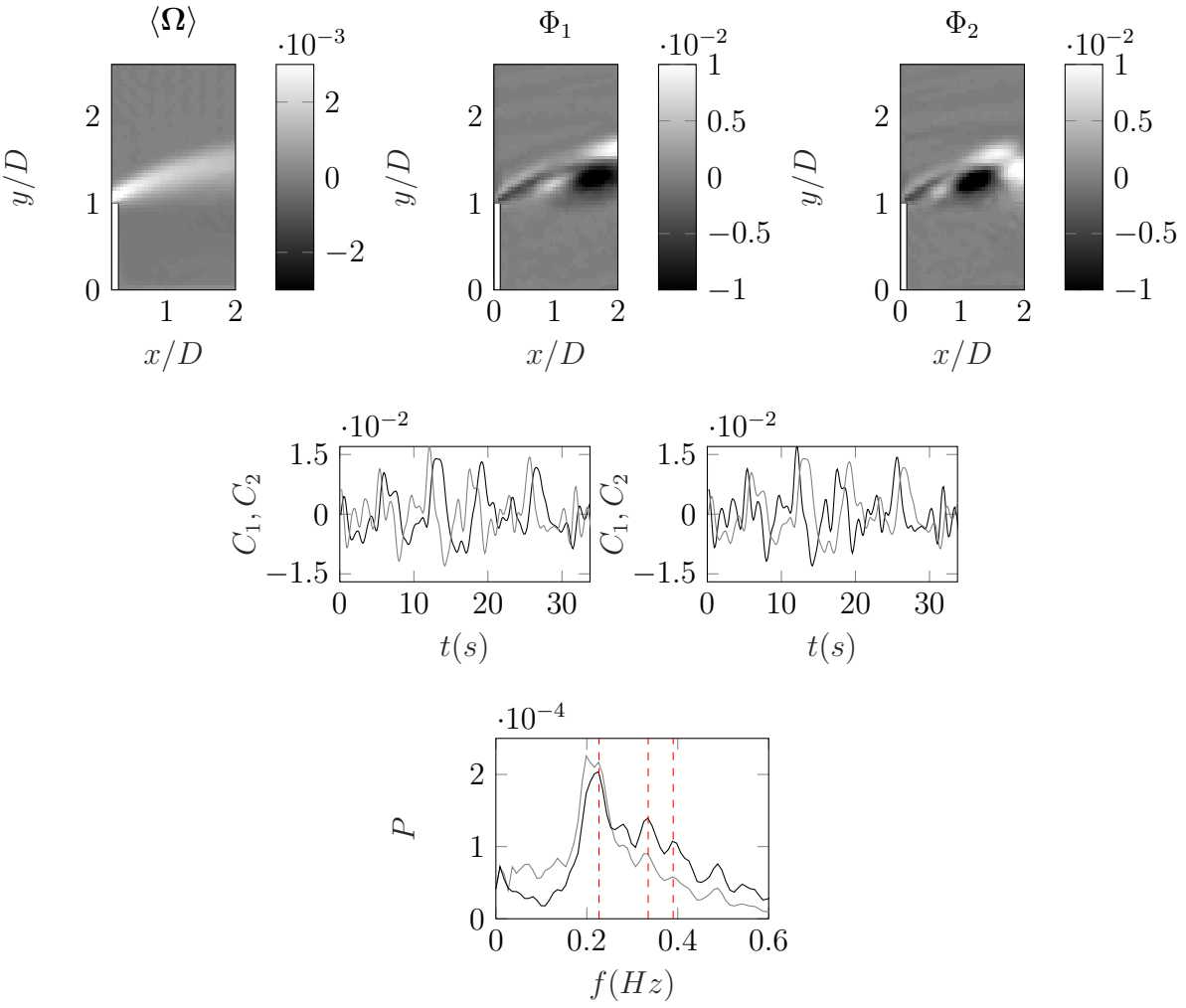

FIGURE 4.5: POD results of the vorticity field of the shear layer generated by a lateral groyne in a shallow flow (groyne highlighted in white). The top row shows the time averaged vorticity field and the spatial modes, $\mathbf{\Phi}_1$ & $\mathbf{\Phi}_2$. The central row shows the temporal coefficients $\mathbf{C}_1$ & $\mathbf{C}_2$, where the grey line denotes the mode which forms the conjugate pair. The bottom row shows Fourier Power Spectrum of the temporal coefficients $\mathbf{C}_1$ & $\mathbf{C}_2$ (grey). The red dashed lines highlight the frequencies extracted using the DMD.

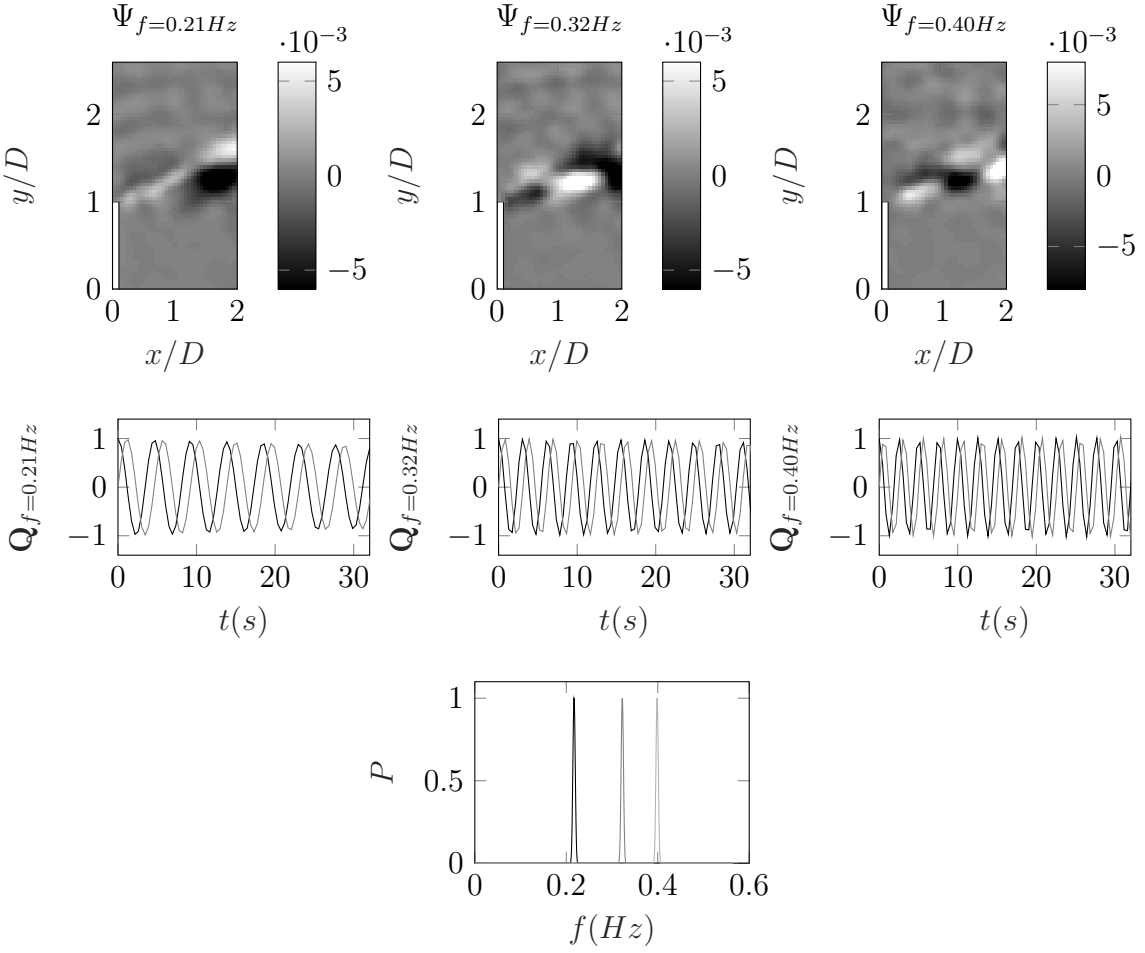

FIGURE 4.6: DMD results of the vorticity field of the shear layer generated by a lateral groyne in a shallow flow. The top row shows the spatial modes $\mathbf{\Psi}_{f=0.21Hz}$, $\mathbf{\Psi}_{f=0.32Hz}$ & $\mathbf{\Psi}_{f=0.39Hz}$. The central row shows the temporal coefficients, $\mathbf{Q}_{f=0.21Hz}$, $\mathbf{Q}_{f=0.32Hz}$ & $\mathbf{Q}_{f=0.39Hz}$, where the solid line are the real part and the grey line is the imaginary part. The bottom row shows the Fourier spectrum of the temporal coefficients

very large contribution to the total variance. The results of the test cases agree with the expected performance of the decomposition methods. POD shows great potential to explain the dynamics of Q2CS as their behaviour is linear in the far field. However it is shown that in the near field, where vortices are in transition towards a Q2CS behaviour, POD has the potential to convolve the dynamics of different flow structures. Although their spatial structure can be extracted from the signal if their associated frequencies are identified and then extracted from the DMD results. The search criteria proposed here is not expected to be valid for three-dimensional flows because of the linear nature of the additive separation. However, for shallow flows, it improves existing methods for extracting physically significant turbulence behaviour from experimental or numerical datasets based on modal decompositions.

Chapter 5

Using modal decompositions to explain the sudden expansion of the mixing layer in the wake of a groyne in a shallow flow

The sudden expansion of the mixing layer created in the wake of a single groyne is investigated using Particle Image Velocimetry. In the region of the sudden expansion a patch of high Reynolds shear stresses are observed. Using low-order representations, created from a Dynamic Mode Decomposition and a search criteria based on a Proper Orthogonal Decomposition, the spatio-temporal mechanism of the sudden expansion is investigated. This chapter demonstrates the sudden expansion is created by the periodic coalescence of eddies. These eddies originate from the upstream separation and the tip of the groyne and merge with recirculating eddies created, downstream of the groyne, at the interface of the mixing layer and the lateral wall.

5.1 Introduction

The main goal of this chapter is to investigate the spatio-temporal mechanisms and Q2CS (quasi-two-dimensional coherent structures) relating to the sudden expansion of the shallow mixing layer. Whilst, the occurrence of this has been previously observed, the physics leading to it has not. Such an interpretation of the physics is important, as this understanding will help one to hypothesise how different flow and boundary conditions will affect the formation and dynamics of the sudden expansion. This is particularly important from an environmental perspective as the increased moment fluxes relating to this phenomenon can lead to enhanced scouring / mixing processes. To investigate these mechanisms an experimental PIV study is undertaken. To describe the spatio-temporal mechanism a low-order reconstruction of the flow is made from a DMD based on the search criteria outlined in the in Chapter 4.

5.2 Experimental setup

The experimental flow conditions in this chapter is the same as in Chapter 4. To capture the large-scale turbulent structures, a planar Particle Image Velocimetry (PIV) measurement system was used. The PIV system consisted of an industrial grade camera with a 1200×1200 CCD-sensor with 12 bit resolution. The flow was seeded with floating 2.5 mm hexagonal polyester particles using a pneumatic particle dispenser. In a shallow flow floating particles have previously been shown to be effective in capturing the large scale turbulent motions by (Weitbrecht et al. 2002). The camera was mounted directly above the water surface at a height of 1.5 m and was set to capture an area of 150 × 45 cm with 5 cm overlapping

between upstream and downstream images. Measurements were conducted in eight consecutive planes, one upstream of the obstacle and seven downstream.In each position snapshots were recorded at an acquisition frequency of 37 Hz. The image sequence was analysed using the PIV package for Linux GPIV van der Graaf (2010), using multi-pass and image deformation techniques. As discussed by Huang et al. (1997) digital PIV often has an associated error, this error can be associated to the seeding distribution. The work of (Higham et al. 2016) also shows outlier vectors can increase this error. In the present study it is estimated these errors are approximately 4%. To reduce the influence of the outlier error the PODDEM algorithm (Higham et al. 2016) was implemented (see Fig. 5.1).

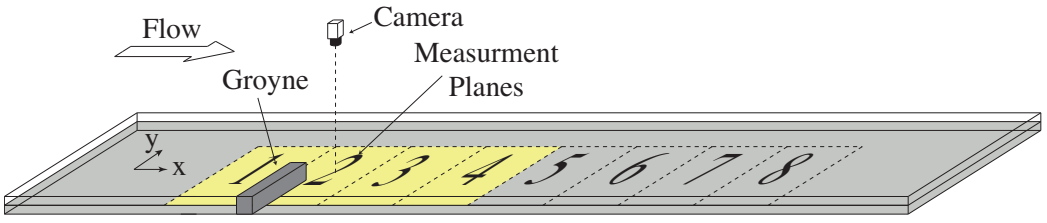

FIGURE 5.1: Sketch of the experimental setup (not to scale)

5.3 Results

5.3.1 Time-averaged statistics

As previously outlined, the emphasis of this chapter is to describe the mechanisms underpinning the sudden expansion of the mixing layer. Before investigating the spatio-temporal mechanisms, time-averaged statistics are used to find its location and investigate any related turbulent properties. Time-averaged statistics are created separately from 8 PIV planes, each obtained from 21,000 velocity fields.

The co-ordinate system is normalised by the length of the groyne, L, and the axes are termed x/L and y/L. The co-ordinate system originates in the x-direction at the centre of the groyne and in the y-direction where the groyne meets the wall. The data obtained are two component velocity fields u (x-direction) and v (y-direction), see Fig. 5.1. Fig. 5.2 presents a time-averaged overview of the flow system, where (a) shows the time averaged streamwise velocity component normalised by the bulk velocity U_0, (b) shows the time averaged spanwise velocity component normalised by U_0 and (c) Ω normalised by its spatial-temporal average, Ω_0. All figures are overlaid by the mean streamlines.

As shown in Fig. 5.2 as the flow approaches the groyne it separates. The separation of the flow creates a mixing layer bounding two counter rotating recirculation zones, which reattaches with the lateral wall at x/L$\sim$ 11. The first counter-clockwise rotating recirculation cell extends the whole spanwise length of the obstacle (y/L= 1) and three obstacle lengths downstream (x/L= 3). The second downstream recirculation cell is clockwise rotating and originates from the tip of the obstacle. Due to the first downstream recirculation cell, this cell does not meet the lateral wall until x/L= 3. The interface between these two recirculation cells and the mixing layer is located around the same point as the sudden expansion (highlighted in Fig. 5.2(a) by a white circle). The sudden expansion is further shown to occur in the streamwise autocorrelation function in Fig. 5.3 (the locations of the two chosen points are highlighted in Fig. 5.2(a)). From the streamwise autocorrelation function the sudden expansion is highlighted by a increase in size of the integral time scale, before and after the sudden expansion (the two chosen points are highlighted in Fig 5.2(a)). As shown Fig. 5.2 (c), eddies shed from the tip of the obstacle create a region of high vorticity. In this region the vorticity reaches a maximum at x/L= 1.2 and is sustained up until x/L= 3. At this point

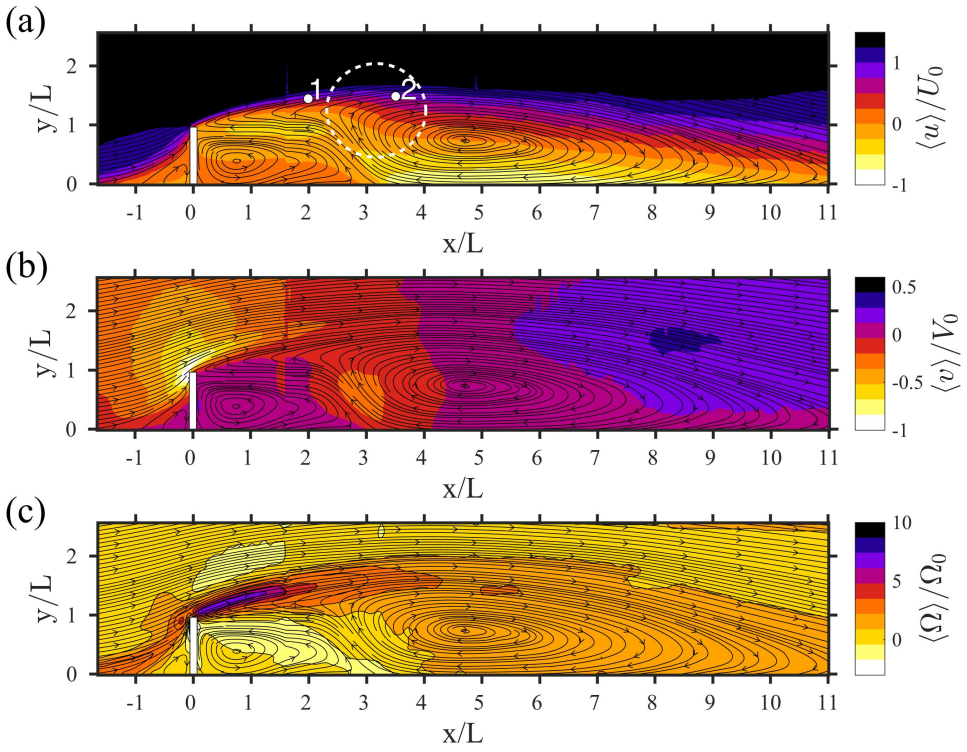

FIGURE 5.2: Mean statistics created from eight overlapping planes. (a) Shows the time averaged streamwise velocity, (b) shows the time averaged spanwise velocity, (c) shows the time averaged vorticity. The white dashed circle in (a) highlights the location of the sudden expansion of the mixing layer. All contour plots have mean streamlines overlaid.

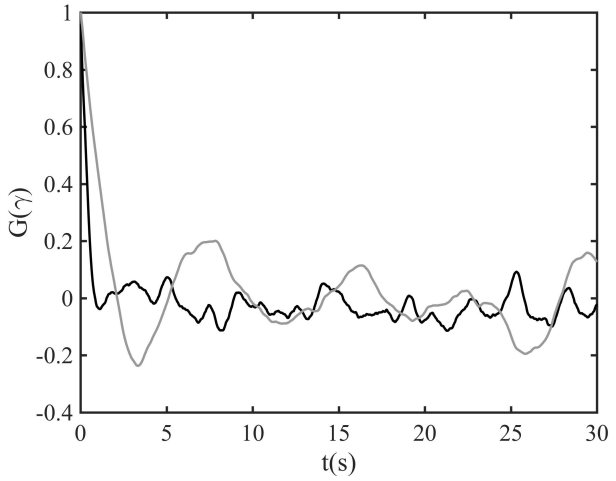

FIGURE 5.3: Streamwise autocorrelation function, G(γ), taken at two points, before and after sudden expansion. The location of the points chosen are plotted on Fig. 5.2(a). Black line relates to (1) (before expansion) and (2) grey line relates to 2 (after expansion).

the intensity of the vorticity reducues, and finally by x/L$\sim$ 4 the region of high vorticity is no longer visible.

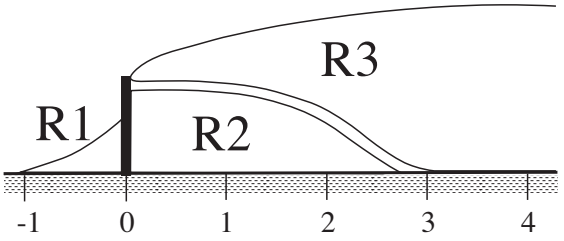

FIGURE 5.4: Nomenclature of recirculation zones

The focus now concentrates on the first four planes, as this corresponds to the location of the sudden expansion. A nomenclature for the recirculation cells is also introduced, as shown in Fig. 5.4. The upstream recirculation zone is termed R1, the first downstream recirculation zone is termed R2 and the second downstream recirculation zone is termed R3. In Fig. 5.5 (a-c) contour plots of the Reynolds stresses $\langle u'u' \rangle$, $\langle v'v' \rangle$ & $\langle u'v' \rangle$ normalised by U_0^2, and (d) contour plots of the turbulent kinetic energy, TKE=$(\langle u'^2 \rangle + \langle v'^2 \rangle)/2$ by U_0^2 are plotted. The $\langle u'v' \rangle$ contour plots show along the mixing layer, between x/L= 2 and x/L= 4 an intense patch of momentum fluxes. The centre of this intense region x/L$\sim$ 3, y/L$\sim$ 1.7, coincides with the point at which the concentration of TKE begins to decrease. From the $\langle u'u' \rangle$ and $\langle v'v' \rangle$ contour plots, it is evident that the patch seen in $\langle u'v' \rangle$ relates the change in direction of the momentum fluxes. From these plots it can be concluded that in this region a process is occurring leading to the sudden expansion of the mixing layer. To investigate the spatio-temporal mechanism responsible for this phenomenon, the modal decompositions described earlier are used to extract the primary features of interest from the complex dynamics observed in this region.

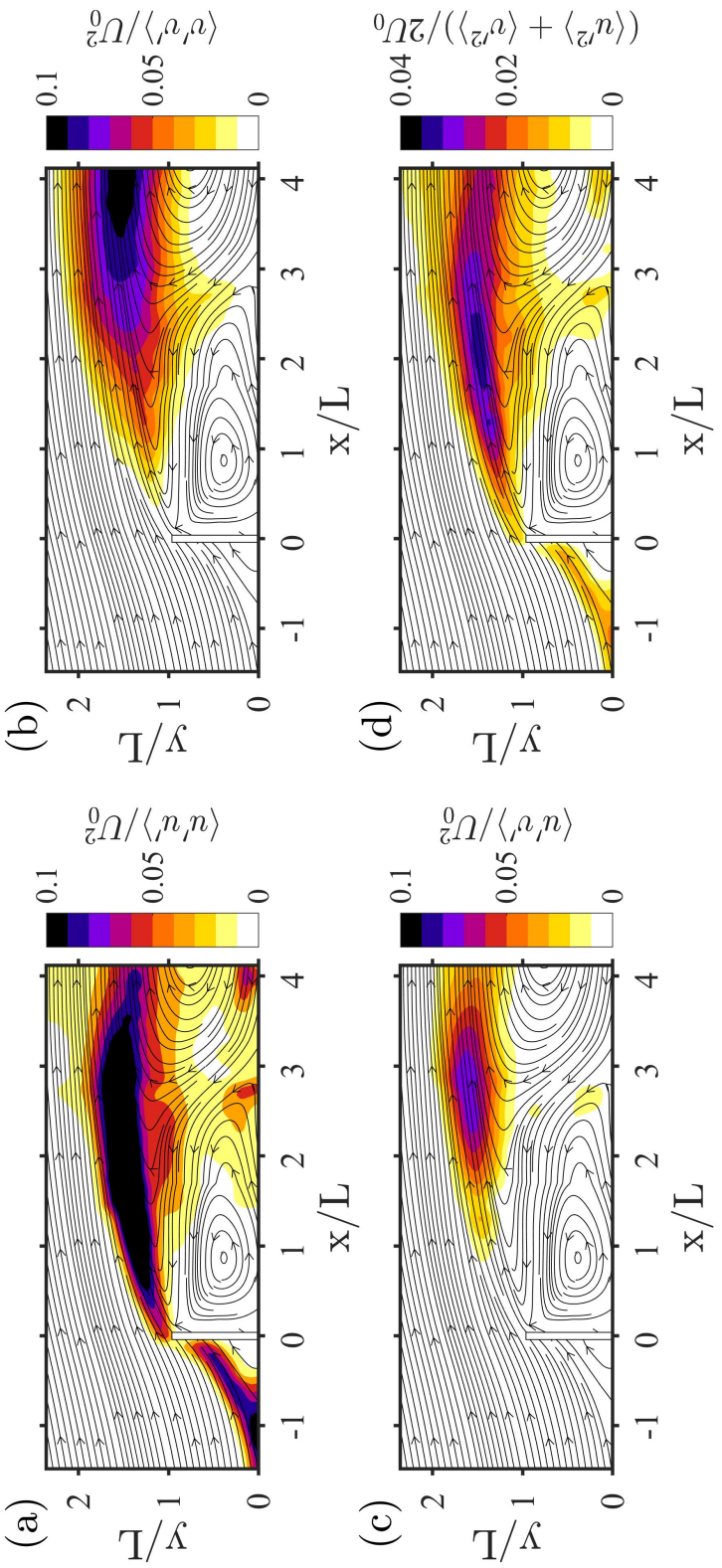

FIGURE 5.5: (a - c) Reynolds shear stresses $\langle u'u'\rangle/U_0^2$, $\langle v'v'\rangle/U_0^2$ & $\langle u'v'\rangle/U_0^2$ respectively (d) Turbulent kinetic energy $(\langle u'^2\rangle+\langle v'^2\rangle)/2U_0$.

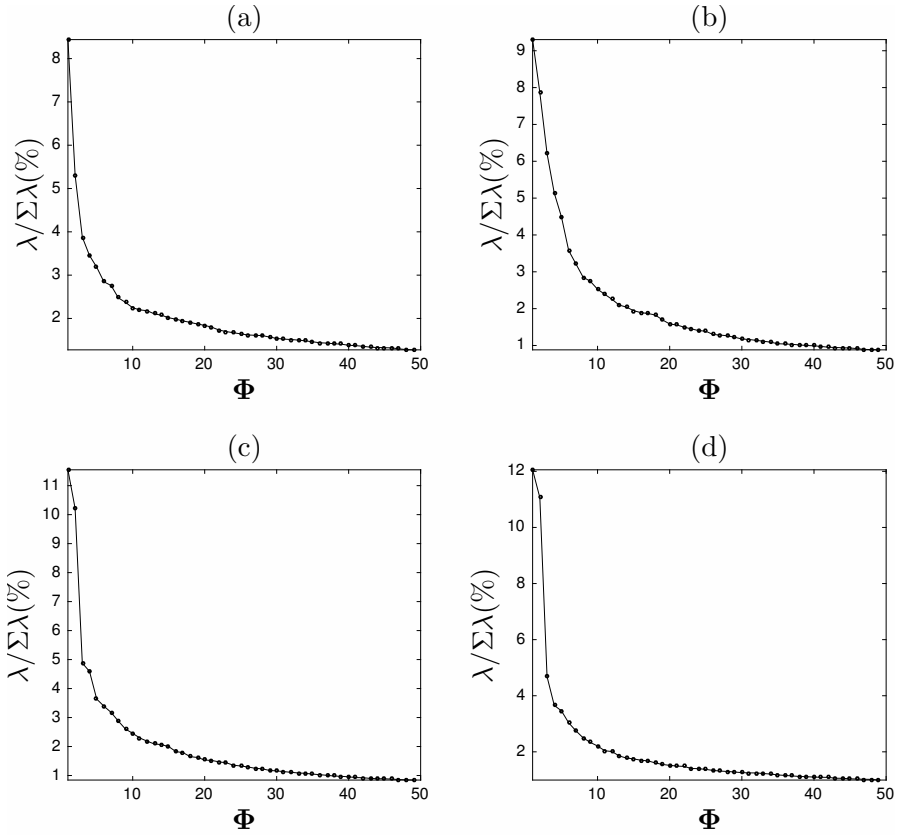

FIGURE 5.6: POD spectra where $\lambda = diag(\mathbf{S})$, these values represent each spatial modes $\mathbf{\Phi}_i$ contribution to the total variance.

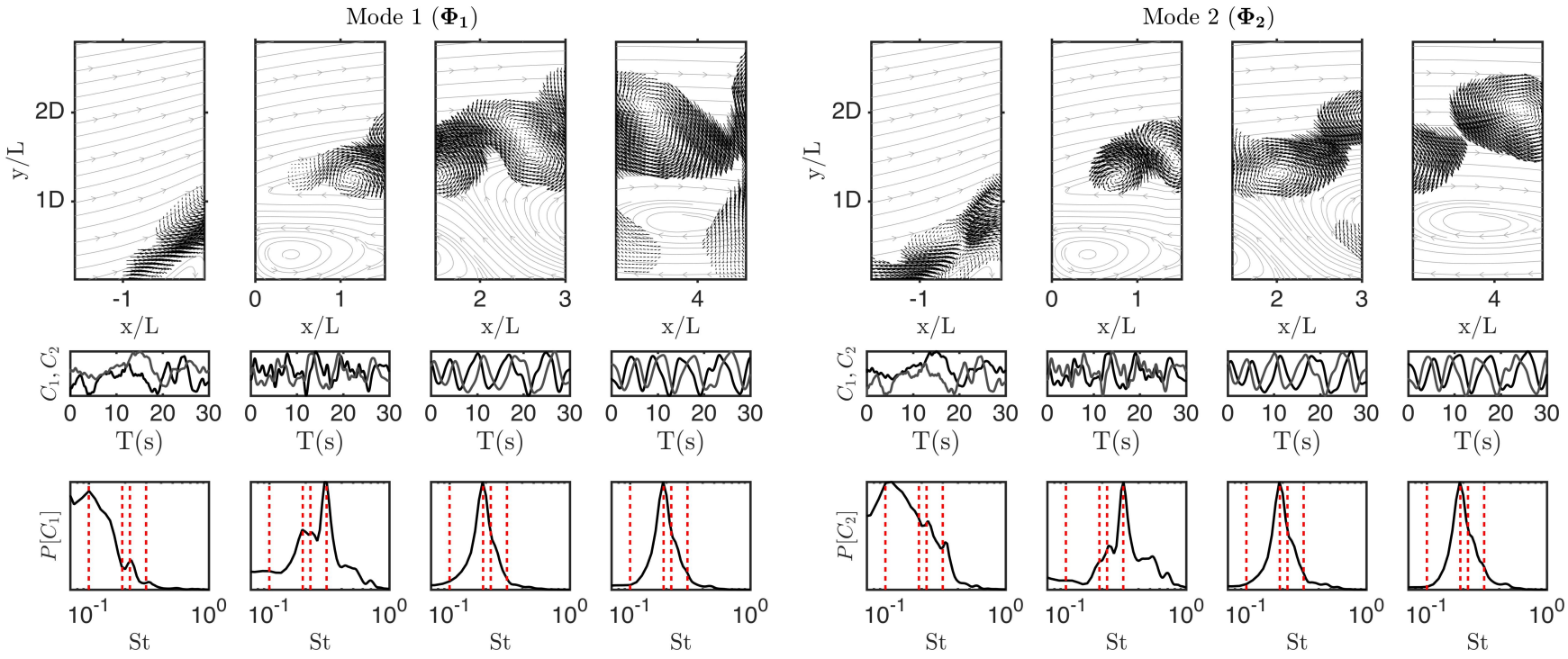

FIGURE 5.7: POD modes ($\mathbf{\Phi}_1$ & $\mathbf{\Phi}_2$) obtained from a Proper Orthogonal Decomposition of four separate planes. The top row shows the spatial modes plotted using vector plots (with a threshold implemented to highlight the spatial structures). Underneath the POD modes the mean streamlines are plotted for reference. The middle row shows a small excerpt of the temporal coefficients (black depicts the current mode, and grey depicts the neighbouring mode). Bottom row shows a power density spectrum created from the POD coefficients ($\mathbf{C}$).

FIGURE 5.8: POD modes ($\mathbf{\Phi}_3$ & $\mathbf{\Phi}_4$) obtained from a Proper Orthogonal Decomposition of four separate planes. The top row shows the spatial modes plotted using vector plots (with a threshold implemented to highlight the spatial structures), Underneath the POD modes the mean streamlines are plotted for reference. The middle row shows a small excerpt of the temporal coefficients (black depicts the current mode, and grey depicts the neighbouring mode). Bottom row shows a power density spectrum created from the POD coefficients ($\mathbf{C}$).

5.3.2 Modal decompositions

A POD is computed using 7,000 velocity fields. Only a subset is chosen due to computational limitations (which is equivalent to 30 integral time scales in the streamwise direction). The computation was undertaken on each of the four PIV planes independently. As shown in Fig. 5.6, the singular value, λ, which is computed as part of the POD can be used as a descriptor of a modes contribution to the total variance (i.e. turbulent kinetic energy). It is observed that on average the top four modes ($\mathbf{\Phi}_1$ & $\mathbf{\Phi}_2$) account for about 35% of the total variance of the flow. As a consequence it is a reasonable assumption that these four modes are likely to contain the most relevant information regarding the Q2CS structures.

In the top planes of Figs. 5.7 & 5.8 the spatial modes $\mathbf{\Phi}_{1...4}$ are presented. The modes alone present a coherent picture of the turbulent structures. As shown by Rempfer & Fasel (1994) and Brevis & García-Villalba (2011) paired modes show spatial and temporal shifted features. From $\mathbf{\Phi}_1$ and $\mathbf{\Phi}_2$ a of number observations made by Chrisohoides et al. (2003) can be verified. $\mathbf{\Phi}_1$ & $\mathbf{\Phi}_2$ show eddies being shed from the tip of the obstacle and being advected along the mixing layer before being engulfed by R3. Furthermore, in $\mathbf{\Phi}_3$ & $\mathbf{\Phi}_4$ it is evident that there is entrainment of eddies back upstream from the reattachment of the mixing layer. However, the poor suitability of the POD for this particular case, i.e. a complex non-linear flow, is highlighted in the middle panes of Figs. 5.7 & 5.8. As shown in the previous chapter it is possible to elucidate the structures shown in the POD by finding the DMD spatial modes relating to the peak frequencies. As shown in the bottom panes of Figs. 5.7 & 5.8 there are a number of peak frequencies relating to modes 1 & 2 St=$\{0.10, 0.19, 0.22, 0.31\}$, (these frequencies are highlighted by red dashed lines).

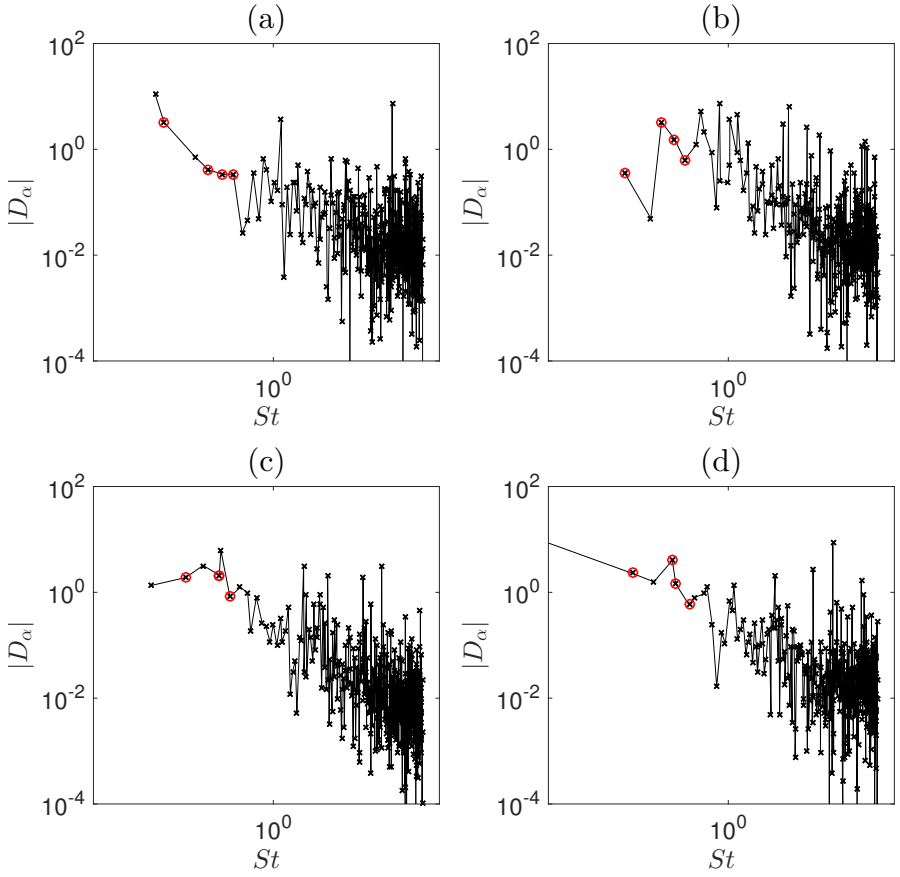

FIGURE 5.9: The DMD spectra, based on the method of Jovanović et al. (2014). The x-axis relates to the Strouhal number of each spatial mode. The y-axis relates to the amplitudes, $\mathbf{D}_\alpha$, calculated in Eq. 2.6. The red circles highlight the spatial modes identified from the power spectrum of the POD temporal coefficients (St=$0.10, 0.19, 0.22, 0.31$). For the readers reference, the high frequency, high amplitude peaks in the spectra relate to experimental/background noise.

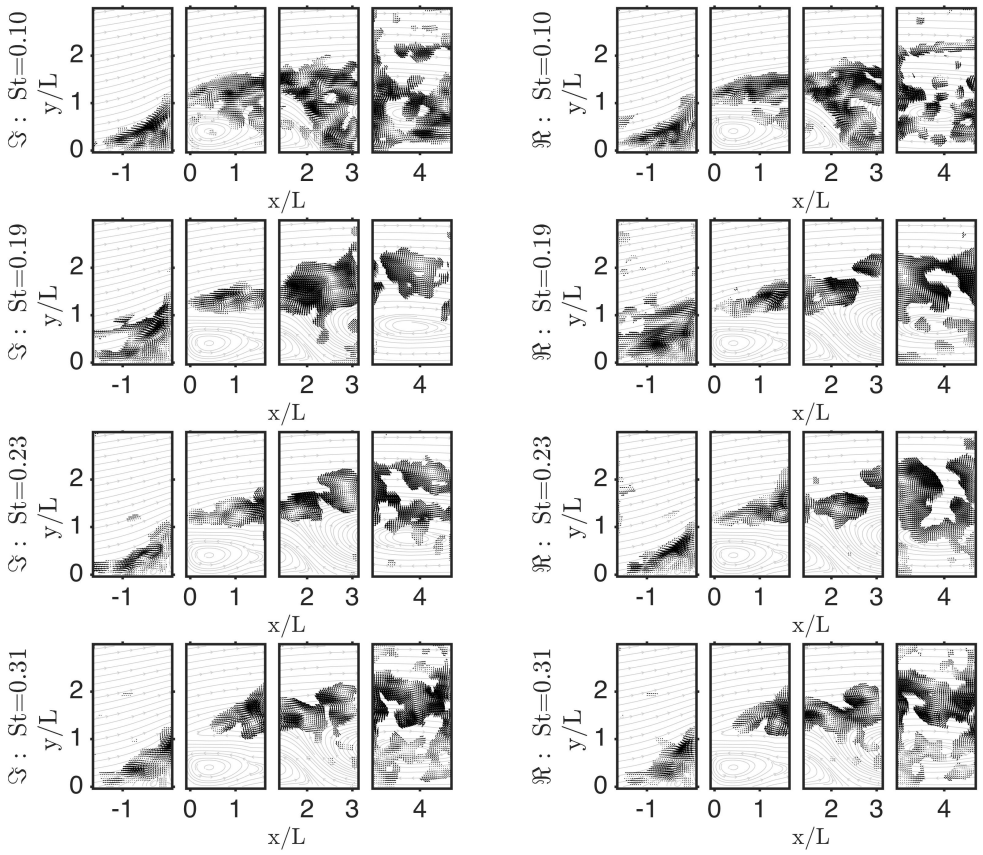

FIGURE 5.10: DMD modes $\mathbf{\Psi}_{\mathrm{St}}$, where St relates to the modes Strouhal number. The left hand column shows the imaginary component and the right hand column the real component. The time averaged streamlines are plotted beneath as a reference. (St=$0.10, 0.19, 0.22, 0.31$).

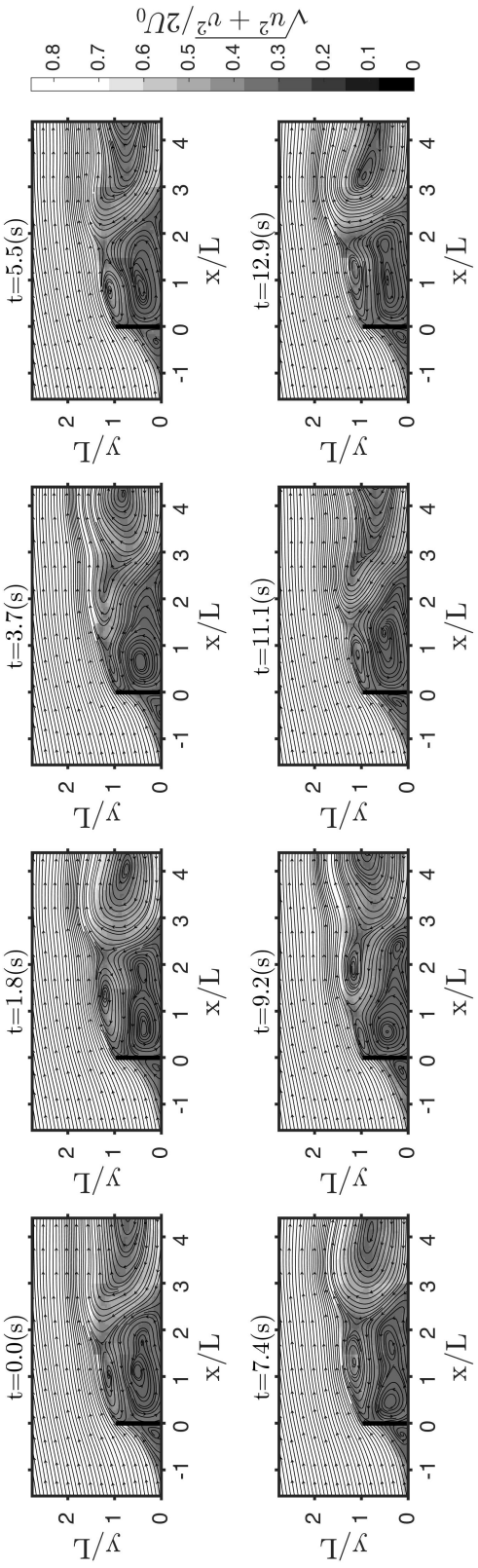

FIGURE 5.11: A low-order reconstruction of velocity magnitude overlaid by streamlines, at selected temporal locations, including the mean flow field.

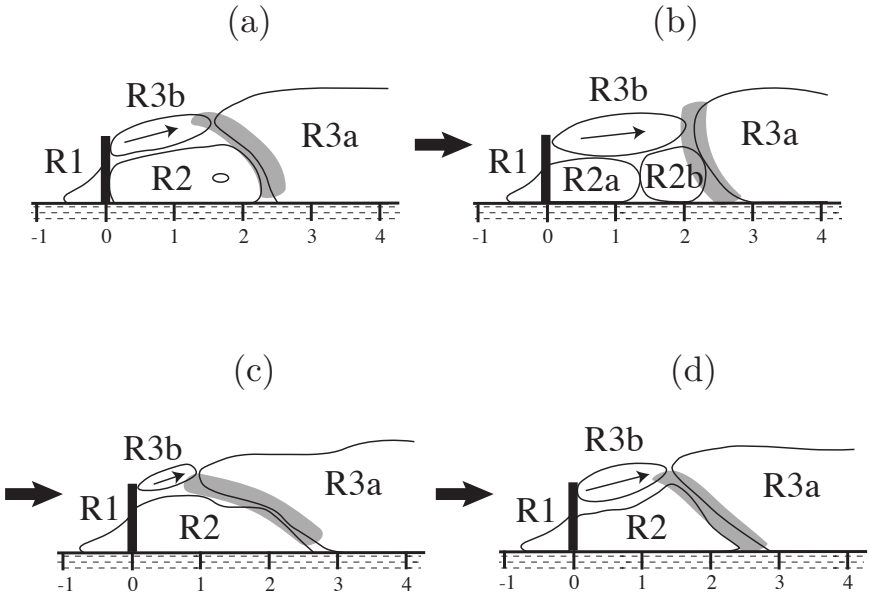

FIGURE 5.12: Schematic of the turbulent mechanism underpinning the scale jump.

Similar to the POD, the DMD was computed independently on the four separate planes each containing a smaller number of velocity fields (700), separated at a greater δt, relating to an acquisition frequency of 7.4 Hz (relating to 15 integral time scale). Only 700 velocity field are selected here to mitigate against problems of rank deficiency as discussed by Tu et al. (2014). The spectra associated to each DMD calculation are shown in Fig. 5.9, where the frequencies relating to the extracted POD modes are highlighted in red. For the reader's reference, whilst in these spectra it is apparent that they are higher frequencies with high amplitudes, from investigations not presented, it was found the majority of these modes relate to noise, originating from the experimental data. Consequently highlighting that using a Fourier description based on a POD's temporal coefficients to select the spatial modes will mitigate against incorrectly choosing insignificant DMD modes with a high $\mathbf{D}_\alpha$, created by experimental/background noise. As in a POD where paired modes represent a spatio-temporal shift, in a DMD, this shift is seen between the real and imaginary parts of $\mathbf{\Psi}$. As shown in Fig. 5.10 the DMD modes offer a clean description of turbulence processes related to single frequencies, although it is difficult to deduce mechanisms regarding the sudden expansion of the mixing layer solely from the spatial modes. Nonetheless, as shown in Eq. 2.6 it is very simple to construct a low-order representation of the flow, because each reconstruction contains the same frequencies, it is also possible to create a time evolving coherent picture of the whole system. For illustration purposes the subsequent low-order planes are concatenated, but it is reiterated that the decompositions were reconstructed independently for each plane.

As shown by the reconstruction of the velocity vectors and velocity magnitude in Fig. 5.11 the size, dynamic and number of the recirculation cells is not static. Initially there are three recirculation cells, with R3 comprised of two cells, termed

RC3a and RC3b as shown schematically in Fig. 5.12. As time progresses R3b expands and R2 simultaneously begins to stretch and split in two (R2a and R2b). The expansion of R3b causes the angle of the shear interface between the recirculation cells to periodically oscillate and the point of incidence of the shear layer and mixing layer to change. The region where the point of incidence moves about coincides with the high Reynolds stresses as seen in Fig. 5.5. This suggests that this mechanism of oscillation is associated with the sudden expansion of the mixing layer, as hypothesised by Talstra et al. (2006). To investigate the turbulent structures associated with this mechanism, Fig. 5.13 shows a low-order reconstruction based upon the fluctuating vorticity, where dark grey is positive vorticity and light grey is negative vorticity. This figure demonstrates that it is the coalescence of two eddies that leads to the sudden expansion of the mixing layer. To highlight the pairing as shown in Fig. 5.13, the two eddies are numbered (1) & (2). The first eddy (1) originates from upstream and the tip of the obstacle, the second (2) originates from vorticity injected upstream from the interaction of the mixing layer and the lateral wall. It is the constant injection of vorticity from upstream that leads to the formation of (2). Once this forms, it causes R3b to expand (explaining the periodic horizontal motion observed by Chrisohoides et al. (2003)). When (2) is sufficiently large enough it merges with (1) and advects along the mixing layer causing R3b to contract. This basic mechanism repeats itself periodically, leading to the observed dynamics, which have been documented for some time, but not previously explained satisfactorily.

5.4 Discussion

From the low-order reconstructions it is clear that the sudden expansion of the mixing layer is created by the pairing of two eddies, one created from the separation upstream and the tip of the obstacle and the other from the entrainment of vorticity, generated by impingement of the mixing layer and the wall. However, it is the interface between the two counter rotating recirculation cells that transports the second eddy into the mixing layer leading to the sudden expansion. It has previously been shown by Talstra (2011), Talstra et al. (2006) and Safarzadeh & Brevis (2016) that the shallowness of the flow leads to the production of the dual recirculation cell. The occurrence of the sudden expansion of the mixing layer is a function of the flow depth. Furthermore, previous works have shown how the effects of bed friction and the shallowness of the flow can affect the spatio-temporal dynamics of the turbulent structures / eddies (Chu & Babarutsi 1988, Uijttewaal & Tukker 1998). If the shallowness of the flow is decreased or the roughness is increased there will be an increase in the the size of eddies and the point of reattachment with the wall will change, which will affect the location of the sudden expansion. Therefore the location of the sudden expansion of the mixing layer, and its occurrence, is a function of the shallowness of the flow and the roughness of the bed. The natural environment provides both shallowness and bed roughness, meaning that, in nature, the sudden expansion of the mixing layer is likely to occur. Whilst this chapter is based upon laboratory experimental work, previous work has shown laboratory studies can be directly related to real flows Le Coz et al. (2006). However, the determination of the degree of roughness or shallowness leading the occurrence and location of the sudden expansion of the mixing layer is beyond the scope of the present study.

Whilst the occurrence of this phenomenon would seem to be problematic due to the increased momentum fluxes at the point of impingement, in fact there are a number of benefits associated with this mechanism. For example, in the first downstream recirculation cell there are no large scale turbulent structures (see Fig. 5.13), i.e. a region in which momentum fluxes are minimal and a region not susceptible to erosion, sediment transport or mixing. This region therefore protects the near upstream region of the groyne and could offer a zone which could be beneficial for fish habitats and river restoration projects.

As shown in the present study the POD and DMD methods can easily extract the large scale turbulent dynamics which govern a flow system. Whilst these methods may seem abstract, the processes which they are able to describe explain events which are of great significance in the mixing of pollutants, erosion and sediment transport. Furthermore, as shown in the present study, for complex systems with many intertwined turbulent processes, the Dynamic Mode Decomposition is able to describe these processes individually, something which could be used to create simplistic models of highly complex systems. Although the present study is based on a highly accurate PIV technique, as shown by Brevis & García-Villalba (2011) this is not a requirement, and presented techniques could easily be applied data obtained from dye tracers / flow visualisations (Constantinescu et al. 2009).

5.5 Chapter conclusions

Using a reconstruction of modes from a DMD and a selection criteria based on power spectrum obtained from the temporal coefficients of a POD the mechanism of the sudden expansion of the mixing layer is explained. The low-order representation, derived from the modes, reveals that eddies shed from the tip of the

obstacle and those created upstream of the obstacle merge with eddies recirculated from the interaction of the mixing layer with the lateral wall, leading to the sudden expansion, something previously only previously hypothesised.

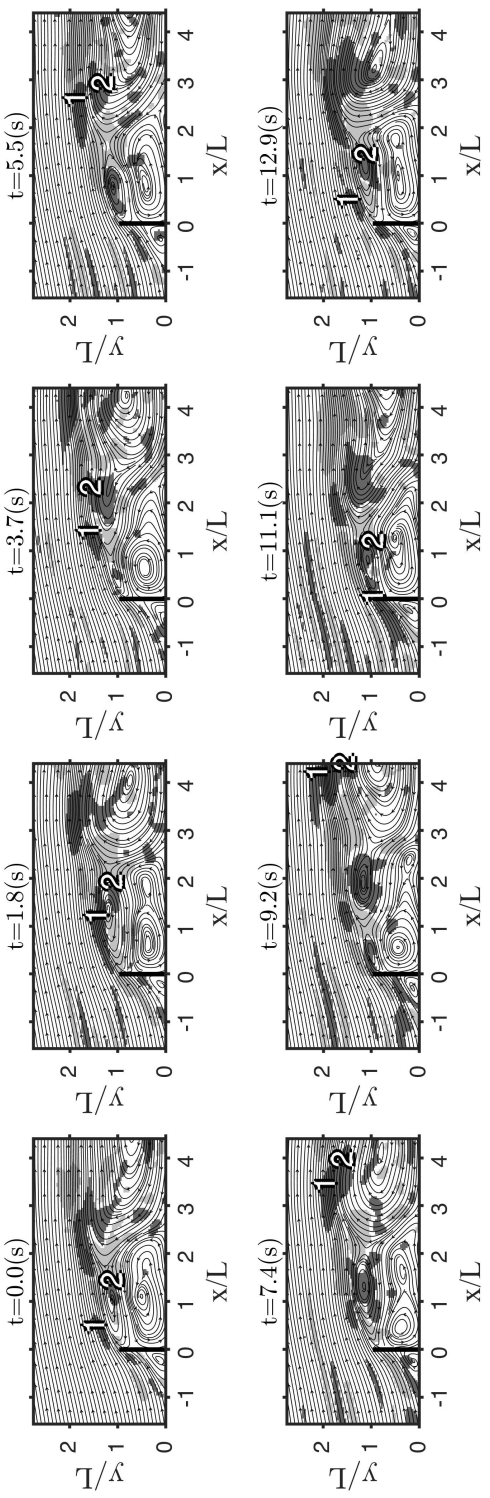

FIGURE 5.13: A low-order reconstruction at selected points of the full turbulent mechanism. Dark grey indicates positive vorticity, light grey indicated negative vorticity.

Chapter 6

Modification of the modal characteristics of a square cylinder wake obstructed by a multi-scale

An experimental study was undertaken to investigate the changes on the turbulent wake of a confined square cylinder, caused by the introduction of three multi-scale arrays of obstacles. The arrays were introduced upstream, downstream and around the square cylinder, using the same obstacles in all cases. The results show that changes on the confinement caused by the introduced elements produce an increase of the shedding frequencies and on the energy contribution of the leading modes obtained by a Proper Orthogonal Decomposition. The results also show that different modifications of the wake properties are observed if the obstacles are located either upstream or downstream of the square cylinder. When the obstacles

are mainly located upstream it is possible to observe an increase in the peak magnitude of Turbulent Kinetic Energy in the wake. These changes are associated to a redistribution of the energy contribution of the POD modes. For larger regions obstructed upstream, the leading modes reduce their energy contribution, while the higher order modes increase it. To further elucidate the turbulent structures the method from Chapter 4 is used. It is also observed that an increased reattachment length can be obtained by locating most of the array downstream of the square cylinder. All these observations are discussed in terms of the expected interactions of flow structures. From the results it is possible to conclude that the general spatial patterns of the Proper Orthogonal Decompositions modes are not changed importantly by the introduction of the arrangements compared with the unconfined case and previously reported confined cases with lower Reynolds number. The most relevant changes for the confined obstructed case analysed here can be found in the shedding frequency and the modal energy distribution.

6.1 Introduction

In this chapter an experimental study is undertaken to quantify the modifications of the wake generated by a confined square cylinder, when it is surrounded by smaller multi-scale square elements. The aim of this work is two fold: First to investigate how surrounding a confined square cylinder with smaller elements can modify the wake, and second to investigate how different arrangements of these elements can change its properties. As previous research has shown that real world distributions of buildings within cities can be well represented by fractal geometry (Batty & Longley 1994), this work reproduces a self-similar situation deriving the arrangement of the smaller elements from a Sierpinski Carpet (Sierpinski 1916).

To elucidate the flow regions of high spatial coherence, a POD is used. As there is no modal decomposition available in the literature for the flow around a confined square cylinder for a high Re_D, this research also expands the observations obtained for a confined flow at low Re_D (Rehimi et al. 2008). Furthermore to elucidate complex intertwined structures the modes relating to the peaks of the higher-order modes are extracted using the method outlined in Chapter 4.

6.2 Experimental setup

Four experimental cases are examined in this work. The first one corresponds to the benchmark and will be termed case I. This case is a single confined square cylinder, with a length scale of a third of the channel width. Case II, corresponds to a deterministic Sierpinski carpet (Sierpinski 1916), with three iterations, where iteration I is of the same dimension and position as the cylinder used in case I. In this work iteration I represents the cylinder of interest while iteration II & III correspond to the length scales of the elements surrounding iteration I. Following the rules for the Sierpinski carpet generation, iteration II has a length scale equal to one third of the length scale of iteration I. Analogously, iteration III has a length scale of one third of iteration II. Cases III & IV contain the same elements as case II, however the position of the largest element have changed longitudinally (see Fig. 6.1).

The experiments were carried out in a recirculating open channel water flume at the University of Sheffield, UK. The flume is 18 m long and B=0.49 m wide, with bottom and side glass walls thus allowing full optical access. The depth of the water was set to 0.30 m, U_0 = 0.07 m/s, Re_D=11,000 and the Froude number Fr=0.04. The dynamics of the flow was captured using PIV measurements. The

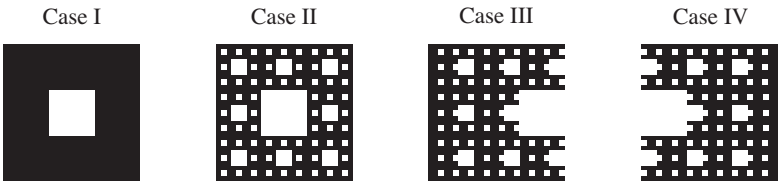

FIGURE 6.1: Plan view of experimental cases.

array was located 8 m downstream of the inlet and all measurements were carried out downstream of the array. Each element within the arrays was constructed out of 6 mm acrylic sheet cut to 0.1 mm precision using a laser cutter. The flow was seeded with Polyamide 12 particles with a mean diameter of 100 μm and density of 1.016 gcm^{-3}. These particles were illuminated using a laser plane generated from a double pulsed Nd:YAG 200mJ laser at 40% of the flow depth (0.12 m). The movement of the illuminated particles was recorded using two synchronised Imager MX 4MP cameras mounted below the flume bed, and capturing an area of 0.44 m $\times$ 0.72 m (with an overlap of 0.05m). Image pairs were captured at 77 Hz. The PIV calculations were undertaken in the software Davis 8.0, using multi-pass and image deformation techniques (Scarano 2002). The multipass interrogation windows ranged from 64 to 16 px, with an overlap of 75%. From the measurements, and along the centreline of the flow, it was determined that $u'_{rms}/\langle u \rangle$ was 7.8% and the spanwise turbulence intensities, $v'_{rms}/\langle u \rangle$, was 5.8%, were u' and v' are the root-mean-square values of the streamwise and spanwise fluctuating components. The outlier vectors were detected and removed using the PODDEM algorithm (Higham et al. 2016). The experimental parameters are summarised in Table 6.1 and a schematic of the experimental set-up is shown in Fig. 6.2. For all measurements the origin of the coordinate system is located at the centre of the largest square cylinder.

Seeding	Type	Polyamide powder
	Specific gravity	1.016 gcm^{-1}
	Diameter	100 μm
Light sheet	Laser type	Double pulsed Nd:YAG
	Maximum energy	200 mJ
	Wave length	532 nm
	Thickness	2mm
Camera	Type	Imager MX 4M
	Resolution	2048 × 2048 px
	Pixel size	0.21 mm
	Lens focal length	24 mm
Imaging	Viewing area	440 mm × 440 mm
PIV Analysis	Interrogation area	integration window size 16 × 16 px
	Overlap	75%
	Approximate resolution	3.5 mm × 3.5 mm × 3.5 mm

TABLE 6.1: PIV experimental parameters

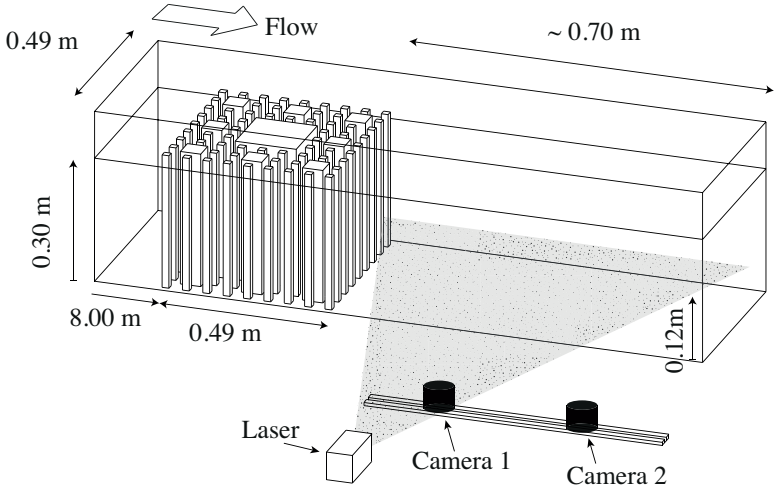

FIGURE 6.2: View of the measurement section and experimental setup (not to scale)

6.3 Results

Time-averaged statistics were calculated from 15,000 snapshots. For reference, Figs. 6.3 & 6.4(a-c) show the contour plots of the streamwise velocity component and time-averaged statistics at the centre-line, respectively. A POD was computed on the 15,000 fluctuating velocity fields. In Fig. 6.5 the POD spectrum is presented

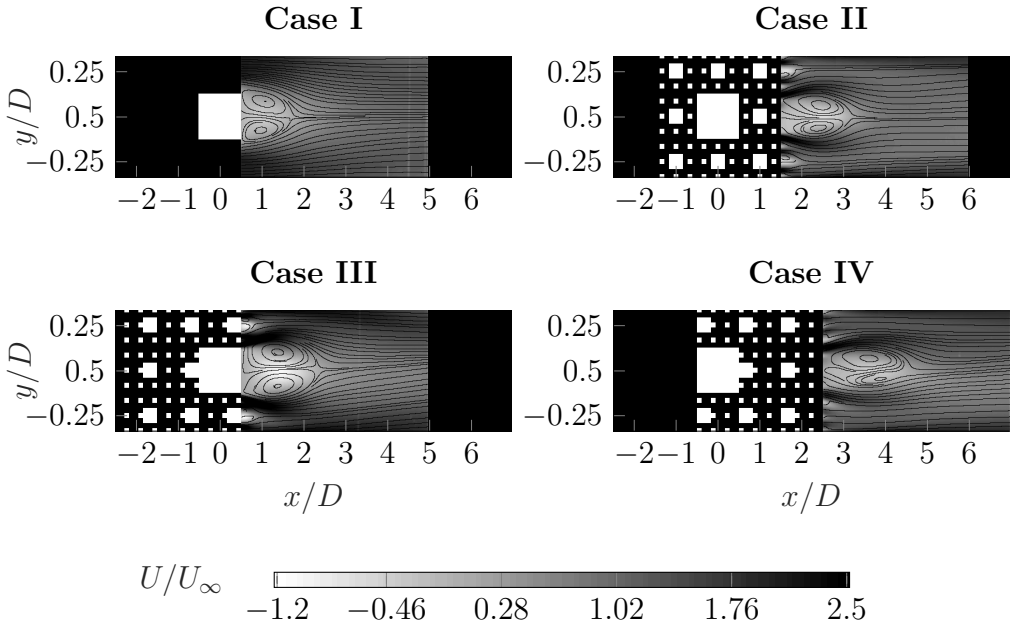

FIGURE 6.3: Contour plots of the streamwise mean velocity, U, normalised by the bulk velocity, U_0, with streamlines overlaid

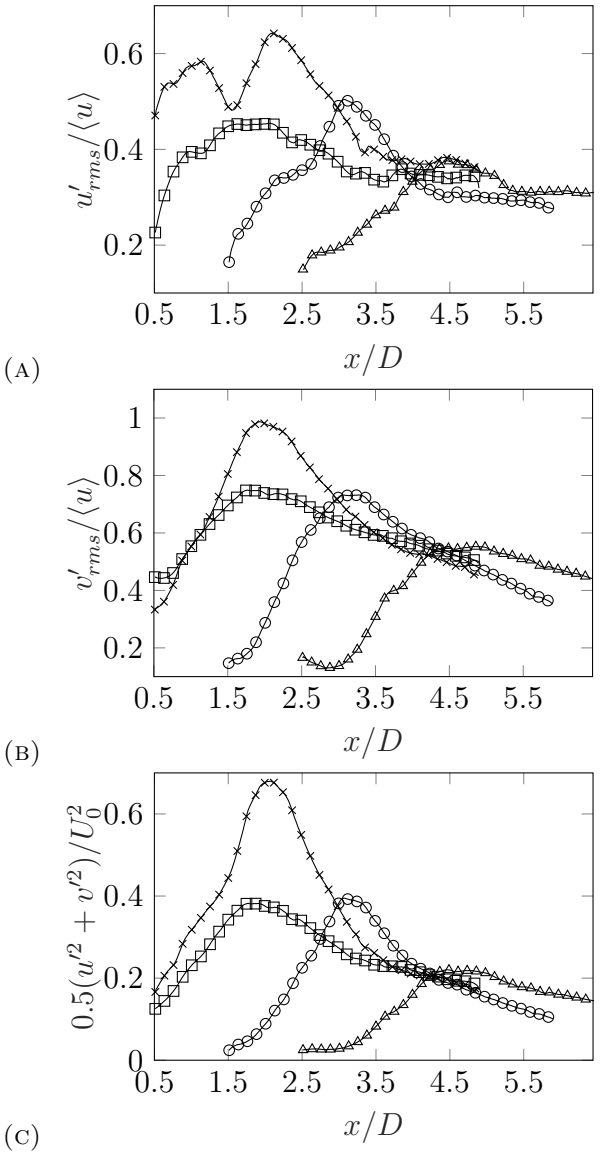

FIGURE 6.4: Centre line time averaged statistics. Case I – □, case II – ◯, case III – × & case IV – △. (a) $u'_{rms}/\langle u \rangle$, (b) $v'_{rms}/\langle u \rangle$ & (c) $0.5(u'^2 + v'^2)/U_0^2$.

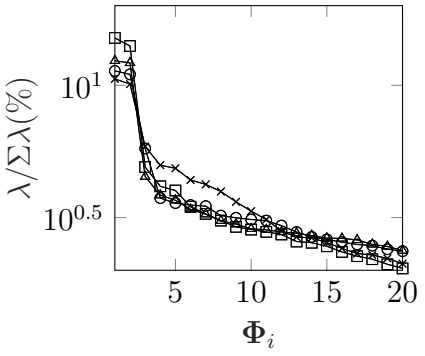

FIGURE 6.5: POD spectra where $\lambda = diag(\mathbf{S})$, these values represent the contribution of each the spatial modes $\mathbf{\Phi}_i$ to the total variance. Case I – □, case II – ◯, case III – × & case IV – △.

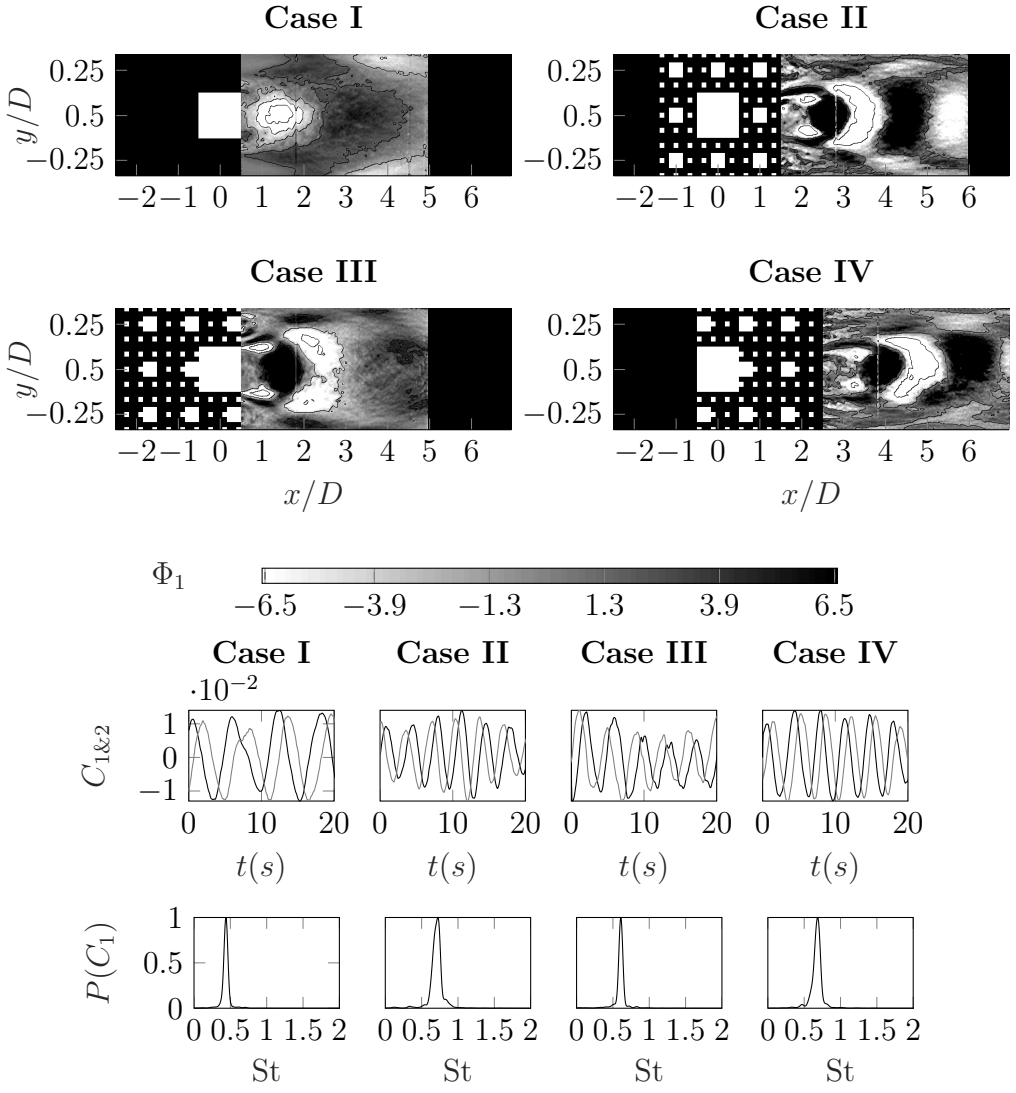

FIGURE 6.6: Top: POD modes $\mathbf{\Phi}_1$. Middle: POD temporal coefficients $\mathbf{C}_1$&$\mathbf{C}_2$ (grey). Bottom: Fourier power spectrum of $\mathbf{C}_1$. ($\mathbf{\Phi}_2$ is not plotted as it is a conjugate pair of $\mathbf{\Phi}_1$.)

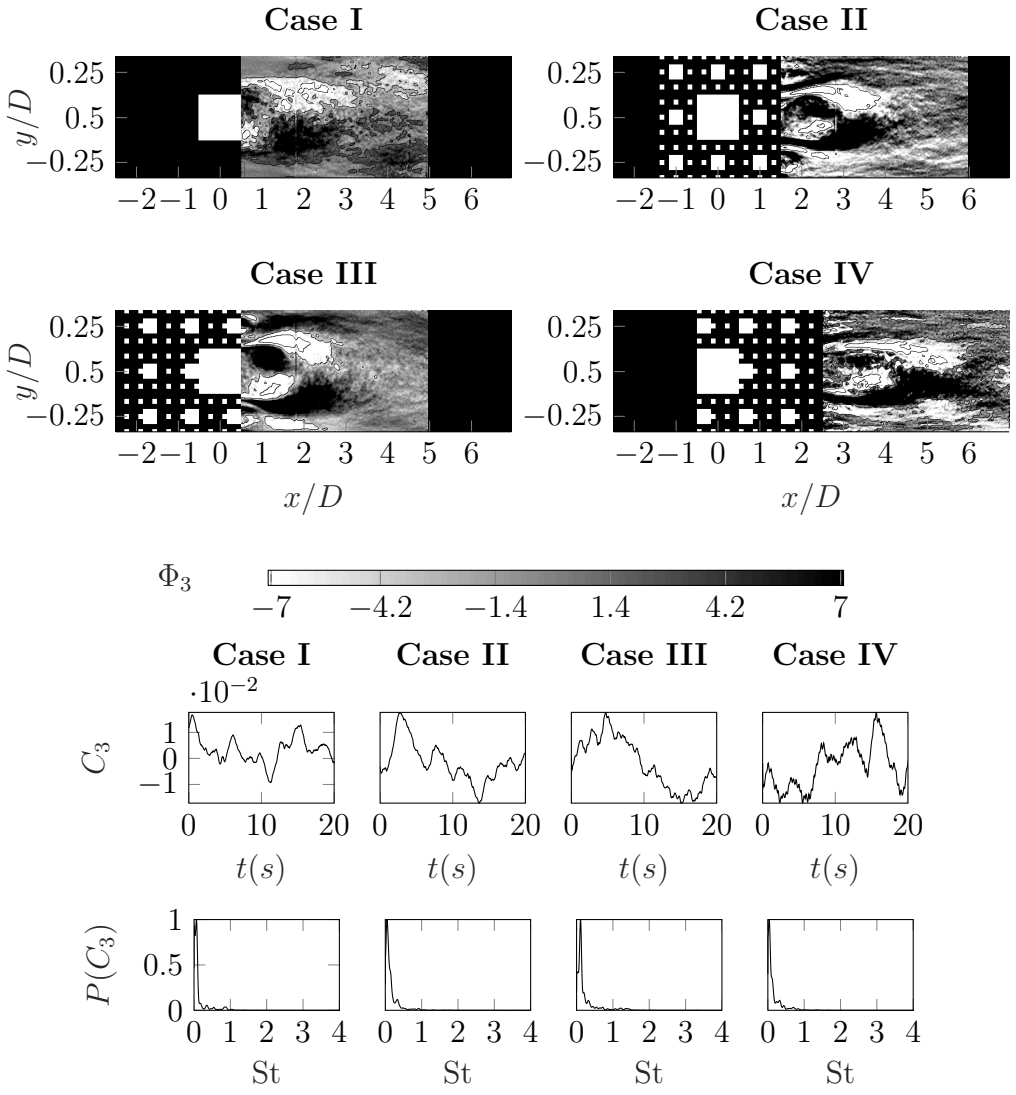

FIGURE 6.7: Top: POD modes $\mathbf{\Phi}_3$. Middle: POD temporal coefficients $\mathbf{C}_3$. Bottom: Fourier power spectrum of $\mathbf{C}_3$.

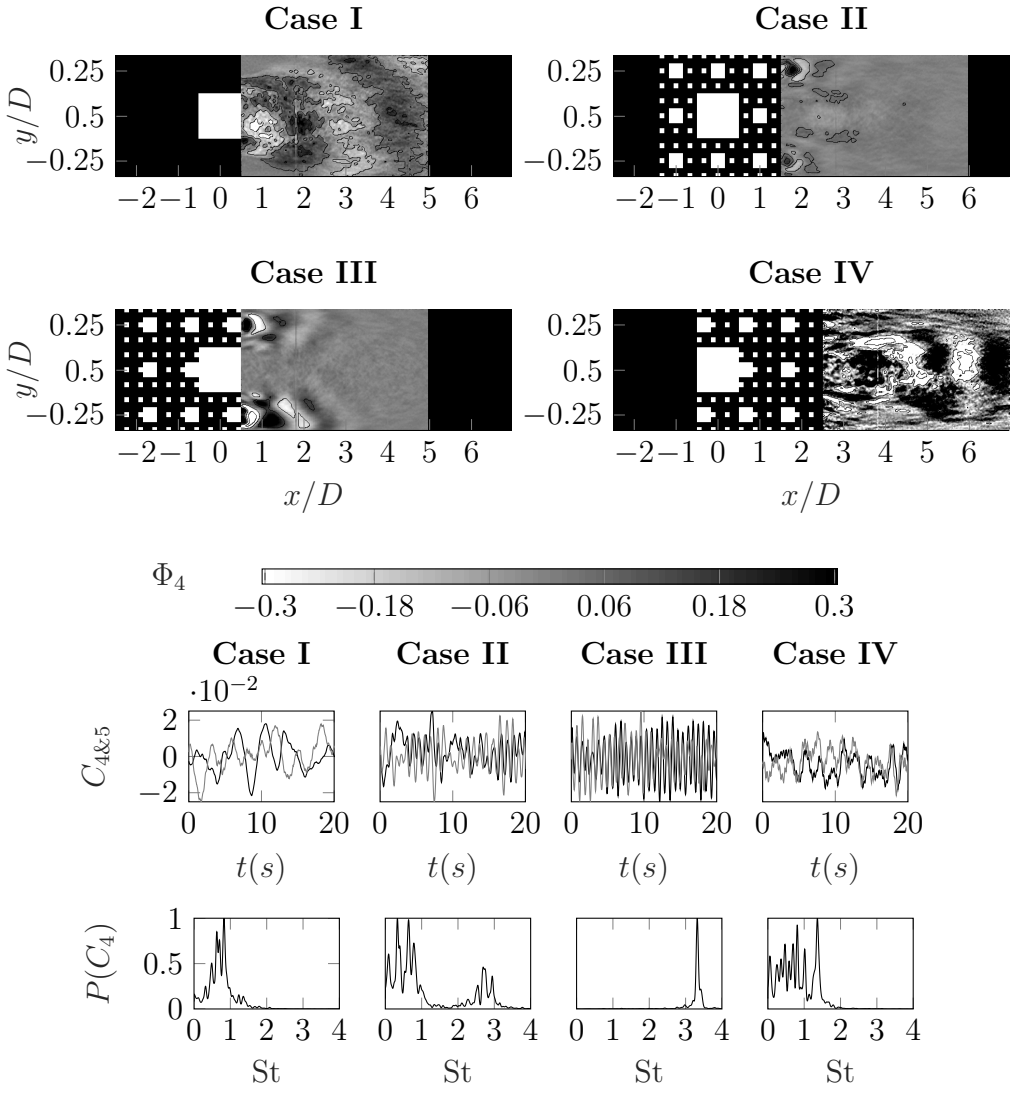

FIGURE 6.8: Top: POD modes $\mathbf{\Phi}_4$. Middle: POD temporal coefficients $\mathbf{C}_4$&$\mathbf{C}_5$ (grey). Bottom: Fourier power spectrum of $\mathbf{C}_4$. ($\mathbf{\Phi}_5$ is not plotted as it is a conjugate pair of $\mathbf{\Phi}_4$.)

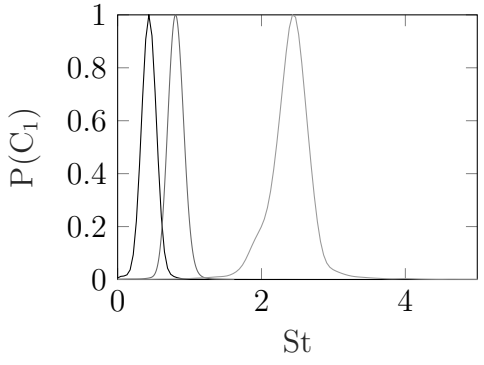

FIGURE 6.9: Power spectrum of the wake generated by iteration I (back line), iteration II (dark grey), iteration III (light grey) respectively. Peak St is St = {0.43, 0.82, 2.48} for iterations I, II & III respectively.

for the first 30 modes of each case. The points show the energy contribution of each mode relative to the total number of modes present in the signal i.e. the turbulent kinetic energy (TKE) of the flow. Fig. 6.6, 6.7, & 6.8 show the vorticity derived from the spatial velocity modes $\mathbf{\Phi}_i$, a subregion of the temporal coefficients $\mathbf{C}_i$ and the power spectra of the temporal coefficients, $P\{\mathbf{C}_i\}$. Finally a DMD was calculated from 5,000 velocity fields. Fig. 6.10, & 6.11 show the vorticity derived from the spatial velocity modes $\mathbf{\Psi}_i$ a subregion of the temporal coefficients $\mathbf{Q}_i$ and the power spectra of the temporal coefficients, $P\{\mathbf{C}_{1\&4}\}$ respectively. In the DMD figures the modes, i extracted relate to the peak frequencies highlighted in red.

6.3.1 Confined single square cylinder

The quantification of the effects of the surrounding small element on the wake developed by the largest square cylinder, implies the characterisation of a baseline for comparison, in this case the wake produced by the largest cylinder alone (case I). Also as a baseline reference, Fig. 6.9 shows the peak frequency associated to the wake of each iteration when they are individually placed in the flow. The peak frequencies were obtained at St=0.43, 0.82 and 2.48, for iteration I, II and III, respectively. As previously discussed, the blockage ratio, BR, of a cylinder can have important effects on the frequency of vortex shedding and on the location of the reattachment point of the separated shear layers. In the present work the cylinder is confined with BR=0.33. As discussed by Durao et al. (1988) significant features of the square cylinder wake can be obtained from the streamlines of the mean flow, and from the longitudinal profile of the TKE at the centreline. The streamlines of the mean flow can be used to identify the recirculation bubble, while the peak of the TKE can be used to identify the location of the point of

reattachment. The reattachment length is defined here as the distance between the origin of the coordinate system and the reattachment point. In the study of Durao et al. (1988) an unconfined cylinder with a similar Reynolds number (Re_D=14,000) and $u'_{rms}/\langle u\rangle$=6% was investigated. Compared to the results of Durao et al. (1988) and as shown in Figs. 6.3 & 6.4(c) the point of reattachment is protracted in the present case $\sim$ 1.4 times further downstream, however the peak TKE is reduced by a factor of $\sim$ 0.8. A similar study of an unconfined cylinder was presented by Wang & Zhou (2009). The Re_D=9,600 was similar to the present study, but with a lower $u'_{rms}/\langle u\rangle \sim 0.4\%$. The reattachment length extracted from the results of (Wang & Zhou 2009) was $\sim$ 1.1 the magnitude of the one obtained in the present study. Since the Re_D have been shown to have small effects on the reattachment length, these observations highlight the effect of $u'_{rms}/\langle u\rangle$ on the wake.

In a recent study, Wang et al. (2014) presented the characteristics of the top two spatial POD modes, which are associated to the advection of the vortices shed from the cylinder. The modes are very similar to those observed in $\mathbf{\Phi}_{1\&2}$, although their frequency is $\sim$ 0.5 times that of the frequency observed in this chapter (see Fig 6.6). Furthermore, the results of Wang et al. (2014) and the results shown in Fig. 6.5 demonstrate how the BR and $u'_{rms}/\langle u\rangle$ can affect the contribution of the large scales to the TKE. The POD spectra of the current study shows that the confinement affects the contribution of the modes to the TKE. The results show that the top two modes contain about half the energy of the contribution found by Wang et al. (2014) for the unconfined case. However the contribution of $\mathbf{\Phi}_3$, a mode representing the dynamics of the separated shear layers, is similar in both cases. The lower energy found in the current results for the top two modes, is reflected on higher energy contributions of $\mathbf{\Phi}_{i>14}$ (see Fig. 6.5). Therefore the POD spectra suggest that the increase of TKE associated to the confinement is

not associated to an increase of the energetic large scale vortices but to the smaller scale ones.

6.3.2 Confined obstructed single square cylinder

From the previous section it was shown that the BR can have important influences on the formation of the wake. In this part of the study, smaller multi-scale elements are introduced around the cylinder. By introducing these elements, a large BR of the incoming flow is obtained, thus the effect of the smaller cylinders could be considered as an equivalent BR. In the obstructed cases (cases II-IV) the BR is defined as the ratio between the sum of the spanwise length of the cylinders located at the cross-section at x=0, and the width of the channel. For all of the obstructed cases, BR=0.7. As shown previously, increasing the BR decreases the length of reattachment and may increase the shedding frequency. As shown in Fig. 6.3 & 6.4, counter-intuitively and compared with case I, in cases II, III & IV the reattachment point is protracted further downstream by $\sim$ 1.68, $\sim$ 1.1 and $\sim$ 2.4 times respectively. This observation seems to be a function of the geometrical layout of the arrangement, i.e the size of the region formed by smaller cylinders upstream or downstream of iteration I. The increase of the TKE is inversely proportional to the number of downstream elements and proportional to the number of upstream elements. For example, in case III where there are no downstream elements the peak TKE is increased by a factor of $\sim$ 1.6 the peak of case I. In case II, the peak TKE is approximately equal to case I. In case IV, where most of the element are located downstream of the large cylinder the TKE is decreased by a factor of $\sim$ 0.6 of case I. These results suggest that the upstream

elements may have an effect increasing the TKE, whilst the downstream elements reduce it.

From a Fourier Power Spectrum of the POD coefficients, it is shown that in all of the obstructed cases, the frequency of vortex shedding is ~ 3 times that of case I, $\mathrm{St} = \{0.74, 0.63, 0.69\}$. This suggests that the higher BR is still causing an increase in the shedding frequency, and different arrangements are causing a frequency difference between the arrangements, but smaller to those related to BR. Furthermore, as shown in the POD spectra in Fig. 6.5, on average the top two modes of case I contribute to ~ 1.4 times more than the other cases to the total TKE. Cases II, III and IV, contribute to $\sim 22\%$, $\sim 21\%$ & $\sim 24\%$, whilst case I contributes to $\sim 30\%$. As previously shown, the higher BR is causing a redistribution of energy at the lower modes, and different arrangements seems to be related to different distributions of energy in higher modes. As shown in Fig. 6.6, despite the introduction of the surrounding elements, in all of the cases, $\mathbf{\Phi}_{1\&2}$ describe the vortex shedding process. As highlighted in the POD spectra, the BR does not affect importantly the contribution of TKE of $\mathbf{\Phi}_3$, representing the shear interface surrounding the recirculation bubble. The spatial modes show that the larger the region perturbed downstream of iteration I, the longer the reattachment length (see Fig. 6.4(c)). From the POD spectra of the higher order $\mathbf{\Phi}_i$>14, it is possible to observe that, the larger the region perturbed upstream there is an increased contribution of higher order modes to the TKE. From a spatial point of view, $\mathbf{\Phi}_4$ shows a number of spatial differences between the cases, however it shows also clear temporal differences, which are captured by the coefficients. In case III there is a clear peak in the Fourier spectra of the temporal coefficients. In case II the shedding from smaller elements can be identified, however a different spectrum is formed revealing the presence of two broadband peaks. Finally in case IV it is

not possible to observe a clear shedding frequency, revealing the superposition of multiple processes and the development of a broadband spectrum.

6.3.3 Selecting frequencies using a DMD

Fig. 6.10 & 6.11 show the DMD spatial modes $\mathbf{\Psi}$ determined from the peak frequencies of $P\{\mathbf{C}_1\}$. From Fig. 6.10 it is possible to observe that the general spatio-temporal patterns relating to $\mathbf{\Psi}$ are similar to $\mathbf{\Phi}_1$. This is expected due to the sinusoidal behaviour of each of the $\mathbf{C}_1$, as discussed in Chapter 4. Next the DMD modes relating to $\mathbf{\Phi}_4$ are determined. The DMD modes associated to $\mathbf{\Phi}_3$ are omitted as the frequencies of the largest peaks are too low for the DMD algorithm. As shown in Fig. 6.11 apart from case III, in all of the $P\{\mathbf{C}_4\}$, there is no single peak that is well defined. In case I the $\mathbf{\Psi}_{St=0.82}$ connected with the highest peak in $P\{\mathbf{C}_4\}$ is determined. This peak frequency is approximately twice the magnitude of the well defined peak in $P\{\mathbf{C}_1\}$. From the spatial structures it is observed that compared with the POD, the DMD mode is spatially different. $\mathbf{\Psi}_{St=0.82}$ resembles the advection of a vortex created along the mixing layer. In case II the largest peak in $P\{\mathbf{C}_4\}$ is not selected. From investigations not presented here, it is shown that the $\mathbf{\Psi}$ linked to this peak has a poorly defined spatial-temporal structure. Therefore, another peak frequency was selected, if the larger peak of the highest frequency group is selected. As the $\mathbf{\Psi}_{St=0.82}$ is spatially similar to $\mathbf{\Phi}_4$ it can be concluded that this frequency is related to the vortex shedding of the second iteration. In case III in $P\{\mathbf{C}_4\}$, there is a well defined peak. The $\mathbf{\Psi}_{St=3.4}$ relating to this mode has a similar spatial picture to that presented in $\mathbf{\Phi}_4$. Finally in case IV the $\mathbf{\Psi}_i$ relating to the largest peak, is twice the frequency obtained from $P\{\mathbf{C}_1\}$. The spatial structure of this $\mathbf{\Psi}_{St=1.35}$ is very similar to that connected to $P\{\mathbf{C}_1\}$,

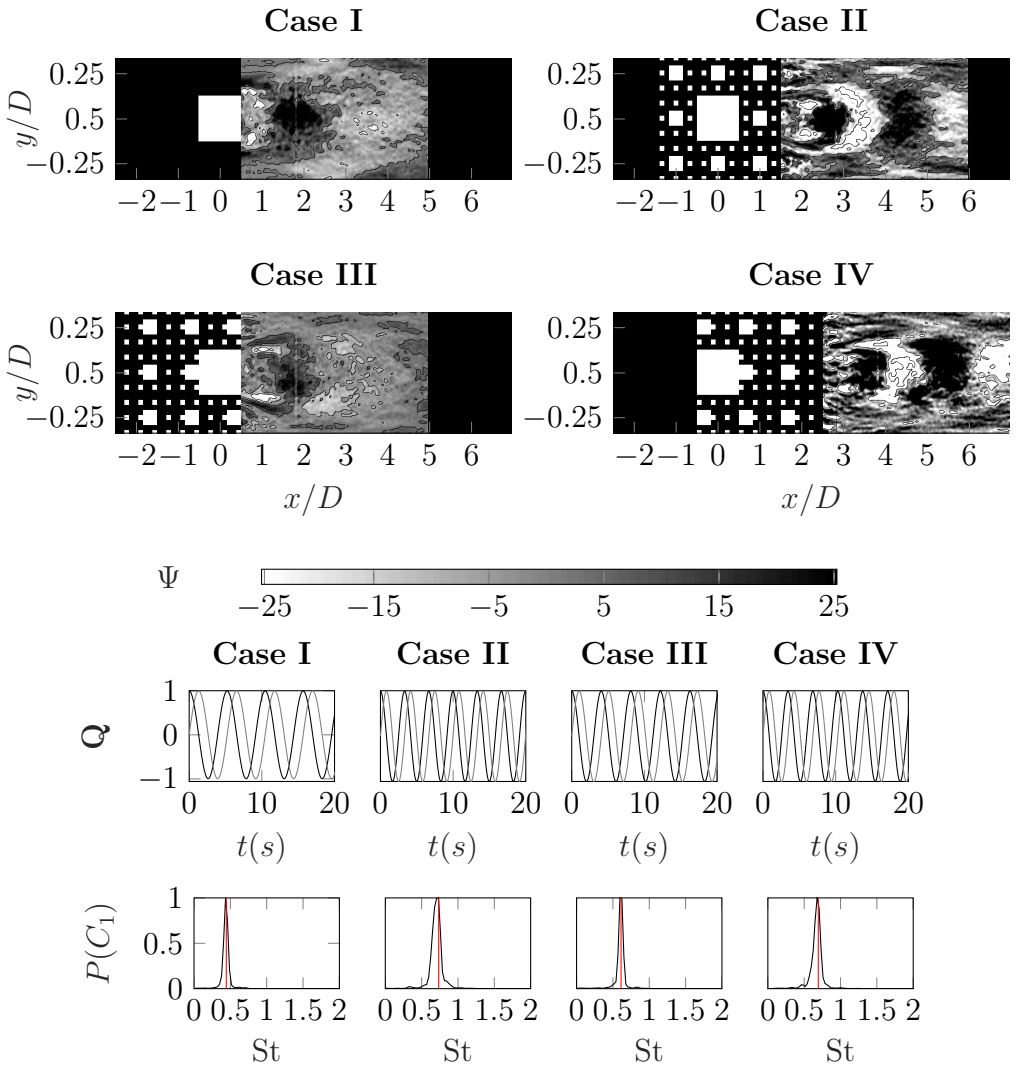

FIGURE 6.10: Top: The real component of the DMD modes $\mathbf{\Phi}$ where each extracted mode represents the peak frequencies highlighted in red. Middle: DMD temporal coefficients $\mathbf{Q}$, where the black line is the real part and the grey line is the imaginary part. Bottom: Fourier power spectrum of $\mathbf{C}_1$, with DMD spatial modes frequency highlighted in red.

this suggests that this mode is a harmonic of the peak shedding frequency of the largest iteration.

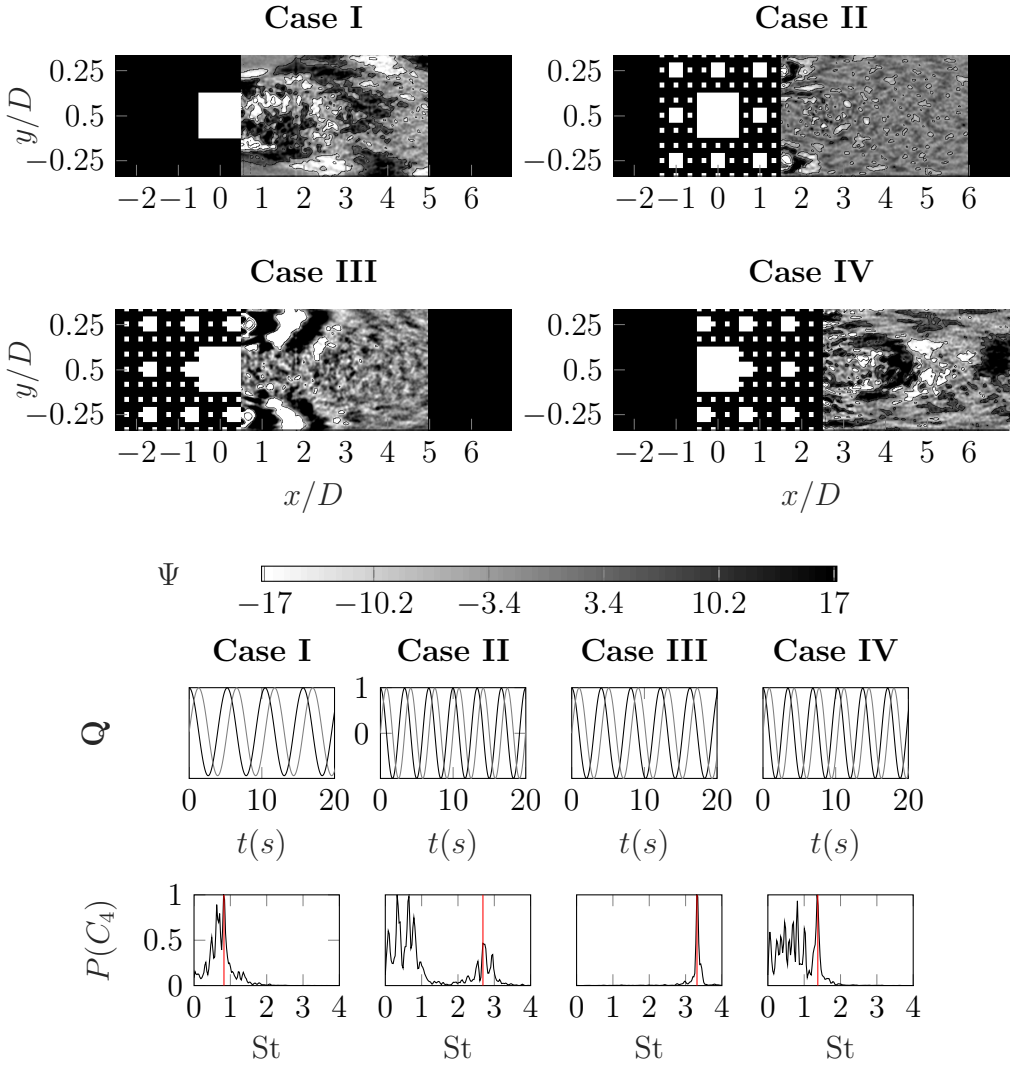

FIGURE 6.11: Top: The real component of the DMD modes $\mathbf{\Phi}$ where each extracted mode represents the peak frequencies highlighted in red. Middle: DMD temporal coefficients $\mathbf{Q}$, where the black line is the real part and the grey line is the imaginary part. Bottom: Fourier power spectrum of $\mathbf{C}_4$, with DMD spatial modes frequency highlighted in red.

6.4 Discussion

In case III, where there is no downstream obstruction, the change in the point of reattachment is very small compared to case I. As previously shown, an increase in the BR causes the point of reattachment to be retracted upstream. Whilst the confinement is causing the retraction of the reattachment, the upstream elements are causing the protraction, maybe as a consequence of a reduced drag on the largest cylinder caused by the upstream smaller ones (Igarashi 1997, Zhang et al. 2005). In case II, both the upstream and downstream region are obstructed. Since the reattachment length is increased, this suggests further effects caused by the downstream elements. It is not clear at this stage if this is due to drag modifications or due to enhanced advection speeds in the near field.

In all of the cases the smaller elements are positioned on either side of the large cylinder. As shown by Kumar & Vengadesan (2009) when a small square cylinder is positioned next to a large square cylinder, there is no effect on the shedding frequency associated to the largest one, but the frequency of vortex shedding associated to the smaller cylinder is increased. In case II & III, $\mathbf{\Phi}_4$ represents the spatial patterns of the flow structures associated to iteration II. As previously shown the unperturbed wake of a cylinder with a length scale of iteration II has a St=0.82. This frequency has been modified to St=2.8 and St = 3.4 for case II & III respectively. Since case III shows a clean peak in the Fourier spectrum of the coefficients, and the St has been increased, this could be linked to the observations to Kumar & Vengadesan (2009). A similar process could be taking place in case II, however from the broadband of frequencies present in the spectrum, and due to the lower spectral peak, the shift in St could be due to several processes.

In case III the larger scale wake is not obstructed by iterations II & III. This observation could offer an explanation for the increase of the energy contribution of $\mathbf{\Phi}_{3-14}$ in the POD spectra (see Fig. 6.6). Due to the size associated to iteration III, it is expected that any flow structure they might generate, has a small size and low energy, and as a consequence their signature should be difficult to identify in the region of measurement. Due to the different length scales of iteration II, and the lack of direct interaction with the wake of iteration I, it is expected to see flow structures generated by iteration II in the region of interest. Therefore, this could offer an explanation for the increase in energy in the spectra. This observation is in agreement with the fact that no important increase in energy was observed for case II & IV for $\mathbf{\Phi}_{3-14}$, however case II shows a slightly higher energy than case IV due to the fact that some structures do avoid the interaction with the wake of iteration I. As a result of the interaction of the wake generated by iteration I with the flow structures generated by the smaller cylinders, the break down of these flow structures might occur (no local interactions), thus an increase of the energy associated to higher order modes for case II & III is expected. A closer observation of Fig. 6.5 reveals that in-fact, for $\mathbf{\Phi}_{i<14}$, an increase of energy is developed. This increase of energy for $\mathbf{\Phi}_{i<14}$ is not developed in case III as a consequence of the ideas presented earlier. The validation of these observations requires measurements or numerical simulations within the porous media formed by all of the cylinders.

From the results the advantage of the use of DMD is also highlighted. From the POD the DMD allows the elucidation of spatio-temporal structures which are not revealed by the POD alone. This further promotes the benefits on the use of the DMD coupled with a POD search criteria, at least for the larger scales.

6.5 Chapter conclusions

Even though a characterisation of the flow within the channels formed between elements was not possible, the result clearly show that the interactions of iteration I with iterations II & III affect its wake properties. The results show the influence of the arrangement of obstacles on the sides of the cylinder, which modify the BR producing a clear change of the vortex shedding frequency and a reorganisation of the energy of the leading modes. This is further highlighted in the DMD modes where it is demonstrated there is a clear change in the spatial structures relating to the higher order dominant frequencies. The results also show the effect of the size of the perturbed region upstream and downstream of the cylinder. The influence can be observed on the magnitude of the peak of TKE. The larger the upstream region the higher the peak of TKE, however the lower the energy of the leading modes, the higher the energy of higher order modes. The larger the obstruction in the region downstream the cylinder, the longer the reattachment length. From the first four POD and DMD modes of all cases, it was possible to observe similar spatial patterns to those found in the unconfined and low Reynolds confined cylinder flows. This means that most of the issues caused by the introduction of the smaller cylinders are related to shedding frequencies and energy redistribution. From an environmental prospective these results show the layout of a city is related to the wake it produced. The understanding of this is important to understand the mixing of pollutants.

Chapter 7

Conclusions

In this thesis at the end of each chapter conclusions are made. These conclusions are summarised below:

1. Unavoidably, data collected using Particle Image Velocimetry, or other similar techniques, can contain outlier data points. Whilst it is possible to remove and replace these points manually, it is often not feasible, due to the large number of vector field typical to these methods. In the thesis a novel approach to remove and replace outliers using a correction of the temporal coefficients relating to a Proper Orthogonal Decomposition (POD) is proposed. Unlike previous POD based methods the method is non-iterative and as a consequence less computationally intensive. The presented method, (PODDEM), when benchmarked against state of the art methods, is found to be the most efficient in the detection of outliers and comparable in the accuracy of replacement.

2. In a simple flow case a POD is very effective in elucidating single turbulent structures. However, in a complex flow case, where the dynamics are

non-linear, the POD modes can become colluded with multiple structures. Although as a POD extracts modes which are spatially significant, the temporal coefficients relating to the modes contain information relating to the colluded structures. Therefore by taking a Fourier power spectrum of the temporal coefficients the frequencies relating to the individual structures are revealed. As a Dynamic Mode Decomposition (DMD) is temporally orthogonal, it is possible obtain spatial modes relating to these single frequencies, ergo determining turbulent structures which are spatially and temporally significant.

3. The topographical forcing caused by a lateral obstacle in a shallow flow generates a mixing layer, bounding a dual counter rotating recirculation cells. This mixing layer is characterised by the sudden change in the integral length scale of the vortical structures at the interface between the cells. The mechanism which leads to this sudden expansion is highly-non linear and comprised of multiple turbulent structures. Applying the method proposed in Chapter 4 it is possible to highlight the turbulent structures responsible for this sudden expansion. From a low-order DMD reconstruction it is possible to reveal the vortex merging process leading to the sudden change in the integral length scale.

4. By surrounding a confined square cylinder with smaller multi-scale elements and after a POD and DMD analysis, it is found it is possible to modify the properties of the developed wake. The size of upstream and downstream perturbed region, formed by the introduced elements, is related to the shedding frequency of the large square cylinder and to a redistribution of energy among the dominant modes. It is suggested that a modification of the spatial

layout of the surrounding elements is related to the position and magnitude of the turbulent kinetic energy.

7.1 Summary conclusions

The objective of this thesis was to demonstrate that modal decomposition techniques can be successfully applied in context of Civil Engineering. In this thesis it is demonstrated that not only are the temporal coefficients of a POD offer a means to remove outliers in data, but the frequencies obtained from a Fourier Power Spectrum of them also can be used as a search criteria for a DMD.

By applying the modal decompositions to two very different cases it is clear that both POD and DMD are techniques which are both under utilised in Civil Engineering applications. As this thesis has shown, these methods can be extremely effective in describing complex spatio-temporal mechanisms such as those leading to the enhanced mixing of pollutants, river scouring or vortex induced vibrations in the urban environment etc.

Appendix A

PODDEM mathematical reasoning and sensitivity analysis

A.1 Mathematical reasoning for PODDEM

The PODDEM is based on the fact that a spatio-temporal error structure in $\mathbf{W}$ is partitioned by the POD across a set of φ independent modes in the spatial domain N, such that the spatial error is found in $\mathbf{\Phi}$ and the temporal error in $\mathbf{A}$. To illustrate this, two instances of $\mathbf{W}$ are considered. In the first case the number of temporal measurements outweigh the number of spatial measurements, while in the second case the converse is true.

If the number of time measurements are larger than measurement locations, $\varphi \gg N$, such as in the case of point-wise velocimetry techniques, the components of the velocity signal are measured at a single spatial location. These instruments can be used individually or several sensors can be synchronised to perform simultaneous measurements at multiple locations. From a generic perspective, this situation

corresponds to the case of $\varphi \gg N$. In an idealised extreme situation, a velocity sensor can fail, introducing errors in that position at all times, i.e the signal may occur at any time, while always occurring at the same position in space. An error signal representing this case can be defined as follows:

$$\mathbf{W}^{(1)}(n \neq \eta, t) = 0, \tag{A.1}$$

$$\mathbf{W}^{(1)}(n = \eta, t) = 1, \tag{A.2}$$

where n is the spatial location within the locations N, and η is the position at which an outlier can be found at all times. The decomposition of the matrix representing these measurements leads to the following results: $\lambda_1^{(1)} = \sqrt{\varphi}$, $\mathbf{A}_1^{(1)} = -1/\sqrt{\varphi}$

$$\mathbf{\Phi}_1^{(1)} = \begin{cases} 0 & \text{if } (n \neq \eta), \\ -1 & \text{if } (n = \eta). \end{cases} \tag{A.3}$$

Since the error is the only source of change in the variance of the error signal, it can be expected that its signature will be found in the parameters characterising the leading mode. For a sufficiently large duration of the measurements, i.e for a large value of φ, $\lambda_1^{(1)}$ increases and therefore $\mathbf{A}_1^{(1)} \to 0$. Therefore, the error propagates into λ_1 and $\mathbf{\Phi}_1$.

As in the case of PIV measurements, in which the number of locations at which the velocity is measured, is normally larger than the number of time samples being analysed i.e. $N \gg \varphi$. If it is assumed that the outlier can be found everywhere in the space but at a single time instance, an idealised error signal can be defined as:

$$\mathbf{W}^{(2)}(n, t \neq \tau) = 0, \tag{A.4}$$

$$\mathbf{W}^{(2)}(n, t = \tau) = 1, \tag{A.5}$$

where τ is a temporal location at which all spatial locations within a snapshot contain outliers. Here, $\lambda_1^{(2)} = \sqrt{N}$, $\mathbf{\Phi}_1^{(2)} = -1/\sqrt{\varphi}$, and

$$\mathbf{A}_1^{(2)} = \begin{cases} 0 & \text{if } (t \neq \tau), \\ -1 & \text{if } (t = \tau). \end{cases} \tag{A.6}$$

For a sufficiently large number of spatial positions, $\lambda_1^{(2)}$ increases and therefore $\mathbf{\Phi_1}^2 \to 0$. Analogously to the previous case, this means the error can be found propagated in $\lambda_1^{(2)}$ and $\mathbf{A}_1^{(2)}$. Therefore, for PIV data, using the temporal coefficients to detect and replace data seems most logical.

A.2 Sensitivity Analysis

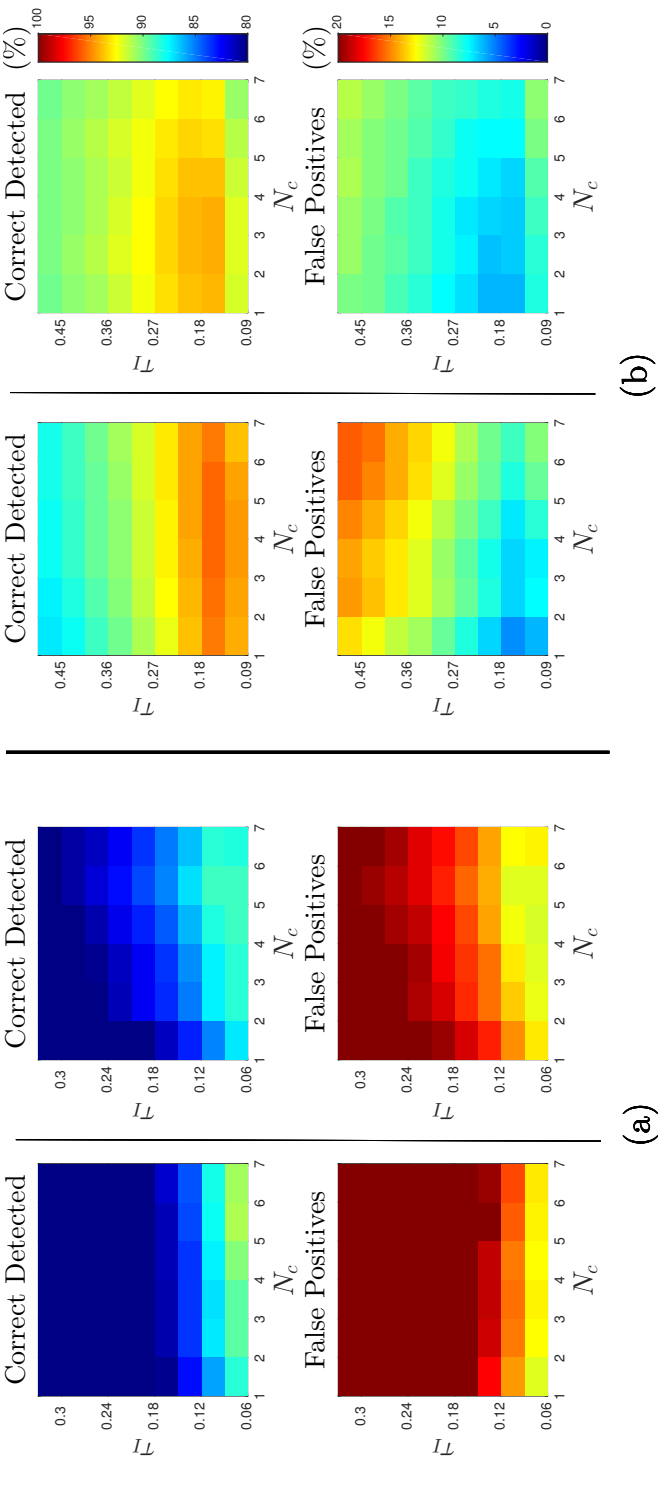

FIGURE A.1: Sensitivity analysis of kernel sizes used in moving average step of the PODDEM, where τ_I is the kernel size based on the average integral time scale. The top row shows the percentage of correct outliers detected. The bottom row shows the percentage of false outliers detected. (a) Results for channel flow. (b) Results for isotropic case.

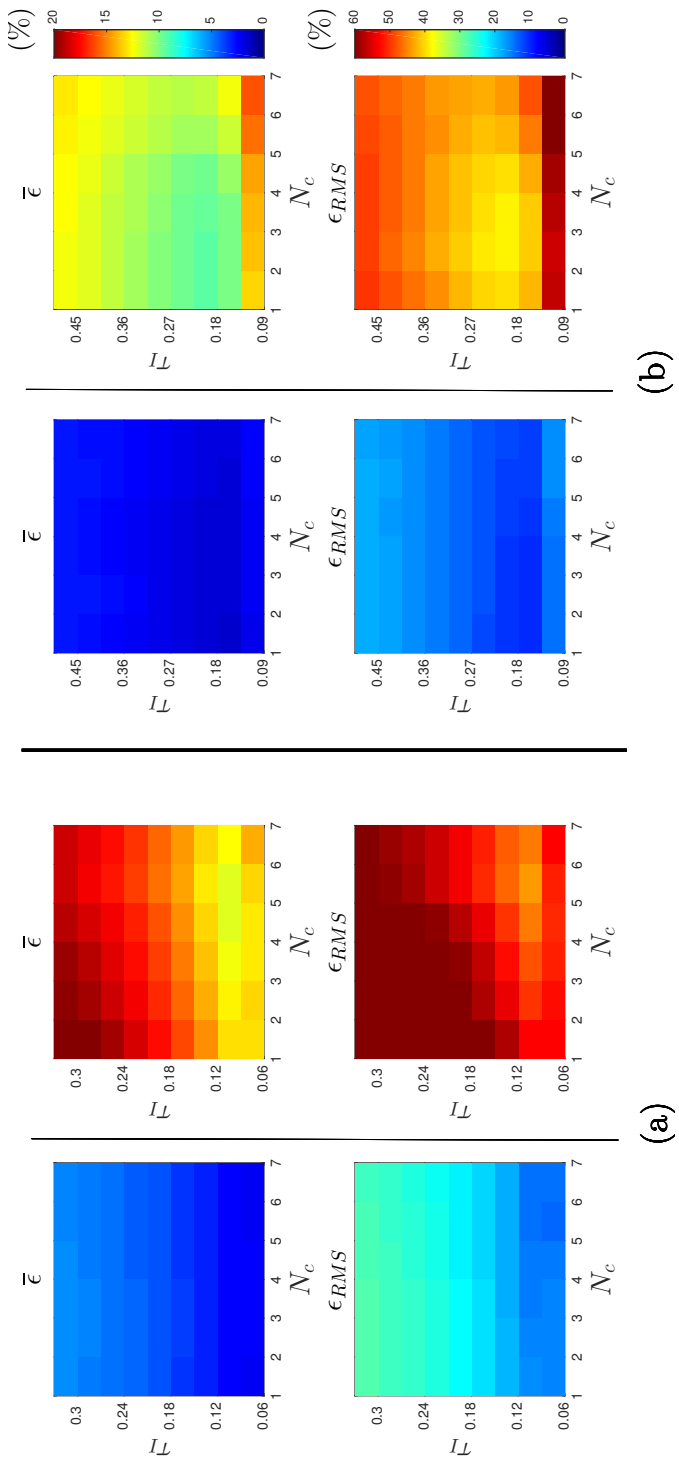

FIGURE A.2: Sensitivity analysis of kernel sizes used in moving average step of the PODDEM, where τ_I is the kernel size based on the average integral time scale. The top row shows $\bar{\epsilon}$ (accuracy) and bottom rows show the spatio-temporal ϵ_{RMS} (precision) error. (a) shows the error obtained with the contaminated channel case. (b) shows the results for the isotropic case.

Appendix B

PODDEM MATLAB script

```
ffunction [U V W]=poddem(a,b,c,d,e,f);

% The PODDEM function is the same method as published in:
% Higham, J. E., W. Brevis, and C. J. Keylock.
% "A rapid non-iterative proper orthogonal decomposition
% based outlier detection and correction for PIV data."
% Measurement Science and Technology 27.12 (2016): 125303.
%
% Please email jonny.e.higham(at)gmail.com if you have any
% questions.
%
% PODDEM is an acronym of "Proper Orthogonal Decompositon
% Dectection and Estimation Method", and is currently the
% most effective rapid method of detecting an estimating
% outlier in Particle Image Velocimetry data.
%
% Please note each input is to be input as a 3D matrix.
% where U = X x Y x T; where U is the velocity component
```

```
% and X and Y are spatial dimensions and T is the temporal
% dimension.
%
% This method can support up to three dimensions
%
% Quick usage: (Default values).
% [U]=poddem(U,thr,[],[],[]);
% [U,V]=poddem(U,V,[],[],[]);
% [U,V,V]=poddem(U,V,W,[],[],[]);
%
% "thr" is the threshold number between 0 and 1.
% The default is set to 0.05
% this number relates to 5% of outliers within the data.
%
% "ker" is the size of the kernal used in the smoothening
% of the coefficients this is set as default at 10.
%
% "fil", this can either be set to 'lin' or 'poddem',
% default is set to 'lin' this is optimum for small outliers.
% For larger outliers choose 'poddem'.
%
% Usage in 1D [U]=poddem(U,thr,ker,fill)
% Default values [U]=poddem(U,[],[],[])
%
% Usage in 2D [U,V]=poddem(U,V,thr,ker,fill)
% Default values [U,V]=poddem(U,V,[],[],[])
%
% Usage in 3D [U,V,W]=poddem(U,V,W,thr,ker,fill)
% Default values [U,V,W]=poddem(U,V,W,[],[],[])
%
%
```

```
% At this point we create the matrix to put into the SVD,
% we use all of the components here.
%
% Example:
% [U,V,W]=poddem(U,V,W,0.05,10,'lin')
%
%
% Please note this is programmed in my own unique way of
% programming, I know there will be more efficient ways,
% feel free to implement if you want.


if nargin == 4
    U = a; thr=b; ker=c; fill=d;
    tmp=reshape(U,size(U,1)*size(U,2),size(U,3));
elseif nargin ==5
    U = a; V=b; thr=c; ker=d; fill=e;
    tmp=[reshape(U,size(U,1)*size(U,2),size(U,3));
         reshape(V,size(V,1)*size(V,2),size(V,3))];
elseif nargin ==6
    U = a; V=b; W=c; thr=d; ker=e; fill=f;
    tmp=[reshape(U,size(U,1)*size(U,2),size(U,3));
         reshape(V,size(V,1)*size(V,2),size(V,3));
         reshape(W,size(W,1)*size(W,2),size(W,3))];

else
    error('Error: Greater than three dimensions')
end

if exist('V');
    if length(U(:))~=length(V(:));
```

```
        error('All of the data must be the same size');
    end
end

if exist('W');
    if length(U(:))~=length(V(:)) & length(U(:))~=length(W(:));
        error('All of the data must be the same size');
    end
end

if isempty(ker)==1;ker = 10;end
if isempty(thr)==1;thr = 0.05;end
if isempty(fill)==1;fill = 'lin';end

% Next we calculate the SVD (this is economy size to
% speed up the calculation)

[phi, s, a]=svd(tmp,'econ');

% Some times the SVD function flips the temporal
% coeficients, I don't know why but here there is a
% sanity check. We also pad the array here in order
% to remove outliers at the beginning and the end.

an=a;
for loop = 1:size(a,1);
    tmp=smooth(padarray(an(loop,:),[0,5*ker],'symmetric'),ker);
    an(loop,:)=tmp(5*ker+1:end-5*ker);
end
% we now produce a new matrix with the smoothed coefficient
recon=phi*s*an';
```

```
% here we reshape the data back into its original form
try
    rec_u=reshape(recon(1:size(U,1)*size(U,2),:)...
        ,size(U,1),size(U,2),size(U,3));
    tmp_u=(abs(U(:,:,:)-rec_u(:,:,:)));
    rec_v=reshape(recon(size(V,1)*...
        size(V,2)+1:2*size(V,1)*size(V,2),:)...
        ,size(V,1),size(V,2),size(V,3));
    tmp_v=(abs(V(:,:,:)-rec_v(:,:,:)));
    rec_w=reshape(2*recon(size(W,1)...
        *size(W,2)+1:3*size(W,1)*size(W,2),:)...
        ,size(W,1),size(W,2),size(W,3));
        tmp_u=(abs(U(:,:,:)-rec_u(:,:,:)));
    tmp_w=(abs(W(:,:,:)-rec_w(:,:,:)));
end

% At this point we create the mask which is used to
% detect the outliers,this is done using this while loop,
% whilst this isnt the most efficient
% way I have found it to be the most effective.
mask=zeros(size(U));
tmp=1.1;inc=0.0;
while tmp>thr;
    mask=zeros(size(U));
    inc=inc+.01;
        thr_u=inc*std(tmp_u(:));
        mask(tmp_u>thr_u)=1;
    try
        thr_v=inc*std(tmp_v(:));
        mask(tmp_v>thr_v)=1;
    end
```

```
    try
        thr_w=inc*std(tmp_w(:));
        mask(tmp_w>thr_w)=1;
    end
    tmp=(sum(mask(:)))./length(mask(:));
    mask_nans=zeros(size(mask));
    mask_nans(mask==1)=nan;
end
try
    U=(U.*(1-mask)+(mask.*(rec_u)));
    V=(V.*(1-mask)+(mask.*(rec_v)));
    W=(W.*(1-mask)+(mask.*(rec_w)));
end
try
    U(U>nanmean(U(:))+1*nanstd(U(:))&mask==1)=nan;
    U(U<nanmean(U(:))-1*nanstd(U(:))&mask==1)=nan;
    V(V>nanmean(V(:))+1*nanstd(V(:))&mask==1)=nan;
    V(V<nanmean(V(:))-1*nanstd(V(:))&mask==1)=nan;
    W(W>nanmean(W(:))+1*nanstd(V(:))&mask==1)=nan;
    W(W<nanmean(W(:))-1*nanstd(V(:))&mask==1)=nan;
end

% At this point we can do two steps, we can either use
% a linear interpolant, or we can use the poddem hole
% filling. As shown the publication, if one is filling
% larger holes in the data PODDEM is more accurate and
% precise, however for smaller gaps a linear interpolant
% is better. Here I use inpaint_nans see below:

[X, Y]=meshgrid(1:size(U,2),1:size(U,1));
if strcmp(fill,'lin')==1
```

```
    for loop = 1:size(U,3)
        try
            U(:,:,loop)=inpaint_nans(U(:,:,loop),1);
            V(:,:,loop)=inpaint_nans(V(:,:,loop),1);
            W(:,:,loop)=inpaint_nans(W(:,:,loop),1);
        end
    end
elseif strcmp(fill,'poddem')==1
    %this is the poddem fill mode
    try
        U(isnan(U))=0;
        U = U+rec_u.*mask;
        V(isnan(V))=0;
        V = V+rec_v.*mask;
        W(isnan(W))=0;
        W = W+rec_w.*mask;
    end
end
```

Appendix C

POD-DMD integration discussion

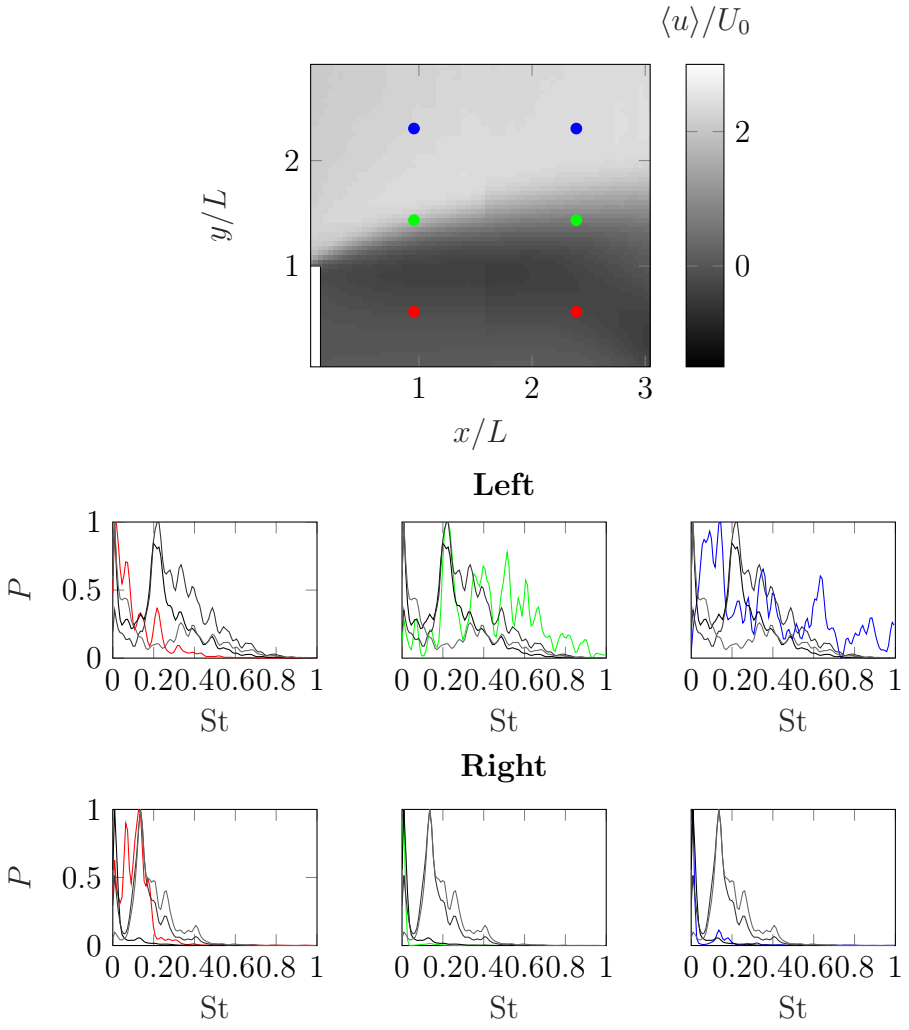

FIGURE C.1: Comparison of the Fourier power spectra of the top three POD coefficients and chosen points in the velocity field. In the top row the mean streamwise velocity field is presented with 6 chosen points highlighted. In the middle and bottom rows the Fourier power spectra of the top three POD coefficients and the spectra of the highlighted points are plotted. Where C_1 - black line, C_2 - grey line and C_3 - light grey line, and the middle and bottom row correspond to the highlighted left and right columns respectively.

Appendix D

POD-DMD integration MATLAB script

```
clear;clf;
freq = 5; %Hz; aquisition frequency
% Transform the data into column vectors.
data=[reshape(u,size(u,1)*size(u,2),size(u,3));
        reshape(v,size(u,1)*size(u,2),size(u,3))];
% Perform the POD.
[Phi ,~, C]=svd(data-repmat(mean(data,2),[1 size(data,2)]),'econ');
% Plot the figures
figure(1)
subplot(4,1,1)
mode=2; % POD mode to be plotted
imagesc(reshape(Phi(1:size(u,1)*size(u,2),mode)...
    ,size(u,1),size(u,2)))
title(['\Phi',sprintf('_%i (u-component)',mode)])
subplot(4,1,2)
```

```
imagesc(reshape(Phi(size(v,1)*size(v,2)+1:end,mode)...
    ,size(v,1),size(v,2)))
title(['\Phi',sprintf('_%i (v-component)',mode)])
subplot(4,1,3)
plot(C(:,mode))
title(sprintf('C_%i',mode))
subplot(4,1,4)
[px, fx]=pwelch(C(:,mode),round(0.9*size(u,3)),...
    round(0.8*size(u,3)),2^12,freq);
plot(fx,px);
title(sprintf('P(C_%i)',mode))
%DMD Calculations
[Phi,S,C]=svd(data(:,1:end-1),'econ');
F=(Phi'*data(:,2:end)*C)/S;
[M,Z]=eig(F) ;% Compute eigen values and vectors
Q=zeros(size(F));
for loop1=1:679;
    Q(:,loop1)=diag(Z).^(loop1-1);
    %creating vandermonde with increasing powers
end
% Compute the modes
Psi=data(:,1:end-1)*Q';
% Compute the frequencies
f=freq*angle(diag(Z))./(2*pi);
% Find the matching frequency from POD
[~,l]=max(px);
[~,l]=min(abs(fx(l)-f));
% Plot the DMD modes;
figure(2);
subplot(4,1,1)
imagesc(real(reshape(Psi(1:size(u,1)*size(u,2),l)...
```

```
    ,size(u,1),size(u,2))))
title(['\Psi',sprintf('_{f=%0.2f Hz} (u-component)',f(l))])
subplot(4,1,2)
imagesc(real(reshape(Psi(size(v,1)*size(v,2)+1:end,l)...
    ,size(v,1),size(v,2))))
title(['\Psi',sprintf('_{f=%0.2f Hz} (v-component)',f(l))])
subplot(4,1,3)
plot(real(Q(l,:)))
title(['Q',sprintf('_{f=%0.2f Hz}',f(l))])
subplot(4,1,4)
[px, fx]=pwelch(real(Q(l,:)),...
round(0.9*size(u,3)),round(0.8*size(u,3)),2^12,freq);
plot(fx,px);
title(['P(Q',sprintf('_{f=%0.2f Hz})',f(l))])
```

Bibliography

Adrian, R., Christensen, K. & Liu, Z.-C. (2000), 'Analysis and interpretation of instantaneous turbulent velocity fields', *Experiments in fluids* **29**(3), 275–290.

Adrian, R. J. (2007), 'Hairpin vortex organization in wall turbulence a', *Physics of Fluids* **19**(4), 041301.

Adrian, R. J. & Marusic, I. (2012), 'Coherent structures in flow over hydraulic engineering surfaces', *Journal of Hydraulic Research* **50**(5), 451–464.

Ahmed, H. S., Hasan, M. M. & Tanaka, N. (2010), 'Analysis of flow around impermeable groynes on one side of symmetrical compound channel: An experimental study', *Water Science and Engineering* **3**(1), 56–66.

Armaly, B. F., Durst, F., Pereira, J. & Schönung, B. (1983), 'Experimental and theoretical investigation of backward-facing step flow', *Journal of Fluid Mechanics* **127**, 473–496.

Aubry, N. (1991), 'On the hidden beauty of the proper orthogonal decomposition', *Theoretical and Computational Fluid Dynamics* **2**(5-6), 339–352.

Batchelor, G. K. (1969), 'Computation of the energy spectrum in homogeneous two-dimensional turbulence', *Physics of Fluids (1958-1988)* **12**(12), II–233.

Batham, J. (1973), 'Pressure distributions on circular cylinders at critical reynolds numbers', *Journal of Fluid Mechanics* **57**(02), 209–228.

Batty, M. & Longley, P. A. (1994), *Fractal cities: A geometry of form and function*, Academic Press.

Bearman, P. (1967), 'The effect of base bleed on the flow behind a two-dimensional model with a blunt trailing edge (base bleed effects on flow behind two-dimensional model with blunt trailing edge, measuring base pressure, shedding frequency and vortex formation)', *Aeronautical Quarterly* **18**, 207–224.

Bearman, P. & Trueman, D. (1972), 'An investigation of the flow around rectangular cylinders', *Aeronautical Quarterly* **23**(03), 229–237.

Belchov, R. & Yaglom, A. (1971), 'Comments on the theory of similarity as applied to turbulence in an unstably stratified fluid', *Atmospheric Oceanic Physics* **7**, B2932.

Berkooz, G., Holmes, P. & Lumley, J. L. (1993*a*), 'The proper orthogonal decomposition in the analysis of turbulent flows', *Annual review of fluid mechanics* **25**(1), 539–575.

Berkooz, G., Holmes, P. & Lumley, J. L. (1993*b*), 'The Proper Orthogonal Decomposition in the analysis of turbulent flows', *Annual Review Fluid Mechanics* **25**(1), 539–575.

Boyer, C., Roy, A. G. & Best, J. L. (2006), 'Dynamics of a river channel confluence with discordant beds: Flow turbulence, bed load sediment transport, and bed morphology', *Journal of Geophysical Research: Earth Surface* **111**(F4).

Brevis, W. & García-Villalba, M. (2011), 'Shallow-flow visualization analysis by proper orthogonal decomposition', *Journal of Hydraulic Research* **49**(5), 586–594.

Brevis, W., García-Villalba, M. & Niño, Y. (2014), 'Experimental and large eddy simulation study of the flow developed by a sequence of lateral obstacles', *Environmental Fluid Mechanics* pp. 1–21.

Chakraborty, P., Balachandar, S. & Adrian, R. J. (2005), 'On the relationships between local vortex identification schemes', *Journal of Fluid Mechanics* **535**, 189–214.

Chen, D. & Jirka, G. H. (1997), 'Absolute and convective instabilities of plane turbulent wakes in a shallow water layer', *Journal of Fluid Mechanics* **338**, 157–172.

Chen, Y. J. & Shao, C. P. (2013), 'Suppression of vortex shedding from a rectangular cylinder at low Reynolds numbers', *Journal of Fluids and Structures* **43**, 15–27.

Cheng, Z. & Constantinescu, G. (2014), 'Spatial development of a constant-depth shallow mixing layer in a long channel', *River Flow 2014* p. 155.

Chrisohoides, A., Sotiropoulos, F. & Sturm, T. W. (2003), 'Coherent structures in flat-bed abutment flow: Computational fluid dynamics simulations and experiments', *Journal of Hydraulic Engineering* **129**(3), 177–186.

Chu, V. H. & Babarutsi, S. (1988), 'Confinement and bed-friction effects in shallow turbulent mixing layers', *Journal of Hydraulic Engineering* **114**(10), 1257–1274.

Constantinescu, G., Sukhodolov, A. & McCoy, A. (2009), 'Mass exchange in a shallow channel flow with a series of groynes: LES study and comparison with laboratory and field experiments', *Environmental fluid mechanics* **9**(6), 587–615.

da Vinci, L., Richter, J. P., Richter, I. A. & Bell, M. R. (1970), *The literary works of Leonardo da Vinci*, Vol. 1, Phaidon London.

Davis, R., Moore, E. & Purtell, L. (1984), 'A numerical-experimental study of confined flow around rectangular cylinders', *Physics of Fluids* **27**(1), 46–59.

Duan, J. G., He, L., Fu, X. & Wang, Q. (2009), 'Mean flow and turbulence around experimental spur dike', *Advances in Water Resources* **32**(12), 1717–1725.

Durao, D., Heitor, M. & Pereira, J. (1988), 'Measurements of turbulent and periodic flows around a square cross-section cylinder', *Experiments in Fluids* **6**(5), 298–304.

Dutta, S., Muralidhar, K. & Panigrahi, P. (2003), 'Influence of the orientation of a square cylinder on the wake properties', *Experiments in Fluids* **34**(1), 16–23.

Everson, R. & Sirovich, L. (1995), 'Karhunen – Loève procedure for gappy data', *Journal of the Optical Society of America* **12**(8), 1657–1664.

Francis, J., Pattanaik, A. & Wearne, S. (1968), 'Technical note. observations of flow patterns around some simplified groyne structures in channels.', *Proceedings of the Institution of Civil Engineers* **41**(4), 829–837.

Frisch, U. & Donnelly, R. J. (1996), 'Turbulence: the legacy of an kolmogorov'.

Gao, Y., Yu, D., Tan, S., Wang, X. & Hao, Z. (2010), 'Experimental study on the near wake behind two side-by-side cylinders of unequal diameters', *Fluid dynamics research* **42**(5), 055509.

Garcia, D. (2010), 'Robust smoothing of gridded data in one and higher dimensions with missing values', *Computational Statistics & Data Analysis* **54**(4), 1167–1178.

Garcia, D. (2011), 'A fast all-in-one method for automated post-processing of PIV data', *Experiments in Fluids* **50**(5), 1247–1259.

Garde, R., Subramanya, K. & Nambudripad, K. (1961), 'Study of scour around spur-dikes', *Journal of the Hydraulics Division* **86**, 23–37.

Gerrard, J. (1966), 'The mechanics of the formation region of vortices behind bluff bodies', *Journal of Fluid Mechanics* **25**(02), 401–413.

Golub, G. H. & Reinsch, C. (1970), 'Singular value decomposition and least squares solutions', *Numerische mathematik* **14**(5), 403–420.

Goring, D. & Nikora, I. (2002), 'Despiking acoustic doppler velocimeter data', *Journal of Hydraulic Engineering* **128**, 117–126.

Graham, J., Kanov, K., Yang, X., Lee, M., Malaya, N., Lalescu, C., Burns, R., Eyink, G., Szalay, A., Moser, R. et al. (2016), 'A web services accessible database of turbulent channel flow and its use for testing a new integral wall model for LES', *Journal of Turbulence* **17**(2), 181–215.

Green, M. A., Rowley, C. W. & Haller, G. (2007), 'Detection of lagrangian coherent structures in three-dimensional turbulence', *Journal of Fluid Mechanics* **572**, 111–120.

Grift, R., Buijse, A., Van Densen, W., Machiels, M., Kranenbarg, J., Klein Breteler, J. & Backx, J. (2003), 'Suitable habitats for 0-group fish in rehabilitated floodplains along the lower River Rhine', *River Research and Applications* **19**(4), 353–374.

Gunes, H., Sirisup, S. & Karniadakis, G. E. (2006), 'Gappy data: To Krig or not to Krig?', *Journal Computational Physics* **212**, 358–382.

Hain, R. & Kähler, C. (2007), 'Fundamentals of multi-frame Particle Image Velocimetry (PIV)', *Experiments in Fluids* **42**(4), 575–587.

Higham, J., Brevis, W. & Keylock, C. (2016), 'A rapid non-iterative proper orthogonal decomposition based outlier detection and correction for PIV data', *Measurement Science and Technology* **27**(12), 125303.

Huang, H., Dabiri, D. & Gharib, M. (1997), 'On errors of digital particle image velocimetry', *Measurement Science and Technology* **8**(12), 1427.

Huber, A. (1988), 'Video images of smoke dispersion in the near wake of a model duilding. part i. temporal and spatial scales of vortex shedding', *Journal of Wind Engineering and Industrial Aerodynamics* **31**(2-3), 189–224.

Huber, A. H., Arya, S. P., Rajala, S. A. & Borek, J. W. (1991), 'Preliminary studies of video images of smoke dispersion in the near wake of a model building', *Atmospheric Environment. Part A. General Topics* **25**(7), 1199–1209.

Hunt, J. C., Wray, A. & Moin, P. (1988), Eddies, streams, and convergence zones in turbulent flows, *in* 'Studying Turbulence Using Numerical Simulation Databases, 2', Vol. 1, pp. 193–208.

Hussain, A. & Clark, A. (1981), 'On the coherent structure of the axisymmetric mixing layer: a flow-visualization study', *Journal of Fluid Mechanics* **104**, 263–294.

Hussain, A. F. (1983), 'Coherent structures—reality and myth', *Physics of Fluids (1958-1988)* **26**(10), 2816–2850.

Igarashi, T. (1997), 'Drag reduction of a square prism by flow control using a small rod', *Journal of Wind Engineering and Industrial Aerodynamics* **69**, 141–153.

Islam, S.-u., Shigri, S. H., Ying, Z. C., Akbar, T. & Majeed, D. (2017), 'A computational study of flow past three unequal sized square cylinders at different positions', *AIP Advances* **7**(3), 035303.

Jeong, J. & Hussain, F. (1995), 'On the identification of a vortex', *Journal of Fluid Mechanics* **285**, 69–94.

Jirka, G. H. (2001), 'Large scale flow structures and mixing processes in shallow flows', *Journal of Hydraulic Research* **39**(6), 567–573.

Jirka, Gerhard H, U. W. S. (2004), 'Shallow flows: a definition', *Shallow flows* pp. 3–11.

Jovanović, M. R., Schmid, P. J. & Nichols, J. W. (2014), 'Sparsity-promoting dynamic mode decomposition', *Physics of Fluids (1994-present)* **26**(2), 024103.

Kadota, A. & Suzuki, K. (2010), Mean flow structure and advection of instantaneous coherent-flow pattern around t-type and l-type groynes, *in* 'Environmental Hydraulics, Two Volume Set: Proceedings of the 6th International Symposium on Enviornmental Hydraulics, Athens, Greece, 23-25 June 2010', CRC Press, p. 81.

Karhunen, K. (1946), 'Zur spektral theorie stochastischer prozesse', *Annales Academiæ Scientiarum Fennicæ* **A1:34**.

Koken, M. (2011), 'Coherent structures around isolated spur dikes at various approach flow angles', *Journal of Hydraulic Research* **49**(6), 736–743.

Koken, M. & Constantinescu, G. (2008), 'An investigation of the flow and scour mechanisms around isolated spur dikes in a shallow open channel: 1. conditions corresponding to the initiation of the erosion and deposition process', *Water Resources Research* **44**(8).

Koken, M. & Constantinescu, G. (2009), 'An investigation of the dynamics of coherent structures in a turbulent channel flow with a vertical sidewall obstruction', *Physics of Fluids (1994-present)* **21**(8), 085104.

Kolar, V., Lyn, D. & Rodi, W. (1997), 'Ensemble-averaged measurements in the turbulent near wake of two side-by-side square cylinders', *Journal of Fluid Mechanics* **346**, 201–237.

Kolmogorov, A. N. (1941), The local structure of turbulence in incompressible viscous fluid for very large Reynolds numbers, *in* 'Dokl. Akad. Nauk SSSR', Vol. 30, pp. 299–303.

Kolmogorov, A. N. (1962), 'A refinement of previous hypotheses concerning the local structure of turbulence in a viscous incompressible fluid at high reynolds number', *Journal of Fluid Mechanics* **13**(01), 82–85.

Kosambi, D. (1943), 'Statistics in function space', *Journal of the Indian Mathematical Society (New Series)* **7**(1), 76–88.

Kraichnan, R. H. (1967), Inertial ranges in two-dimensional turbulence, Technical report, DTIC Document.

Kuhnle, R. A., Alonso, C. V. & Shields, F. D. (1999), 'Geometry of scour holes associated with 90 spur dikes', *Journal of Hydraulic Engineering* **125**(9), 972–978.

Kumar, M. S. & Vengadesan, S. (2009), 'Large eddy simulations of flow interference between two unequal sized square cylinders', *International Journal of Computational Fluid Dynamics* **23**(10), 671–686.

Le Coz, J., Brevis, W., Niño, Y., Paquier, A. & Riviére, N. (2006), Open-channel side-cavities: A comparison of field and flume experiments, *in* 'River Flow 2006, Two Volume Set: Proceedings of the International Conference on Fluvial Hydraulics, Lisbon, Portugal, 6-8 September 2006', CRC Press, p. 145.

Lee, B. (1975), 'The effect of turbulence on the surface pressure field of a square prism', *Journal of Fluid Mechanics* **69**(02), 263–282.

Li, Y., Perlman, E., Wan, M., Yang, Y., Meneveau, C., Burns, R., Chen, S., Szalay, A. & Eyink, G. (2008), 'A public turbulence database cluster and applications to study Lagrangian evolution of velocity increments in turbulence', *Journal of Turbulence* (9), N31.

Liang, D., Jiang, C. & Li, Y. (2003), 'Cellular neural network to detect spurious vectors in PIV data', *Experiments in Fluids* **34**(1), 52–62.

Lin, J.-C., Yang, Y. & Rockwell, D. (2002), 'Flow past two cylinders in tandem: instantaneous and averaged flow structure', *Journal of Fluids and Structures* **16**(8), 1059–1071.

Liu, C.-H. & Chen, J. M. (2002), 'Observations of hysteresis in flow around two square cylinders in a tandem arrangement', *Journal of Wind Engineering and Industrial Aerodynamics* **90**(9), 1019–1050.

Loève, M. (1945), 'Functions aléatoire de second ordre.', *Comptes Rendus de l'Académie des Sciences* **220**.

Lumley, J., Holmes, P. & Berkooz, G. (1996), 'Turbulence, coherent structures', *Dynamical Systems and Symmetry, Cambridge University Press* .

Ly, H. V. & Tran, H. T. (2001), 'Modeling and control of physical processes using proper orthogonal decomposition', *Mathematical and computer modelling* **33**(1-3), 223–236.

Masullo, A. & Theunissen, R. (2016), 'Adaptive vector validation in image velocimetry to minimise the influence of outlier clusters', *Experiments in Fluids* **57**(3), 1–21.

Meyer, K. E., Pedersen, J. M. & Özcan, O. (2007), 'A turbulent jet in crossflow analysed with proper orthogonal decomposition', *Journal of Fluid Mechanics* **583**, 199–227.

Mezić, I. (2005), 'Spectral properties of dynamical systems, model reduction and decompositions', *Nonlinear Dynamics* **41**(1-3), 309–325.

Mukhopadhyay, A., Biswas, G. & Sundararajan, T. (1992), 'Numerical investigation of confined wakes behind a square cylinder in a channel', *International Journal for Numerical Methods in Fluids* **14**(12), 1473–1484.

Nadaoka, K. & Yagi, H. (1998), 'Shallow-water turbulence modeling and horizontal large-eddy computation of river flow', *Journal of Hydraulic Engineering* **124**(5), 493–500.

Nicolle, A. & Eames, I. (2011), 'Numerical study of flow through and around a circular array of cylinders', *Journal of Fluid Mechanics* **679**, 1–31.

Nielsen, H., Lophaven, S. & Søndergaard, J. (2002), 'DACE - a MATLAB Kriging toolbox'.

Obukbov, A. M. (1954), 'Statistical description of continuous fields.', *Trudy Geofizicheskogo Instituta, Akademiya Nauk SSSR* **24**, 3–42.

Okajima, A. (1982), 'Strouhal numbers of rectangular cylinders', *Journal of Fluid Mechanics* **123**, 379–398.

Paik, J. & Sotiropoulos, F. (2005), 'Coherent structure dynamics upstream of a long rectangular block at the side of a large aspect ratio channel', *Physics of Fluids (1994-present)* **17**(11), 115104.

Pougachev, V. S. (1953), 'General theory of the correlations of random functions.', *Izvestiya Akademii Nauk SSSR. Seriya Matematicheskaya. Bulletin de l'Académie des Sciences de l'URSS* .

Raben, S. G., Charonko, J. J. & Vlachos, P. P. (2012), 'Adaptive Gappy Proper Orthogonal Decomposition for Particle Image Velocimetry data reconstruction', *Measurement Science and Technology* **23**(2), 025303.

Rehimi, F., Aloui, F., Nasrallah, S. B., Doubliez, L. & Legrand, J. (2008), 'Experimental investigation of a confined flow downstream of a circular cylinder centred between two parallel walls', *Journal of Fluids and Structures* **24**(6), 855–882.

Rempfer, D. & Fasel, H. F. (1994), 'Evolution of three-dimensional coherent structures in a flat-plate boundary layer', *Journal of Fluid Mechanics* **260**, 351–375.

Reynolds, O. (1883), 'An experimental investigation of the circumstances which determine whether the motion of water shall be direct or sinuous, and of the

law of resistance in parallel channels.', *Proceedings of the Royal Society of London* **35**(224-226), 84–99.

Reynolds, O. (1885), 'On the dilatancy of media composed of rigid particles in contact. with experimental illustrations', *The London, Edinburgh, and Dublin Philosophical Magazine and Journal of Science* **20**(127), 469–481.

Rhoads, B. L. & Sukhodolov, A. N. (2004), 'Spatial and temporal structure of shear layer turbulence at a stream confluence', *Water Resources Research* **40**(6).

Richardson, L. F. (1922), 'Weather prediction by numerical process'.

Richter, A. & Naudascher, E. (1976), 'Fluctuating forces on a rigid circular cylinder in confined flow', *Journal of Fluid Mechanics* **78**(03), 561–576.

Rowley, C. W., Mezić, I., Bagheri, S., Schlatter, P. & Henningson, D. S. (2009), 'Spectral analysis of nonlinear flows', *Journal of Fluid Mechanics* **641**, 115–127.

Ruhe, A. (1984), 'Rational Krylov sequence methods for eigenvalue computation', *Linear Algebra and its Applications* **58**, 391–405.

Safarzadeh, A. & Brevis, W. (2016), 'Assessment of 3d-RANS models for the simulation of topographically forced shallow flows', *Journal of Hydrology and Hydromechanics* **64**(1), 83–90.

Safarzadeh, A., Salehi Neyshabouri, S. A. A. & Zarrati, A. R. (2016), 'Experimental investigation on 3d turbulent flow around straight and t-shaped groynes in a flat bed channel', *Journal of Hydraulic Engineering* p. 04016021.

Scarano, F. (2002), 'Iterative image deformation methods in PIV', *Measurement Science and Technology* **13**(1), R1.

Scarano, F. (2012), 'Tomographic PIV: Principles and practice', *Measurement Science and Technology* **24**(1), 012001.

Schmid, P. J. (2010), 'Dynamic mode decomposition of numerical and experimental data', *Journal of Fluid Mechanics* **656**, 5–28.

Schmid, P. J. (2011), 'Application of the dynamic mode decomposition to experimental data', *Experiments in fluids* **50**(4), 1123–1130.

Schmid, P. J., Meyer, K. E. & Pust, O. (2009), Dynamic Mode Decomposition and Proper Orthogonal Decomposition of flow in a lid-driven cylindrical cavity, *in* '8th international symposium on Particle Image Velocimetry-PIV09', number 3, pp. 1–4.

Shinneeb, A., Bugg, J. & Balachandar, R. (2004), 'Variable threshold outlier identification in PIV data', *Measurement Science and Technology* **15**(9), 1722.

Sierpinski, W. (1916), 'Sur une courbe cantorienne qui contient une image biunivoque et continue de toute courbe donnée', *Comptes Rendus* **629**.

Smagorinsky, J. (1963), 'General circulation experiments with the primitive equations: I. the basic experiment', *Monthly Weather Review* **91**(3), 99–164.

Socolofsky, S. A. & Jirka, G. H. (2004), 'Large-scale flow structures and stability in shallow flows', *Journal of Environmental Engineering and Science* **3**(5), 451–462.

Sommerfeld, A. (1908), 'Ein beitrag zur hydrodynamischen erklaerung der turbulenten fluessigkeitsbewegungen', *Atti del IV Congresso internazionale dei matematici* **4**, 116–124.

Stokes, G. G. (1851), *On the effect of the internal friction of fluids on the motion of pendulums*, Vol. 9, Pittsburgh Press.

Sukhodolov, A. N. & Rhoads, B. L. (2001), 'Field investigation of three-dimensional flow structure at stream confluences: 2. turbulence', *Water Resources Research* **37**(9), 2411–2424.

Talstra, H. (2011), *Large-scale turbulence structures in shallow separating flows*, TU Delft, Delft University of Technology.

Talstra, H., Uijttewaal, W. S. & Stelling, G. S. (2006), Emergence of large-scale coherent structures in a shallow separating flow, *in* 'Conference proceedings of River Flow 2006, International Conference on Fluvial Hydraulics, Lisboa', pp. 261–269.

Taylor, G. I. (1938), 'The spectrum of turbulence', *Proceedings of the Royal Society of London. Series A-Mathematical and Physical Sciences* **164**(919), 476–490.

Thielicke, W. & Stamhuis, E. (2014), 'PIVLab–towards user-friendly, affordable and accurate digital Particle Image Velocimetry in MATLAB', *Journal of Open Research Software* **2**(1).

Tu, J. H., Rowley, C. W., Luchtenburg, D. M., Brunton, S. L. & Kutz, J. N. (2014), 'On dynamic mode decomposition: theory and applications', *Journal of Computational Dynamics* **1**(2), 391–421.

Uijttewaal, W. S. (2005), 'Effects of groyne layout on the flow in groyne fields: Laboratory experiments', *Journal of Hydraulic Engineering* **131**(9), 782–791.

Uijttewaal, W. S. (2014), 'Hydrodynamics of shallow flows: Application to rivers', *Journal of Hydraulic Research* **52**(2), 157–172.

Uijttewaal, W. & Tukker, J. (1998), 'Development of quasi two-dimensional structures in a shallow free-surface mixing layer', *Experiments in Fluids* **24**(3), 192–200.

van der Graaf, G. (2010), 'GPIV, Open Source Software for Particle Image Velocimetry'.

Wang, H., Cao, H. & Zhou, Y. (2014), 'Pod analysis of a finite-length cylinder near wake', *Experiments in Fluids* **55**(8), 1790.

Wang, H., Gao, Q., Feng, L., Wei, R. & Wang, J. (2015), 'Proper Orthogonal Decomposition based outlier correction for PIV data', *Experiments in Fluids* **56**(2), 1–15.

Wang, H. & Zhou, Y. (2009), 'The finite-length square cylinder near wake', *Journal of Fluid Mechanics* **638**, 453–490.

Weitbrecht, V., Kühn, G. & Jirka, G. (2002), 'Large scale PIV-measurements at the surface of shallow water flows', *Flow Measurement and Instrumentation* **13**(5), 237–245.

Westerweel, J. (1994), 'Efficient detection of spurious vectors in Particle Image Velocimetry data', *Experiments in Fluids* **16**(3-4), 236–247.

Westerweel, J. & Scarano, F. (2005*a*), 'Universal outlier detection for PIV data', *Experiments in Fluids* **39**(6), 1096–1100.

Westerweel, J. & Scarano, F. (2005*b*), 'Universal outlier detection for PIV data', *Experiments in Fluids* **39**(6), 1096–1100.

Zhang, P., Wang, J., Lu, S. & Mi, J. (2005), 'Aerodynamic characteristics of a square cylinder with a rod in a staggered arrangement', *Experiments in Fluids* **38**(4), 494–502.

Zhou, J., Adrian, R., Balachandar, S. & Kendall, T. (1999), 'Mechanisms for generating coherent packets of hairpin vortices in channel flow', *Journal of Fluid Mechanics* **387**, 353–396.

Zhou, Y. & Yiu, M. (2006), 'Flow structure, momentum and heat transport in a two-tandem-cylinder wake', *Journal of Fluid Mechanics* **548**, 17–48.

Zigrang, D. & Sylvester, N. (1982), 'Explicit approximations to the solution of colebrook's friction factor equation', *AIChE Journal* **28**(3), 514–515.

Zong, L. & Nepf, H. (2012), 'Vortex development behind a finite porous obstruction in a channel', *Journal of Fluid Mechanics* **691**, 368–391.